

ELUCIDATING THE MECHANICAL RESPONSE OF METALLIC GLASSES
PREPARED IN DIFFERENT STRUCTURAL STATES AT SUB-MICRON
LENGTH SCALES

Daniel J. Magagnosc

A DISSERTATION

in

Materials Science and Engineering

Presented to the Faculties of the University of Pennsylvania

in

Partial Fulfillment of the Requirements for the

Degree of Doctor of Philosophy

2016

Supervisor of Dissertation

Daniel S. Gianola, Associate Professor

Co-Supervisor of Dissertation

Robert W. Carpick, John Henry Towne Professor

Graduate Group Chairperson

Shu Yang, Professor

Dissertation Committee

I-Wei Chen, Skirkanich Professor of Innovation

Andrea Liu, Hepburn Professor of Physics

for Alli, Kato and Pinky

ACKNOWLEDGEMENTS

Undertaking a doctoral degree has been unique endeavor in terms of both its duration and demands. It was not solely an individual experience; instead, I have been fortunate to share my PhD journey with many people, both within Penn and beyond the confines of the LRSM.

Of course, the utmost of gratitude goes to my mentors, Dr. Daniel Gianola and Dr. Robert Carpick. When I arrived at Penn, you offered me a unique and exciting research opportunity. You pointed me at a project and then let me run. Thank you for this opportunity. Thank you for giving me the latitude to follow my curiosity, wherever it led. Thank you for your mentorship. And more than anything, thank you for your infinite patience as I found my way through challenges big and small. I would also like to thank my funding sources. Much of the equipment I used was purchased with Dr. Gianola's start up funding. The majority of my support came through the Penn MRSEC DMR-1120901. I was also fortunate to be awarded a National Science Foundation Graduate Research Fellowship under Grant No: DGE-132185.

Beyond my advisors and funding sources, I want to thank the Gianola and Carpick research groups. I have learned an immeasurable amount from both groups, particularly communication, critical thinking, and technical skills. I want to specifically acknowledge my fellow Gianola Group members Lisa Chen, Kate Murphy, Mo-rigen He, Jungho Shin, Brian Piccione and especially Danny Strickland for help proof-reading, designing figures, and stimulating discussions on deformation mechanisms in amorphous materials, big and small. Additionally, I wish to thank Tevis Jacobs, Filippo Magnolini, Graham Wabiszewski, and Nitya Gosvami from the Carpick Group.

I have also been fortunate to work with many excellent collaborators within the Penn community and beyond. Thank you to my committee members, I-Wei Chen and Andrea Liu, for their insights and guidance. Thank you to the DISCONAP community, where I expanded my perspective far beyond the scope of my project and developed many new ideas. My nanowire work was performed with Jan Schroers and Wen Chen, at Yale University, and Golden Kumar, at Texas Tech. I learned an immeasurable amount about metallic glasses during our discussions and iterations on manuscripts. I would like to further thank Julie Cairney and Peter Felfer, from the University of Sydney, for assistance with atom probe tomography. Thank you Gang Feng, at Villanova University, for conducting the nanoindentation studies. Xuemei Cheng, Le Ye, and Xuzhao Chai at Bryn Mawr College, thank you for help your with sputter deposition. Thank you as well to Kevin Turner and Yijie Jiang for providing access to the triboindenter. Beyond those directly involved in my dissertation research

I had the pleasure of learning from and working with many other great colleagues. Thank you Chris Eberl, Gidong Sim, Joost Vlassak, Peter Derlet, Sei Jin Park, A. John Hart, Prashant Purohit, Mingliang Zhang, and Cherie Kagan.

I am also extremely grateful for the assistance from the staff here at Penn. Steve Szewczyk, if I ever needed a random piece of material, lab equipment, or really just about anything you were always my first stop. Without your help I don't know what I would have done. Doug Yates and Jamie Ford, thank you for giving me free reign throughout the Nanoscale Characterization Facility and putting up with my many complaints. Thank you to the Quattronne Nanofabrication facility staff, Noah Clay, Meredith Metzler, Gerald Lopez, and Charlie Veith, for your help, valuable insights, and investment in my success. And of course I am extremely grateful for the help of the administrative staff members, Pat Overend, Rico Vargas, Irene Clements, and Vicky Lee, for help with reimbursements, shipping, and much more.

While the science is first and foremost, much of the PhD experience occurs beyond the laboratory through the friendships that are developed. Thank you Rob Middleton, Frank Streller, Nick Greybush, Daksh Agarwal, and Jacob Berger for taking breaks from foosball to work on problem sets, talk shop, and to just have a fun over the past five years. In addition to my cohort Penn Engineering has a fantastic community of students. Thanks to Rahul Agarwal, Cathy Yang, Mike O'Reilly, Spencer Thomas, Emmabeth Parish, Kirk Vaughn, Boris Rasin, Jason Reid, Elaine Lee, Ted Trigg, Hossein Ahmadzadeh, Nadia Krook, Brian Cosgrove, Bhavana Mohanraj, Rob Ferrier, and Jim Borchert. Coffee hour, happy hour, and all things social would have been dull without you.

I have also had the immense benefit of a family that put the utmost value on education. Thank you to my grandparents, Barbara, Tom, Ann and Stan, for sating my curiosity with an endless supply of museum visits, books, and woodworking projects during my summer visits. Thank you Mom and Dad for emphasizing the importance of education. Thank you driving me to endless activities, always encouraging me, and providing ample opportunities for success.

I also must express my extreme gratitude to those who bore the brunt of my crazy work schedule and the stress that comes with a PhD. Kato and now Pinky, you might be cats but that does not diminish the role you played in my success. Thank you waiting by the door for me to get home, and your unconditional excitement to greet me. There is no better stress relief than a purring, furry friend who doesn't care about anything but you. Finally, this brief acknowledgement can't capture the extent of my gratitude for Allison. Thank you for your patience, love and support. Thank you for bringing energy and enthusiasm to balance my reserved nature. And more than anything thank you for always being there for me.

ABSTRACT

ELUCIDATING THE MECHANICAL RESPONSE OF METALLIC GLASSES
PREPARED IN DIFFERENT STRUCTURAL STATES AT SUB-MICRON
LENGTH SCALES

Daniel J. Magagnosc

Daniel S. Gianola

Robert W. Carpick

Metallic glasses (MGs) exhibit both high yield stresses and elastic strain limits owing to their metallic bonding character and lack of long-range order. Yet the structural state (i.e. local atomic packing), and the corresponding elastic and plastic mechanical response, of MGs is nuanced and dependent on processing history. Moreover, the interplay between small length scales and glass processing routes have produced seemingly conflicting results. Here, the influence of processing on MG mechanical behavior at sub-micron length scales is explored, revealing extreme sensitivity to ion irradiation, enhanced control over the mechanical response, and an underpinning of yield strength in thermodynamic properties.

Using *in situ* testing methods, the deformation response of individual thermo-plastically molded MG nanowires is studied. In contrast with previous literature reports the nanowire behavior is observed to be consistent with bulk deformation, exhibiting brittle fracture and shear banding at room temperature. To determine the role of processing at the nanoscale, ion irradiation is used to systematically alter the glassy structure of molded nanowires, leading to enhanced tensile ductility and reduced strength. A model for MG strength and ductility rationalizes the observations

based on the glass transition temperature and a structure-dependent excess energy term. In addition, studying deformation at elevated temperature provides insight into the role of size and processing history on the mechanical properties in MGs. The Newtonian to non-Newtonian flow transition occurs at higher strain rates in nanoscale specimens. This suggests a more relaxed nanowire structural state, potentially owing to thermal processing, and a wider range of thermally accessible structures at the nanoscale. Finally, the range of structural states in MG thin films is explored by sputter deposition at different substrate temperatures. The maximum hardness increases more than 30% with deposition temperature, revealing a wide range of achievable glass structures. Together, the nanowire and thin film results emphasize the need to quantify glass structural state and suggest a potential processing – structural state – property relationship in MGs, correlating mechanical properties with thermodynamic quantities.

TABLE OF CONTENTS

ACKNOWLEDGEMENTS	iii
ABSTRACT	v
LIST OF TABLES	x
LIST OF FIGURES	xiii
1 Introduction	1
1.1 Glass Forming Process	3
1.2 Describing Glass Structure	6
1.3 Metallic Glass Deformation	10
1.3.1 Deformation Phenomenology	13
1.3.2 Controlling Metallic Glass Deformation	15
1.4 Processing Sensitivity	16
1.4.1 Relaxation	22
1.4.2 Rejuvenation	24
1.5 Small Scale Metallic Glass Deformation	28
1.6 Overview	31
2 Materials and Methods	34
2.1 Tensile Testing of Individual Nanowires	35
2.1.1 Nanowire Fabrication and Harvesting	35
2.1.2 <i>In situ</i> Nanomechanical Testing	37
2.1.3 High Temperature Creep Measurements	38

2.1.4	Estimate of Experimental Uncertainty	41
2.2	Ion Irradiation of Metallic Glass Nanowires	43
2.2.1	Characterizing Ion Damage in MG nanowires	45
2.3	Sputtered Metallic Glass Thin Films	46
2.3.1	Deposition	46
2.3.2	Characterization	47
2.3.3	Assessing Deformation Response	48
3	Tunable Tensile Response of Molded Metallic Glass Nanowires	50
3.1	Nanowire Tensile Response	51
3.1.1	Role of Fracture Location	55
3.2	Discussion	56
3.3	Conclusion	60
4	Systematic Study of Ion Irradiation	62
4.1	Structural Characterization of Irradiated Nanowires	63
4.2	Tensile Response of Irradiated Nanowires	65
4.2.1	Effect of Ion Irradiation on Tensile Ductility and Yield Strength	68
4.3	Discussion	74
4.3.1	Size-Independent Transition in Plastic Deformation Owing to Ion Irradiation	74
4.3.2	Effect of Ga Implantation on the Observed Mechanical Response	76
4.3.3	Effects of Ion Irradiation on Atomic Structure	79
4.3.4	Revisiting Kinetic and Thermal Phenomena in Amorphous Ma- terials Below the Glass Transition	80
4.3.5	Correlations between T_f and Plastic Deformation, and T_g and Yield Strength	82

4.3.6	New Analytical Model for Universal Strength Scaling Dependent on Glass Structural State	84
4.3.7	Application of Yield Strength Prediction to Severely Deformed Metallic Glasses	90
4.4	Conclusion	94
5	Thermoplastic Deformation of Individual Nanowires	97
5.1	High Temperature Creep Measurement	98
5.1.1	Viscosity Scaling with Power Dissipation	102
5.1.2	Preservation of Amorphous Structure	104
5.2	Transition in Flow Behavior	106
5.2.1	Determination of Flow Regime	106
5.2.2	Size Dependent Flow Transition	109
5.3	Discussion	112
5.4	Conclusion	116
6	Vapor Deposited Metallic Glass Thin Films	118
6.1	Characterization of Sputtered Thin Films	119
6.2	Mechanical Properties	122
6.3	Structural State in Sputtered Thin Films	126
6.4	Conclusion	130
7	Conclusion and Perspectives	131
Appendix A Operation of SmarPod Nanomechanical Testing Appa- ratus		137
BIBLIOGRAPHY		143

LIST OF TABLES

TABLE 1:	Summary of metallic glass relaxation treatments	20
TABLE 2:	Summary of metallic glass rejuvenation treatments	20
TABLE 3:	Composition of sputtered Pd-based MG thin films	120

LIST OF FIGURES

FIGURE 1.1: Glass forming process	4
FIGURE 1.2: Structural measurements of metallic glasses	7
FIGURE 1.3: Illustration of free volume	8
FIGURE 1.4: Processing dependence of excess enthalpy in metallic glasses	9
FIGURE 1.5: Shear Transformation Zone (STZ) Schematic	11
FIGURE 1.6: Illustration of the potential energy landscape	13
FIGURE 1.7: Bulk Metallic Glass Deformation Map	14
FIGURE 1.8: Cooling rate dependence of metallic glass microhardness and density	17
FIGURE 1.9: Illustration of relationship between metallic glass properties and structural state	19
FIGURE 1.10: Thermal relaxation near the glass transition	23
FIGURE 1.11: Hardening of metallic glass by cyclic loading in spherical nanoindenter	24
FIGURE 1.12: Rejuvenation through thermal processing	25
FIGURE 1.13: Effect of high pressure torsion (HPT) on hardness, modulus, and excess enthalpy	27
FIGURE 1.14: Size dependent deformation morphology in metallic glass micropillars	29
FIGURE 1.15: Size dependent criteria for formation of shear bands in metallic glasses	30
FIGURE 2.1: Nanowire molding process	35
FIGURE 2.2: Manipulation of individual MG nanowires	36

FIGURE 2.3: Nanomechanical Testing Apparatus	37
FIGURE 2.4: Schematic of nanowire creep experiment	39
FIGURE 2.5: Custom fiducial marker tracking	41
FIGURE 2.6: Nanowire Irradiation analysis	44
FIGURE 3.1: Tunable nanowire tensile response	54
FIGURE 3.2: Effect of fracture location on nanowire strength	56
FIGURE 3.3: Size effects in metallic glass tensile deformation	59
FIGURE 4.1: Structural Characterization of Irradiated Nanowires	64
FIGURE 4.2: Representative stress-strain curves for irradiated nanowires	67
FIGURE 4.3: Deformation map showing the influence of ion fluence and irradiated volume fraction on amount of plastic strain and fracture morphology.	69
FIGURE 4.4: Deformation map showing the influence of ion fluence and irradiated volume fraction on yield stress.	73
FIGURE 4.5: Direct comparison of the effect of different Ga ion treatments on the average measured strength.	75
FIGURE 4.6: Application of yield strength model to severely deformed metallic glasses	92
FIGURE 5.1: Nanowire creep experiment	99
FIGURE 5.2: Determination of steady-state flow response	101
FIGURE 5.3: Scaling of viscosity with power dissipation	103
FIGURE 5.4: Preservation of amorphous structure.	105
FIGURE 5.5: Characterizing flow behavior in metallic glass nanowires. . .	108
FIGURE 5.6: Flow transition in metallic glass nanowires.	111

FIGURE 6.1: Structural characterization of sputtered Pd-based MG thin films	121
FIGURE 6.2: Indentation response of Pd-based MG thin films at different deposition temperatures	123
FIGURE 6.3: Indent morphology of Pd-based MG thin films	125

Chapter 1

Introduction

Metallic glasses (MGs) are a unique class of materials with a suite of advantageous properties. In contrast with conventional engineering metals, MGs lack the long range order and well-defined defect structures intrinsic to crystalline solids. However, it is this amorphous structure in conjunction with a predominantly metallic bonding character that gives rise to the unique properties of MGs. For instance, some iron-based MGs exhibit excellent soft magnetic properties such as high saturation induction, low magnetic permeability, and low loss¹⁻³. As a result, magnetic MG allows have been widely employed in electrical power transformers cores, under the trade name Metglas, as well as current inductors and radio-frequency antennas, under the names Licalloy and SENNTIX⁴⁻⁶. Regardless of the application, iron-based MGs have resulted in significant electrical power savings, as high as 60%^{3, 4}.

While MGs were first developed in ribbon form in 1960, broad application beyond the initial magnetic applications was limited by the small achievable specimen sizes achievable⁷. Recently, with the advent of bulk glass formers^{8, 9}, interest in MGs has renewed and primarily centered on their excellent mechanical properties¹⁰⁻¹². Typically, MGs exhibit large elastic strain limits^{11, 13}, high strength^{14, 15}, low internal friction^{16, 17}, and potentially good fracture- and wear-resistance¹⁸⁻²⁰. Compared to crystalline metals, with low elastic limits and strengths, MGs are exceptional. MGs

yield at an apparently universal 2% strain¹³ and gigapascal strengths^{14, 15} compared to the less than 0.2% yield strains and 100's of MPa strengths typical of crystalline metals¹¹. In fact record yield strengths in MGs reach 6 GPa in a Co-based bulk system²¹.

The exceptional mechanical properties coupled with facile processing through thermoplastic molding make MGs attractive in many structural applications. A broad range of potential applications have been demonstrated including springs, gears, cutting blades, and sports equipment^{8, 9, 11, 22, 23}. Additionally, MGs are particularly well-suited for use in microelectromechanical systems (MEMS) devices such as actuators or resonators^{24, 25} which take advantage large elastic strain limits, low internal friction, and the lack of an internal length scale, which results in isotropic properties and lifts restriction imposed by grain size^{26, 27}. Finally, MGs have been explored for use in biomedical implants²⁸⁻³¹ and tribological applications³²⁻³⁴. Yet widespread adoption of MGs in structural roles has faltered in large part due to the propensity to form shear bands leading to catastrophic failure via brittle fracture³⁵.

As a result, successful application of MGs requires an understanding of the unique processing sensitivity that emerges from the glass forming process. For instance, the outstanding performance of MGs in soft magnetic applications hinged on a detailed understanding of how thermal treatments relaxed casting stresses and controlled the magnetic domain structure^{2, 3}. In contrast, the role of processing on mechanical properties has been widely examined but a comprehensive processing – property

relationship remains absent. In this first chapter glass formation and structural descriptors of MGs are reviewed in the context of various processing routes applied to MGs to control their mechanical properties with the aim of developing a potential framework for understanding structure – property – processing relationships in MGs.

1.1. Glass Forming Process

To form a metallic glass, the liquid phase must be cooled sufficiently quickly to circumvent crystallization. Upon cooling below the liquidus temperature, a strong driving force for nucleation and growth of crystallites emerges in the supercooled liquid phase³⁶⁻³⁸. As the supercooled liquid is further cooled the driving force grows, ultimately resulting in crystallization as indicated by the cooling path intersecting the crystallization nose in the time-temperature-transition (TTT) diagram, shown schematically as cooling path (1) in Figure 1.1a (adapted from Ref. 39). When considering the energy of the system, as shown in Figure 1.1b (adapted from Ref. 36), a discontinuous transition from the high energy liquid to the low energy parent crystal state is found.

However, if a critical cooling rate (R_c) is exceeded, the supercooled liquid avoids the crystallization nose⁴⁰, as shown by cooling path (2) in Figure 1.1a . In this case the supercooled liquid remains in a dynamic equilibrium, where the atomic relaxation times are sufficiently fast to accommodate changes in temperature. This equilibrium persists until the relaxation times reach 100s of seconds and the liquid undergoes

kinetic freezing as a part of the glass transition and the structure ceases to evolve^{36, 37}. In the energy diagram, the glass transition is observed as a smooth transition from the rapidly changing supercooled liquid to the slowly varying glass phase with an enthalpy difference with respect to the parent crystal^{36, 37}. This process is illustrated by cooling path (2) in Figure 1.1b. Critically, further increasing the cooling rate results in a glass transition at higher temperatures and enthalpies, resulting in subtle differences in amorphous structures. This variability in glass formation is demonstrated by the difference between the slow cooling rate of (2) as compared to the fast cooling rate of

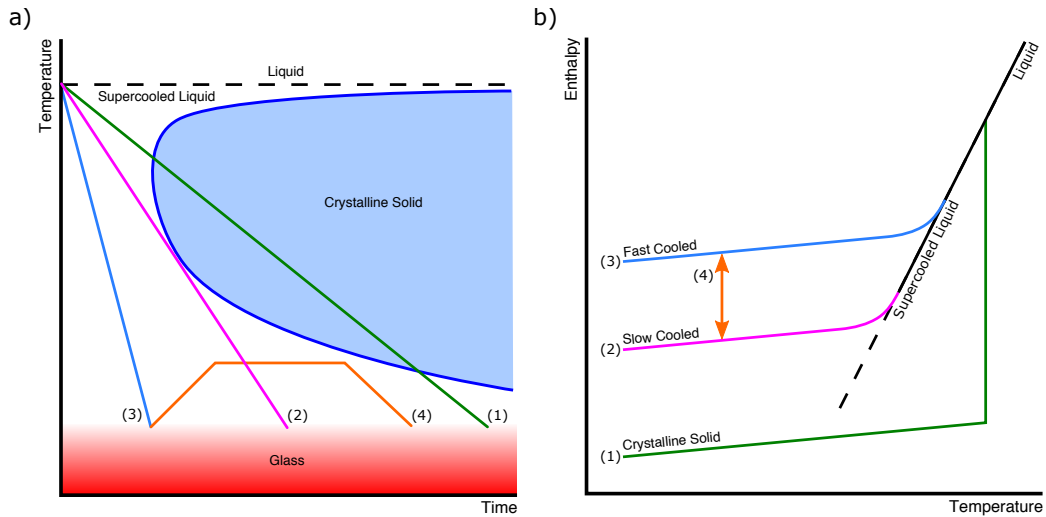


Figure 1.1: The glass forming process is illustrated in a) through a time-temperature-transition diagram (TTT). In the TTT diagram cooling path (1) intersects the crystallization nose resulting in a crystalline solid. If a critical cooling rate, shown as path (2), is achieved the crystallization nose is avoided resulting in a glassy solid. The cooling rate can be further increased, shown as path (3), resulting in earlier glass formation. The different cooling paths result in distinct system enthalpies as shown in b). Again, cooling path (1) results in crystallization and a discontinuous change in enthalpy. Cooling paths (1) and (2) result in glass formation and a continuous transition from the supercooled liquid to amorphous solid. However, the difference in cooling rate results in a glass transition at higher temperatures and enthalpies as the cooling rate increases. Finally, the glass structure may be tuned between the extremes of cooling rate by annealing in the supercooled liquid as shown by path (4).

(3). Finally, the glass structure may be varied between the extremes of cooling rate after glass formation by annealing in the supercooled liquid as shown in path (4). In this region the crystallization kinetics are sluggish, enabling a wide range of potential cooling rates and resulting enthalpies. Therefore, it is the inherent metastability of the amorphous structure that gives rise to the unique processability of MGs. While thermal processing is the canonical method to tune glass response, many other routes have been explored in MGs and will be discussed in detail in remainder of this chapter.

From a practical standpoint, producing a metallic glass often requires extreme processes such as melt spinning with cooling rates on the order of $10^6 K/s$ ^{7, 39}. Yet such high cooling rates restrict the critical casting thickness to 10's of microns^{41, 42}. As a result, the metallic glass community has striven to reduce R_c and achieve greater casting thicknesses, in excess of 10 cm, for the best glass formers. This effort has resulted in a series of empirical rules for producing MGs. In general, good glass forming ability is achieved by choosing a composition with at least three primary constituents that lie near a deep eutectic, with large atomic sizes mismatches ($>12\%$), and with large negative enthalpies of mixing. However, the gains in casting size have been achieved at the expense of structural control by restricting the range of usable cooling rates based on the approximate relation between cooling rate (R) and casting thickness (t) given as $R \approx 10/t^2$ ⁴².

1.2. Describing Glass Structure

In order to compare different processing steps a good descriptor of the resulting structure is required. However, describing the glassy structures of MGs remains an outstanding challenge. In stark contrast to crystalline metals, when examined by a cabinet x-ray diffractometer, different glass structures, and hence processing histories, are largely indistinguishable^{43–46}. To resolve quantifiable differences in structure the high resolution of synchrotron x-ray sources or neutrons are required^{47–50}. The difference in sensitivity between cabinet x-ray diffractometers and high energy diffraction sources is shown in Figure 1.2. Here, high energy x-rays and neutrons reveal subtle differences in the structure factor, particularly in the first and second scattering peaks, due to changes in composition in a binary Cu-Zr glass. Critically, such experiments reveal ordering in MGs at short and medium ranges, where short-range order refers to nearest neighbor distances while medium-range order describes the arrangement of different short-range structural motifs.

Yet even the highest resolution measurements cannot uniquely identify structural configurations. For simple binary alloys the distribution of structural motifs may be extracted with the aid of computer simulations^{47, 48, 51–53}. While molecular dynamics (MD) simulations have greatly advanced the understanding of glass structure and helped identify specific atomic packing configurations prone to deformation^{54–56}, the impact has been muted by the lack of direct experimental observations to findings from MD. Furthermore, as the chemical complexity of a glass forming alloy is increased, as

is often necessary to improve glass forming ability, the resulting structural complexity makes solving for the structure intractable^{51, 57}. Instead, only global changes in atomic density may be inferred from changes in the radial distribution function^{49, 50, 58–62}.

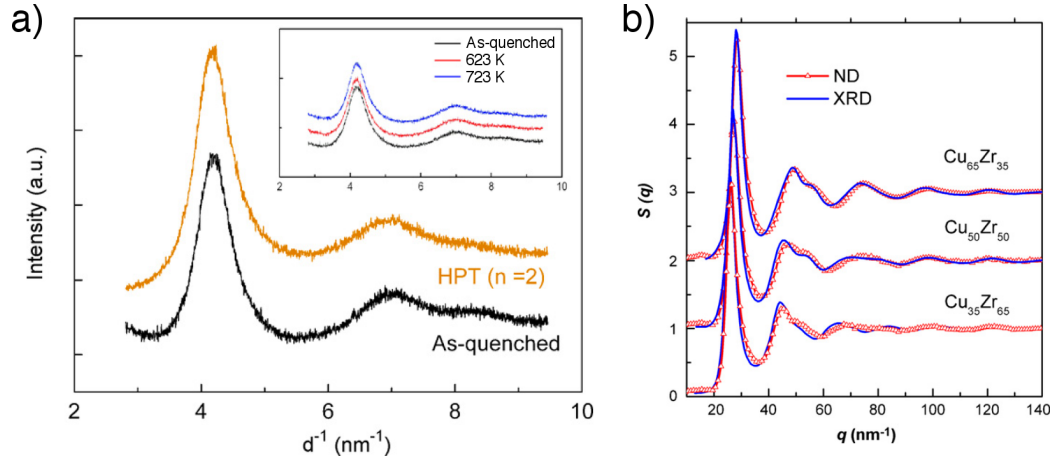


Figure 1.2: a) From Ref. 46, XRD patterns from an as-quenched metallic glass (black) and glasses subjected to high pressure (orange) torsion or annealed at 623 K (red) and 723 K (blue) are largely indistinguishable. Copyright 2010, with permission from Elsevier. b) From Ref. 48, in contrast, high energy sources such as synchrotrons or neutrons reveal subtle differences in the structure factor, particularly in the first and second scattering peaks, due to changes in composition in a binary Cu-Zr glass. Copyright 2009, with permission from Elsevier.

Similarly, recent advances in electron microscopy have led to techniques capable of glean information from disordered solids. For instance, fluctuation electron microscopy (FEM) employs a statistical approach to construct a radial distribution function from fluctuations in contrast^{63–66}. In this way, FEM is able to overcome challenges associated with dynamic scattering of electrons to probe both short- and medium-range order in MGs. Furthermore, the development of new scanning transmission electron microscopy methods has enabled direct observation of local packing^{67, 68}. When applied to a binary glass, diffraction measurements taken with a coherent

Angstrom scale spot size revealed distinct packing configurations and allowed specific icosahedral ordering to be determined from rotational symmetries. Despite the new insights provided by cutting-edge electron diffraction methods, many of the same challenges encountered in XRD remain in determining specific atomic positions and environments.

As a result, the metallic glass community has turned to other metrics to describe glassy structures. The canonical descriptor employed in both theoretical and experimental studies of MGs is the free volume⁶⁹⁻⁷². Shown schematically in Figure 1.3, the free volume quantifies deviations from the ideal packing efficiency. However, free volume is typically an experimentally intractable quantity. While methods such as positron annihilation spectroscopy⁷³⁻⁷⁵ are able to measure free volume, the measurements are often limited to quantifying differences in free volume⁷⁶⁻⁷⁹. Yet in order to apply theoretical models for MG deformation, the absolute value of free volume is necessary since subtle changes may result in drastically different properties.

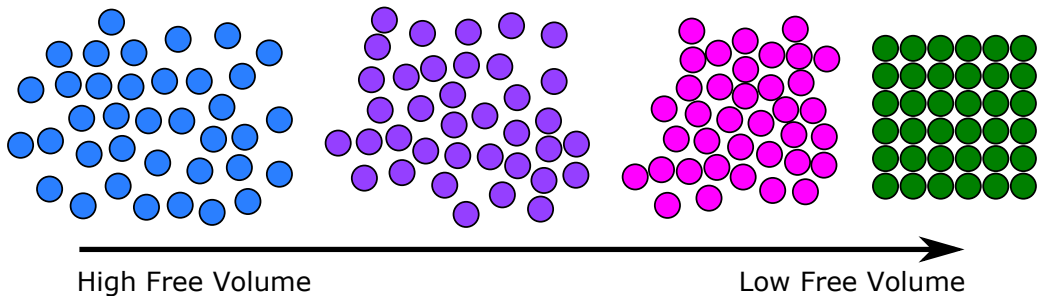


Figure 1.3: Free Volume quantifies deviations from ideal packing. In a crystal, the free volume is low due to efficient packing. However, glasses can have a range of free volumes depending on the temperature and processing history

Given the challenges associated with directly interrogating free volume, alternative

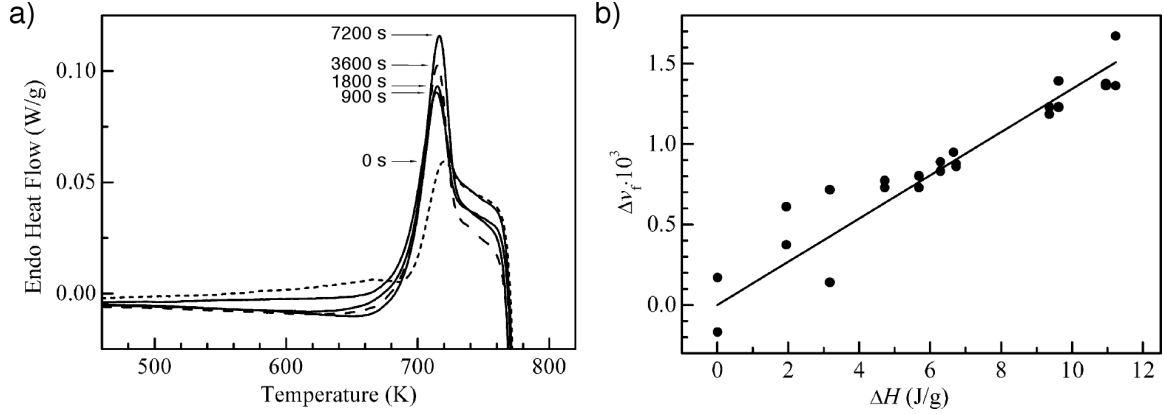


Figure 1.4: From Ref. 85, a) the effect of annealing time at 675K ($0.92T_g$) on the heat flow around the T_g in a $\text{Zr}_{55}\text{Cu}_{30}\text{Al}_{10}\text{Ni}_5$ metallic glass. As the annealing time increases, the endothermic peak beginning around 700K grows, indicating less excess enthalpy after annealing. In b) changes in enthalpy are correlated to differences in free volume determined from changes in density after thermal treatments. Copyright 2003, with permission from Elsevier.

metrics, which are related to free volume, are desirable. One such indicator is the calorimetric response of MGs around the glass transition temperature (T_g), which strongly depends on structural state. For instance, different processing routes enact small changes in T_g , up to a few Kelvin^{80–82}. More importantly, the enthalpy evolved around T_g strongly indicates changes in structure. By integrating the enthalpy release while heating through the glass transition, an excess enthalpy can be determined and used to compare different processing histories^{45, 83–86}. Such changes in excess enthalpy have been further correlated to changes in free volume⁸⁵. An example of the typical differences in the calorimetric response of MGs prepared under annealing treatments are shown in Figure 1.4a for a $\text{Zr}_{55}\text{Cu}_{30}\text{Al}_{10}\text{Ni}_5$ metallic glass. Furthermore, the changes in enthalpy are correlated with changes in free volume in Figure 1.4b.

However, simply comparing energies hinders comparison between different glass

chemistries with subtly different thermal responses. Instead, the fictive temperature (T_f) may be a suitable parameter to describe glass structural state. The fictive temperature describes the temperature at which a glassy structure would be at equilibrium⁸⁷⁻⁹⁰. Unlike T_g , T_f is a thermodynamic property making it sensitive to processing history. As a result, comparing T_f to T_g enables comparison of processing routes and different glass systems⁹¹. Here, a high T_f relative to T_g indicates a “liquid-like” structure while a low T_f relative to T_g indicates a more ordered glass structure. A detailed discussion of the determination of T_g and T_f can be found in Chapter 4.

1.3. Metallic Glass Deformation

The well-ordered structure of crystalline metals has facilitated a detailed understanding of the mechanisms that accommodate plastic deformation. As a result, many processes, including dislocation motion, deformation twinning, and grain boundary sliding, have been identified, and are active to different extents depending on the microstructure and testing conditions⁹²⁻⁹⁷. In contrast, all deformation in MGs is understood as the result of a single fundamental unit, the shear transformation zone (STZ)¹⁰.

A shear transformation zone is a small volume of atoms which undergo a cooperative, non-affine rearrangement due to an applied shear stress^{69, 70}. A schematic of this process is illustrated in Figure 1.5. The fundamental groundwork for the STZ was developed by Spaepen and Argon in the late 1970’s to describe the vari-

ous deformation modes observed in MGs^{69, 70}. By modeling a competition between stress-driven activation of STZs and thermal relaxation of deformation-induced excess free volume and local stresses, Argon predicted the transition between the low and high temperature deformation regimes⁷⁰. Subsequently, the STZ framework has been adapted into detailed theoretical models⁹⁸, constitutive models^{72, 99–101}, and finite element methods^{102–107}.

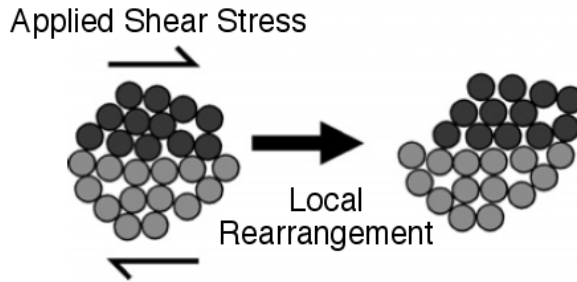


Figure 1.5: From Ref. 10, An illustration of a shear transformation zone (STZ) in which a group of atoms undergo a local rearrangement due to an applied shear stress. Copyright 2007, with permission from Elsevier.

Critically, the STZ is a transient defect and its location cannot be identified *a priori*. Instead, much effort has been made to identify structural motifs that are more or less likely to deform^{54–56, 108}. Atomistic simulations have suggested that some local atomic packing environments, coined geometrically unfavorable motifs, preferentially deform^{54, 55}. These motifs typically include distorted icosahedra; in contrast, ideal icosahedra are unlikely to deform. This result suggests STZs to be a more concrete structural feature rather than simply local regions of enhanced free volume.

Similarly, new conceptual frameworks for STZs which incorporate the energy topology have emerged. Mapping deformation to an energy landscape is a potentially

powerful framework for understanding micromechanisms and enables facile comparison to structural descriptions based on excess enthalpy. In the potential energy landscape description (PEL), different deformation mechanisms are related to various relaxation processes^{109–115}. Specifically, the topology of the internal glass energy is described as a rugged energy landscape consisting of many energy macro-basins^{37, 111}. Within the macro-basins, multiple sub-basins exist resulting in local energy minima and distinct structural states. Within this PEL, picture transitioning between macro-basins is associated with the α -relaxation (i.e. escaping the macro-basin pictured in Figure 1.6) and related to either the glass transition or mechanical yield^{37, 109, 112, 114}. Transitions between the local minima of sub-basins, such as those pictured in Figure 1.6, is associated with secondary β -relaxations, which have been suggested to be equivalent to STZs.

While the PEL description of MGs provides a simple mapping of glass structural state onto an energy spectrum, the details of the PEL show sensitivity to history and ultimately define the dynamic response of the glass^{115, 116}. For instance, the profile of the macro-basins and organization of sub-basins was found to depend on cooling rate. Here, the slope of the macro-basin is related to shear modulus, and decreases with increasing cooling rate, providing evidence that the mechanical response may strongly depend on processing. Yet the shape of the sub-basins, which is related to the high frequency response, appears to be insensitive to history^{115, 116}. The PEL and its sensitivity to cooling rate are illustrated in Figure 1.6.

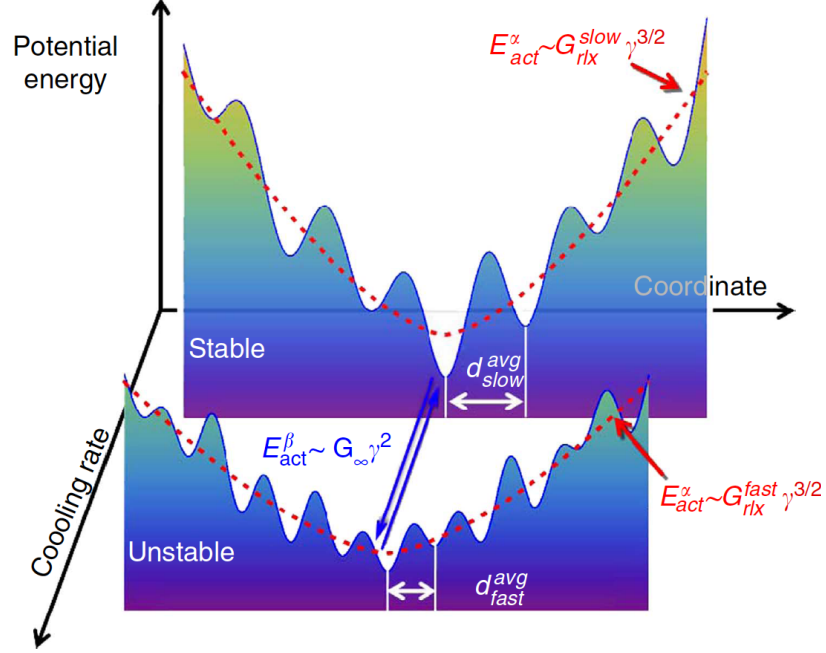


Figure 1.6: From Ref. 115, the shape of the potential energy landscape, as determined from the shear modulus is illustrated. Here the high frequency response, which contributes to the topology of individual sub-basin, is insensitive to cooling history. Yet the non-affine contribution to the shear modulus is highly sensitive to cooling history leading to broadening of the macro-basin with increasing cooling rate. Copyright 2014, with permission from Nature Publishing Group

1.3.1. Deformation Phenomenology

In general, the STZ-based deformation in MGs can be grouped into a high and low temperature regime. In the high temperature regime, above $\sim 0.8T_g$, MGs homogeneously flow under applied stresses¹¹⁷ and thermal relaxation begins dominating the deformation response. At low strain rates, activating an STZ produces free volume and the materials softens. However, thermal relaxation quickly erases this history-induced softening and annihilates excess free volume⁶⁹. As the strain rate increases thermal relaxation must compete with an ever increasing amount of strain-induced free volume generation⁹⁹. Eventually, an excess of local softening occurs and the

material transitions to a new, softer equilibrium state with higher free volume. This results in an observed transition from Newtonian to non-Newtonian flow^{118–127}. The strain rate at which this transition occurs is highly temperature dependent.

In contrast to the homogeneous deformation at high temperatures, in the low temperature regime MG deformation is heterogeneous³⁵. Below $\sim 0.8T_g$, STZs activate in a cooperative manner and the deformation localizes into shear bands³⁵. Upon yield, the material within a shear band softens and the strain rate bifurcates, going to zero outside the shear band while rapidly increasing within the shear band⁷⁰. In

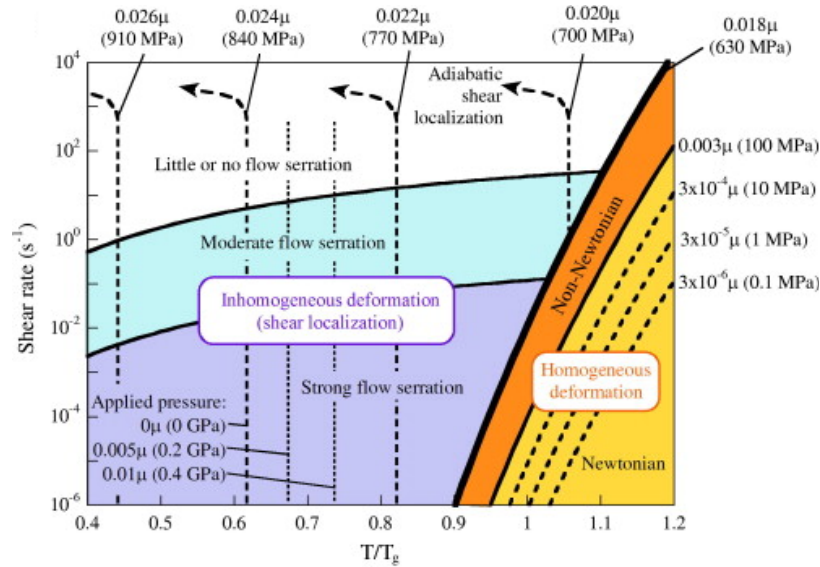


Figure 1.7: From Ref. 10, a qualitative map of bulk metallic glass deformation modes. For the range of strain rates included here, deformation localizes under all applied strain rates at temperatures less than $0.9T_g$. Depending on the strain rate, flow serrations (i.e. periodic load or displacement bursts) are observed. At lower temperatures, the strain rate must also be correspondingly lower (less than the minimum strain rates shown here) to avoid inhomogeneous deformation. At sufficiently high temperatures (i.e. $> 0.9T_g$), the bulk metallic glass deforms homogeneously in a non-Newtonian manner at high strain rates and in a Newtonian manner at sufficiently low strain rates. Regardless of the temperature, at very high strain rates, deformation will always localize. Copyright 2007, with permission from Elsevier.

the absence of a mechanism to arrest the shear band, such as confinement^{128–130} or competing thermal and strain rate effects^{131, 132}, a single, system spanning shear band will result in catastrophic failure³⁵. Under appropriate conditions, flow serrations, observed as periodic load or displacement bursts, are observed¹⁰. It is precisely this process of shear localization that has restricted application of metallic glasses. Based on these observations a deformation map for MGs has been developed as shown in Figure 1.7

1.3.2. Controlling Metallic Glass Deformation

In an effort to control or even prevent shear bands and achieve homogeneous deformation akin to the high temperature response, a number of strategies have been employed. For instance, tuning glass composition has proven effective in improving bending ductility and toughness^{18, 133–135}. These gains have been made in two ways. First, the chemistry was intentionally altered to promote the formation of crystalline precipitates,¹³³ thereby creating a MG metal matrix composite. The precipitates assist in arresting or deflecting shear band propagation when their spacing is below a critical length scale. Such composite structures are interesting and promising structural materials but are beyond the scope of this study, which focuses on purely amorphous structures and not composites..

Second, glass compositions have been selected to favor low ratios of the shear modulus to bulk modulus (G/B), which correspond to high Poisson's ratios (ν)^{18, 134, 135}.

In this case, the MG approaches an incompressible solid (i.e. $\nu = 0.5$). This favors the nucleation of a high density of shear bands as opposed to a single shear band by inhibiting dilation along the shear band and favoring shear band extension¹³⁴.

However, these strategies for shear band control necessitate altering the glass composition to achieve the desired response. Yet many applications require specific chemistries, for instance to ensure bio-compatibility²⁸⁻³¹, corrosion resistance^{23, 136}, or magnetic properties¹⁻³. As a result, post-processing routes have also been explored to tune the desired MG response.

1.4. Processing Sensitivity

The fundamental physics of glass formation and the unique metastability that results enable a continuous spectrum of structural states. Changing the cooling rate shifts the glass transition to higher or lower temperatures for higher or lower cooling rates, respectively. While the changes in T_g are small, significant changes in properties are observed. As the cooling rate increases, a less dense structure is produced with subtly different atomic packing environments¹³⁷; as a result the modulus and hardness decrease and ductility increases^{57, 138-142}. Figure 1.8 shows the cooling rate dependence of microhardness in a Pd-based MG. Accordingly, a terminology has emerged to qualitatively describe the effect of cooling rate on glassy structure. Here lower cooling rates produce more “solid-like” structures while higher cooling rates result in more “liquid-like” structures.

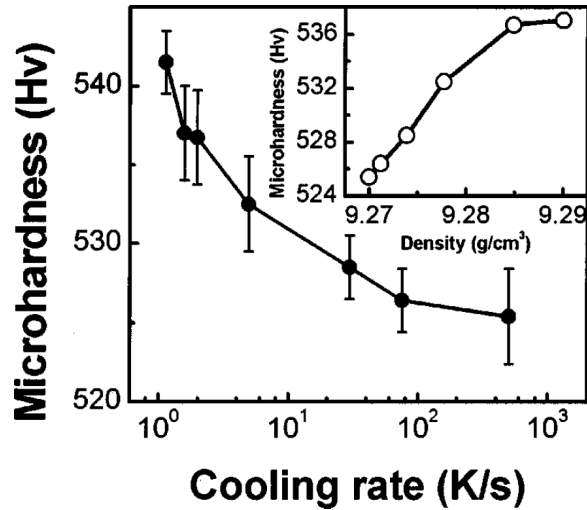


Figure 1.8: From Ref. 138, the cooling rate is found to influence the microhardness in Pd-based MG. Slow cooling rates result in greater microhardness. This is further reflected in an increase in density (inset). Copyright 2001, with permission from American Physical Society.

However, control over the glassy structure is not restricted to the time of glass formation. While thermal processing (i.e. changing cooling rate) is the prototypical method to enact structural changes in glasses, numerous processes have been explored to alter the glass structure and properties. These methods may broadly be described as either a relaxation or rejuvenation process, with the former corresponding to lower effective cooling rates and the latter indicating higher effective cooling rates.

Yet, despite extensive examinations of processing effects on metallic glasses, a comprehensive framework for comparing and assessing the effects of various processes is absent. In particular, the effects of relaxation and rejuvenation processes on the mechanical properties have not been consistently linked to changes in MG structural descriptors. In reviewing reports from the literature, a general trend emerges in

which the effect of a processing route may be explained through the interdependent structural descriptors of excess enthalpy and free volume. This relationship is shown schematically in Figure 1.9, which summarizes the relationship between mechanical properties and structure, as described by excess enthalpy or free volume, for many methods used to alter metallic glasses. The details of the MG processing methods are summarized in Table 1 and Table 2 respectively and described in the following sections.

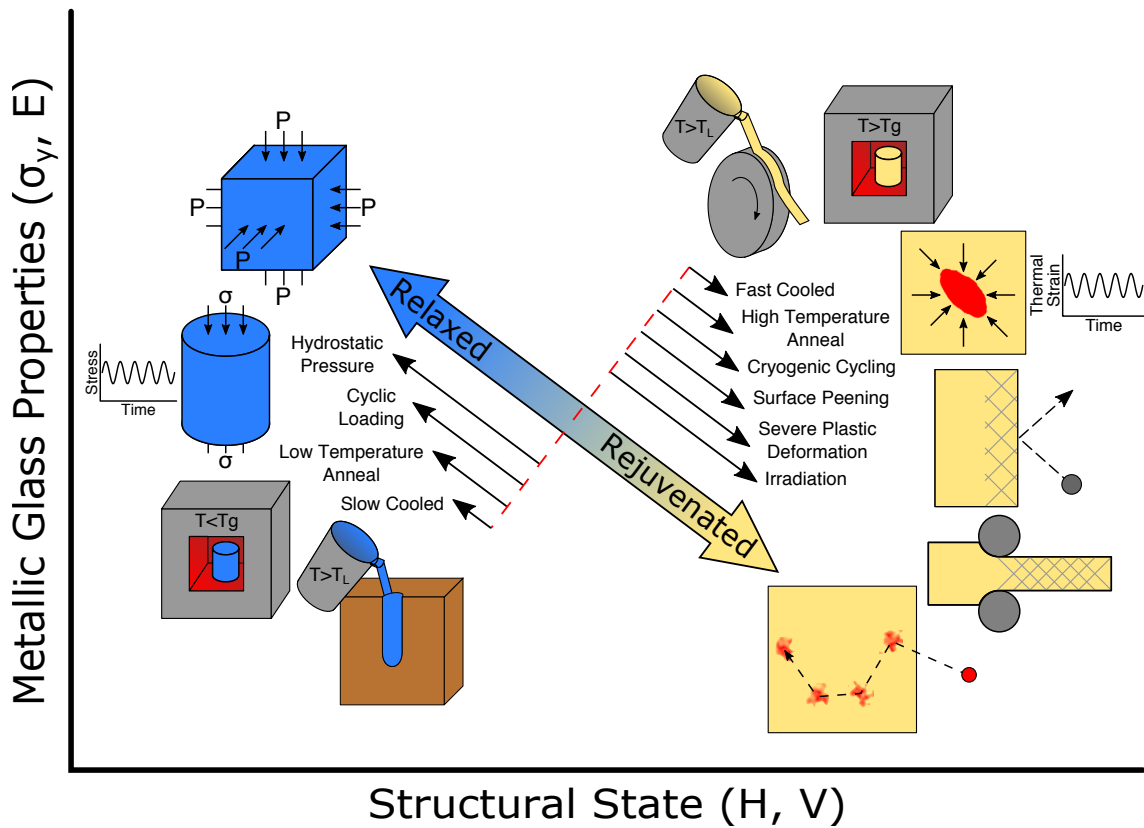


Figure 1.9: Illustration of relationship between metallic glass properties, such as yield strength (σ_y or Young's modulus (E), and structural state, as indicated by excess enthalpy (H) or free volume (V), for different relaxation and rejuvenation processes. Here prototypical relaxation processes are illustrated and include slow cooling by copper mold casting, annealing below T_g , cyclic loading at small elastic strains, and large hydrostatic pressures. Similarly potential rejuvenation treatments are showing including fast cooling by melt spinning, annealing above T_g , cycling to cryogenic temperatures, surface peening, severe plastic deformation such as cold rolling, and irradiation with high energy particles.

Table 1: Summary of metallic glass relaxation treatments.

Method	Description	Canonical Result	References
Slow Cooling Rate	Slow cooling rates result in kinetic freezing at lower temperatures	Produces relaxed structures with lower excess enthalpy, higher modulus and strength, and decreased ductility.	56, 57, 81, 137–143
Sub- T_g Annealing	Low temperature annealing enables structural relaxation on long time scales	Reduces excess enthalpy resulting in embrittlement and enhanced modulus and strength and reduced ductility	17, 45, 58, 78, 79, 83, 85, 86, 91, 144–163
Cyclic Elastic Loading	Small cyclic strains activate STZs	Operation of isolated STZs annihilates free volume leading to relaxation and greater median pop-in loads.	107, 164–178
Hydrostatic Pressure	Applying large hydrostatic pressures promotes densification. Elevated temperatures accelerate this process	Reduces free volume and excess enthalpy leading to higher strengths	77, 148, 179–192

Table 2: Summary of metallic glass rejuvenation treatments.

Method	Description	Canonical Result	References
Fast Cooling Rate	Fast cooling rates result in kinetic freezing of the liquid at higher temperatures	Produces rejuvenated structures with higher excess enthalpy, lower modulus and strength, and increased ductility.	56, 57, 81, 137–142

Annealing Above T_g	High temperature annealing followed by a rapid quench preserves high temperature liquid structures	Increases excess enthalpy resulting in increased plasticity and reduced modulus and strength	85, 91, 151, 193, 194
High pressure torsion	High pressures allow accumulation of large torsional plastic strains	Large plastic strains produce free volume and highly rejuvenated structures	46, 49, 50, 60–62, 195–201
Cold working	Drawing and rolling produce high strains under confinement	Creates a high density of shear bands resulting in decreased strength and increased ductility	44, 58, 76, 78, 80, 121, 159, 163, 202–221
Equal Angle Channel Extrusion	Produces uniform shear strains through multiple passes with no shape change	Produces free volume depending on the angle and number of passes resulting in rejuvenation	222–224
Surface Peening	High energy impact by shot or laser imparts heavy damage to the surface	Induces a high density of shear bands in the near surface region which may result in bulk changes in ductility is strength	225–241
Irradiation	High energy particles result in knock-on damage and the formation of local regions with extremely high effective cooling rates	Imparts large free volume changes observed as net volume changes, decreased strength and suppression of shear bands	242–261
Cryogenic Cycling	Thermal expansion mismatch between high and low free volume regions produces large local strains	Increases plastic strain with increasing cycles while excess enthalpy peaks at 10-15 cycles	262

1.4.1. Relaxation

A relaxation process is any treatment that reduces the enthalpy stored in the glass structure. The reduction of stored enthalpy is accompanied by a densification of the structure^{45, 78, 79, 144–146}. As a result, relaxed MGs typically exhibit increased elastic moduli and yield strength^{17, 147–150}. However, these gains come at the expense of ductility^{91, 151, 152}. Typically, structural relaxation is accomplished by annealing below the glass transition for extended periods of time; the time necessary for complete relaxation scales exponentially with temperature difference from T_g ^{83, 144, 153}. The effect of relaxation on the glass enthalpy is shown in Figure 1.10. Here the as-cast glass (black triangles) evolves more enthalpy around T_g and does not follow the supercooled liquid cooling curve. In contrast the relaxed glass (open circles) evolves less enthalpy and closely matches the supercooled liquid cooling curve in the temperature window considered here. This suggests a lower effective cooling rate in the relaxed glass as compared to the as-cast glass since it follows the supercooled liquid to lower temperatures. The relaxation applied to treatments are summarized in Table 1.

However, relaxation is not limited to thermal processes. Recently, mechanical treatments have been demonstrated to produce a relaxation response. For instance, spherical nanoindentation studies showed that cyclic loading at low loads changed the distribution of first pop-in loads^{164, 165}. In the as-quenched glass a wide distribution of pop-in loads was observed. As the number of elastic pre-loads increased the distribution of pop-ins tightened and shifted to greater loads. This process is illustrated

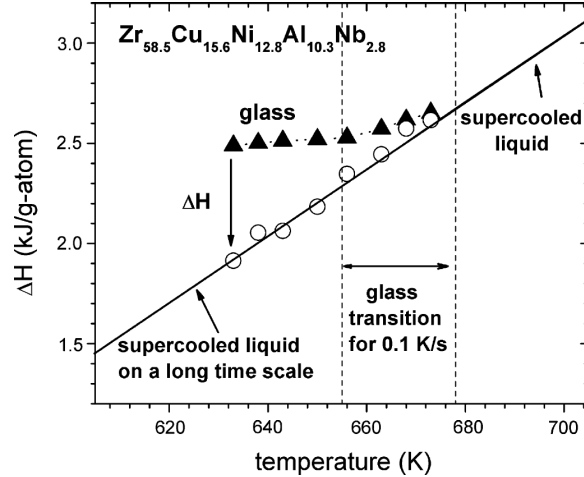


Figure 1.10: From Ref. 83, the enthalpy response of a metallic glass near T_g is shown. Here, the as quenched glass (black triangles) evolves more enthalpy when heated through T_g . In contrast, the relaxed glass (open circles), evolves less enthalpy and collapses onto the supercooled liquid cooling curve. Copyright 2007, with permission from Elsevier.

in Figure 1.11. Similar results were found in pillar compression fatigue measurements, which also identified densification from the x-ray diffraction measurements¹⁶⁶. MD and finite element studies further support this observation of relaxation by cyclic loading^{107, 167–170}. In these studies, cyclic loading stimulates deformation in regions of high free volume, effectively exhausting the easily deformed regions and annihilating free volume. However, the magnitude of the elastic strain plays a role. In cases of large cyclic strains, that are still less than the global yield strain, a tendency to soften emerges^{170, 263}.

Application of large hydrostatic pre-stresses is also effective at relaxing glass structures. Hydrostatic loading promotes densification, resulting in reduced stored enthalpy and increased yield strength, a clear indicator of structural relaxation^{77, 179–181}.

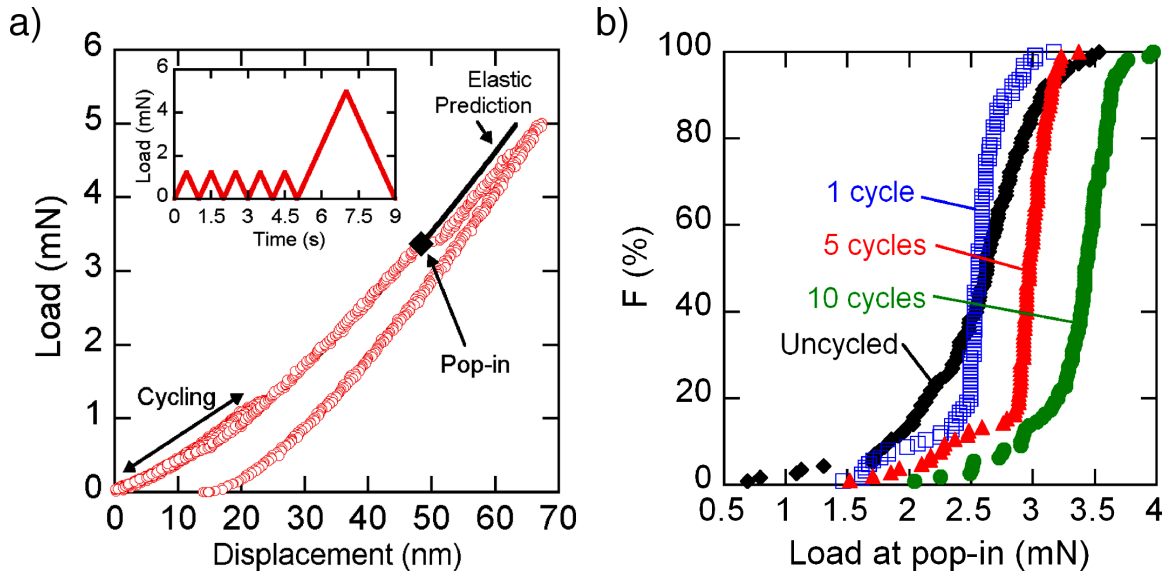


Figure 1.11: From Ref. 164, a) example of the spherical nanoindentation process. The load-displacement curve shows the cyclic preloading well below the first pop-in load as indicated by the deviation from the elastic loading prediction (black line). The inset shows the applied load profile. In b) the cumulative distribution of first pop-in loads for uncycled, 1 cycle, 5 cycles, and 10 cycles is shown. As the number of cycles increases the distribution shifts to higher loads and tightens. Copyright 2008, with permission from AIP Publishing LLC.

Furthermore, when hydrostatic pressure is coupled with elevated temperatures the relaxation process is accelerated^{148, 182} while crystallization may be hindered due to decreased diffusivity¹⁸³. However, hydrostatic loading is not universally effective. While pressure may stabilize an amorphous structures, in some alloys large pressures resulted in stress induced crystallization¹⁸⁴.

1.4.2. Rejuvenation

The converse response is a rejuvenation process. Potential rejuvenation treatments are summarized in Table 2. During a rejuvenation treatment the enthalpy

stored in a glass structure and the free volume is increased^{49, 78, 198}. As a result a rejuvenated glass exhibits decreased elastic moduli and yield strength^{151, 193, 198}. Additionally, rejuvenation treatments are effective in enhancing the capacity for plastic deformation^{91, 151}. Again, thermal processing is the canonical route to rejuvenation. To rejuvenate a glass it is annealed above the glass transition in the supercooled liquid region. The supercooled liquid is then quenched into the glassy state^{193, 194}. In this case, the degree of rejuvenation depends on the annealing temperature and quench rate; higher temperatures and faster quench rates produce more liquid-like, rejuvenated structures¹⁹⁴. The rejuvenation process is shown in Figure 1.12 by the increasing enthalpy with increasing quench rate.

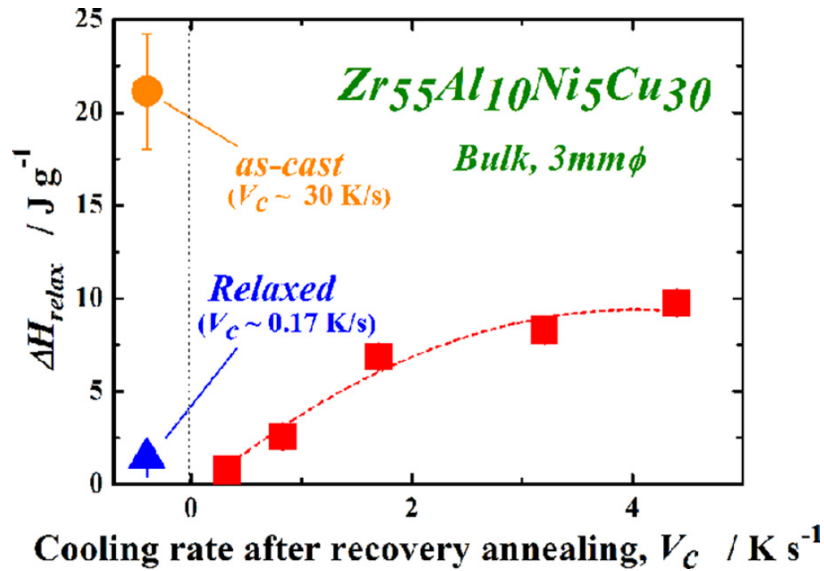


Figure 1.12: From Ref. 193, a metallic glass is rejuvenated by annealing above T_g then quenching into the glassy state. The degree of rejuvenation is indicated by the increasing enthalpy of relaxation and is controlled by the annealing temperature and the ensuing quench rate. Copyright 2013, with permission from AIP Publishing LLC.

Similar to relaxation, rejuvenation may also be accomplished by non-thermal

routes. One attractive route is through mechanical treatments that introduce non-affine strains by activating many STZs. Widely examined mechanical treatments include severe plastic deformation processes (SPD), such as cold working^{44, 58, 76, 78, 202–214}, high pressure torsion (HPT)^{46, 49, 50, 60–62, 195–198}, or equal channel angular extrusion (ECAE)^{222–224}. In these methods, confinement suppresses catastrophic failure and enables the accumulation of large plastic strains through copious shear banding^{46, 49, 50, 62, 76, 198, 214}. Recently, as MGs attracted renewed interest cold rolling and HPT have been extensively examined as a means to control shear band mediated deformation by rejuvenating the structure. This rejuvenation effect is observed in subtle changes to the radial distribution function^{49, 50, 58, 61} as well as significant changes in the stored enthalpy and mechanical properties^{44, 50, 196, 198, 206, 211, 212, 214}. The effects of SPD are shown in Figure 1.13. When subjected to HPT both the hardness and modulus decrease with increasing number of rotations. This reduction in mechanical properties is accompanied by an increase in relaxation enthalpy.

High energy surface treatments, such as shot and laser peening, may also induce a strong rejuvenation effect. Subjecting the surface to shot peening produces a high density of shear bands at the surface^{225–232}. As a result, the indentation hardness is reduced^{226, 229} and enhanced capacity for plastic deformation is observed²³⁰. However, the peening process is highly temperature sensitive. For instance, peening at cryogenic temperatures has been shown to enhance deformation induced rejuvenation²²⁷ or promote deformation induced crystallization²³⁴ depending on glass composition and the

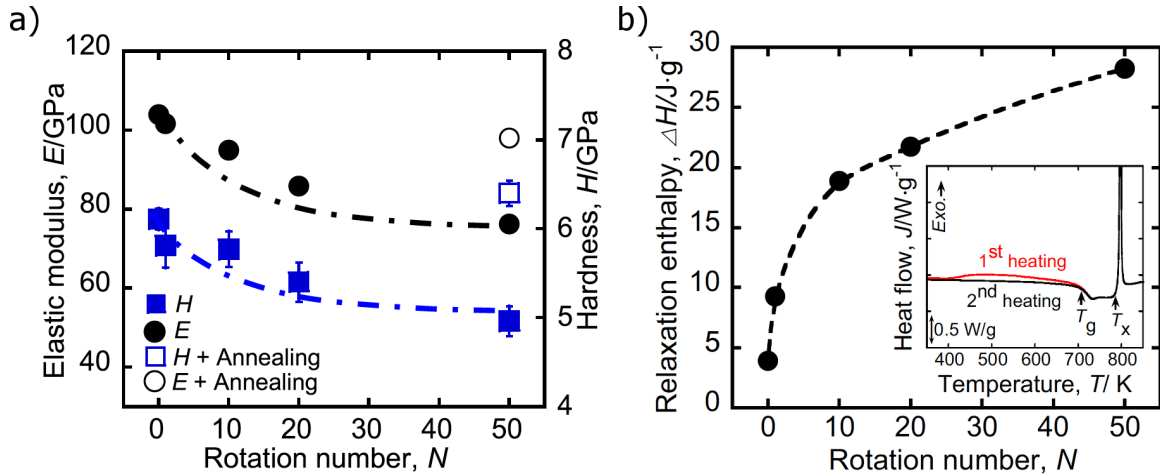


Figure 1.13: From Ref. 198, in a) the effect of increasing number of high pressure torsion rotations is shown. As the number of rotations increases both the hardness and modulus decrease. However, the as-cast properties are recoverable by annealing after severe deformation (open symbols). The changes in mechanical properties are accompanied by changes in relaxation enthalpy as shown in b). As the number of rotations increases the relaxation enthalpy increases from less than 5 J/g to nearly 30 J/g . Copyright 2012, with permission from AIP Publishing LLC.

thermal history. Similarly, laser shock peening induces significant surface deformation by generating large shock pressures^{233, 238–241}. As a result, the hardness near the laser shocked region is reduced but remains unchanged in material well removed from the damage site.

Similarly, when irradiated by high energy ions or neutrons a MG is rejuvenated by knock-on damage. MD simulations suggest that collisions between impinging ions and the target atoms produces a localized thermal spikes leading to a high density of “liquid-like” clusters and increased free volume^{242–248}. Macroscopically, large reductions in strength, suppression of shear banding, and improved ductility are observed^{249–254}. These changes in mechanical response are coupled to a reduction in density (increased

free volume) and increased energy stored in the glassy structure^{242, 243, 255–257}.

Finally, thermal cycling to cryogenic temperatures has recently been reported to produce a rejuvenation effect²⁶². After repeatedly quenching to liquid nitrogen temperatures and then heating to room temperature, the excess enthalpy of the system increased and multiple thermal relaxation peaks appeared before the glass transition temperature. In conjunction, the distribution of hardnesses shifted to lower hardness and an enhancement in plastic strain was found. This effect was hypothesized to emerge due to thermal expansion mismatches between the initial population of local soft spots and the surrounding matrix leading to large local non-affine strains upon cooling²⁶². As a result thermal cycling leads to localized plasticity around soft spots and increases the population of available deformation sites. Interestingly, the excess enthalpy reaches a maximum and decreases with additional thermal cycles. Yet the hardness saturates at a lower hardness while the plastic strain continues to increase.

1.5. Small Scale Metallic Glass Deformation

While processing history has been shown to strongly affect the mechanical response in MGs, reduction of specimen size to small length scale has recently been explored as an alternative route to controlling shear band and MG deformation. Following initial findings by Guo *et al.*²⁶⁴ that simply reducing specimen size suppresses shear bands, microscale and nanoscale dimensions have been explored as a route to controlling shear bands. Numerous follow up investigations observed a transition from shear

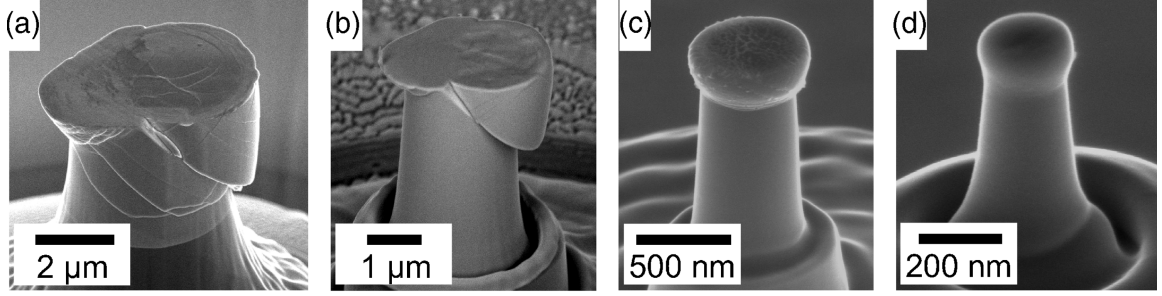


Figure 1.14: From Ref. 265, as the MG pillar diameter decreases the deformation is observed to transition from shear band dominated at a) $3.61 \mu m$ and b) $1.84 \mu m$ in diameter to quasi-homogeneous, with an absence of shear bands, at c) $440 nm$ and d) $140 nm$ in diameter. Copyright 2008, with permission from AIP Publishing LLC.

bands at large sizes to homogeneous flow, akin to high temperature deformation, below a critical length scale^{265–270}. Figure 1.14 shows example failure morphologies that transition from shear band dominated to an absence of shear bands when the pillar diameter is reduced to less than $\sim 1 \mu m$ ²⁶⁵.

To rationalize the observed size transition a theory analogous to the Griffith criteria for crack propagation was developed. In this formalism the elastic strain energy stored in the MG at the time of yield offsets the energy penalty to form a shear band (Equation 1.1)²⁶⁵. Here, σ is the applied stress, ε is the strain and $\pi r^2 L$ is the specimen volume, $\sqrt{2}\pi r^2$ is the shear band area assuming 45° inclination, and Γ is the shear band energy per unit area. Solving for stress gives the critical stress (σ_c) for forming a shear band as Equation 1.2, where the elastic modulus (E) is substituted for σ/ε .

$$\frac{\pi \varepsilon \sigma r^2 L}{2} = \sqrt{2} \pi r^2 \Gamma \quad (1.1)$$

$$\sigma_c = \sqrt{\frac{2^{3/2}\Gamma E}{L}} \quad (1.2)$$

The criteria for shear band formation is illustrated in Figure 1.15. As the specimen size decreases less elastic energy is available to offset the energy required to form a shear band. As a result, the critical stress increases. However, the intrinsic strength of the MG is proposed to be independent of size. As a result, below a critical size, the stress necessary for forming a shear band surpasses the intrinsic strength of the MG. Under this condition, deformation must proceed homogeneously until the stress reaches the shear band nucleation stress or fracture occurs.

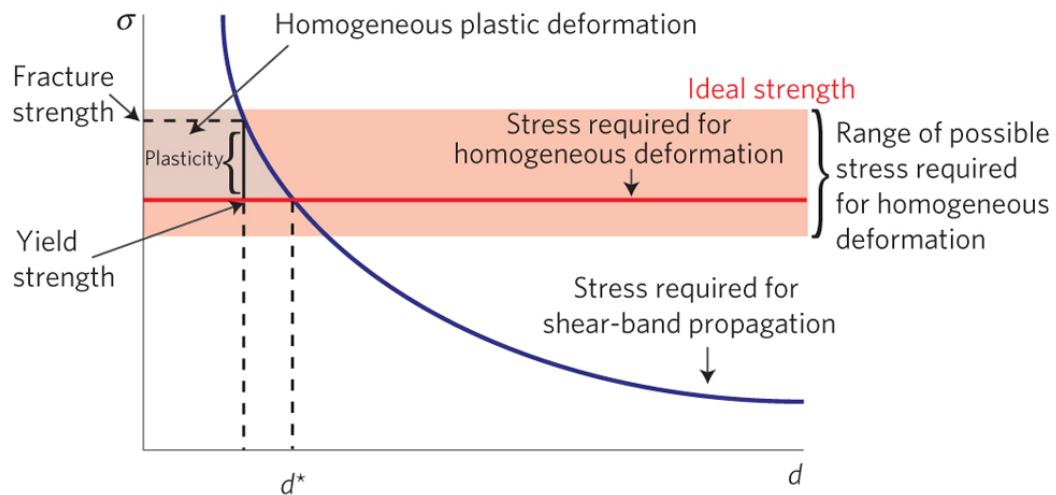


Figure 1.15: From Ref. 267, the criteria for suppression of shear bands due to reduced specimen dimension is shown. As the specimen size decreases, the stress for form a shear band increases until it exceeds the intrinsic strength of the MG. Copyright 2010, with permission from Nature Publishing Group

However, while the simple model for shear band formation has gained wide acceptance, many contradictory observations have been made. For instance, Schuster

et al. observed shear bands in pillars with diameters approaching 250 nm, well below the predicted critical length scale^{271, 272}. Similarly Tian *et al.*²⁷³, Wang *et al.*²⁷⁴ and Chen *et al.*²⁷⁵ found shear bands in sub-micron tensile specimens. Finally, Tönnies *et al.* studied both size and strain rate effects and found an interplay between size and strain rate effects²⁷⁶.

Given the strong processing sensitivity, the discrepancies in mechanical behavior at sub-micron length scales is unsurprising. Until recently, the majority of micromechanical studies on MGs employed focused ion beam (FIB) milling to fabricate test samples. However, irradiation has been shown to alter MG structures and properties according to experiments and MD simulations^{242, 249, 255, 256, 277}. Thus the convolution of potential size and processing effects are challenging to separate. This motivates a significant amount of the work reported in this thesis.

1.6. Overview

In summary, the unique processing sensitivity of metallic glasses, which stems from the glass formation process, was considered. Broadly, MG processing routes may be described as either relaxing or rejuvenating the glassy structure. Yet a tractable and consistent method for comparing structural changes resulting from different processing routes remains absent. Nowhere is the gap in quantifying processing effects more prevalent than in the recent study of micro- and nanoscale MGs, where the FIB employed to fabricate test samples may drastically alter the material response.

However, the literature suggests strong correlations between excess enthalpies and the mechanical response in bulk MGs. As a result, excess enthalpy offers a potential method for quantifying structural state – processing – property relationships in metallic glasses. Therefore, the overarching goal of this dissertation is to determine the interplay between size and processing on micro- and nanoscale MGs. In the following chapters, mechanical property measurements will demonstrate that reduced length scales enhance processing sensitivity and provide access to a greater range of structural states. Furthermore, to quantify the interplay processing sensitivity, a structural state – property relationship will be developed.

Thus in this dissertation, a study of the effect of processing history on the mechanical properties of MG nanowires and sputtered thin films will be presented. First the nanomechanical testing methods, particularly the production and harvesting of MG nanowires, a custom nanomechanical testing apparatus, and the production and testing of MG thin films, will be described in Chapter 2. Subsequently, the effect of both irradiation and annealing on the tensile response of MG nanowires will be presented in Chapters 3 and 4. Based on these experimental observations, a model for glass strength based on glass structural descriptors will be developed in Chapter 4. In addition, Chapter 5 examines the high temperature thermomechanical response of MG nanowires to gain further insight on the potential interplay between size and processing. In Chapter 6, the effect of deposition temperature on the mechanical properties of sputtered thin film MGs will be examined as a method to determine

properties at the time of glass formation with a wider range of accessible structures. Finally, we conclude by summarizing the major findings from this thesis and outline future experimental directions in Chapter 7.

Chapter 2

Materials and Methods

Portions of this chapter have been reproduced with permission from Scientific Reports, Volume 3, Page 16 (Copyright 2013 Nature Publishing Group), Acta Materialia, Volume 74, Page 165 (Copyright 2014 Elsevier), and Scientific Reports, Volume 6, Page 19530 (Copyright 2016 Nature Publishing Group).

When studying materials mechanics at the micro- and nanoscale many of the methods are functionally similar to macroscale testing. However, unique challenges often arise, such as how to prepare specimens for testing or how to apply and measure forces. To overcome these challenges, new equipment and methods must be developed. As such, a considerable portion of the work described here surrounds the development and implementation of new nanoscale testing methods, as is detailed in the following sections. First, the fabrication, preparation and testing of MG nanowires under a variety of conditions will be described. Considerations for evaluating the accuracy of these methods are also presented. Second, ion irradiation methods to vary the structural state in MG nanowires are presented, as well as supporting methods to characterize the structural impact of ion damage. Finally, the deposition, characterization, and mechanical testing of MG thin films will be described.

2.1. Tensile Testing of Individual Nanowires

2.1.1. Nanowire Fabrication and Harvesting

Nano-mechanical testing was performed in situ on $\text{Pt}_{57.5}\text{Cu}_{14.3}\text{Ni}_{5.7}\text{P}_{22.5}$ nanowires. The Pt-glass nanowires were fabricated through thermoplastic molding by G. Kumar and J. Schroers at Yale University using methods previously described in²⁶. Briefly, the nanowires were molded in a nanoporous alumina template at 270 °C under an applied pressure of 130 MPa. After molding, the alumina template was etched in KOH to leave free standing nanowires. The resulting nanowires had diameters between 90 and 160 nm with nominal testing gage lengths of 3 μm . The molding processes is illustrated in Figure 2.1²⁵⁹.

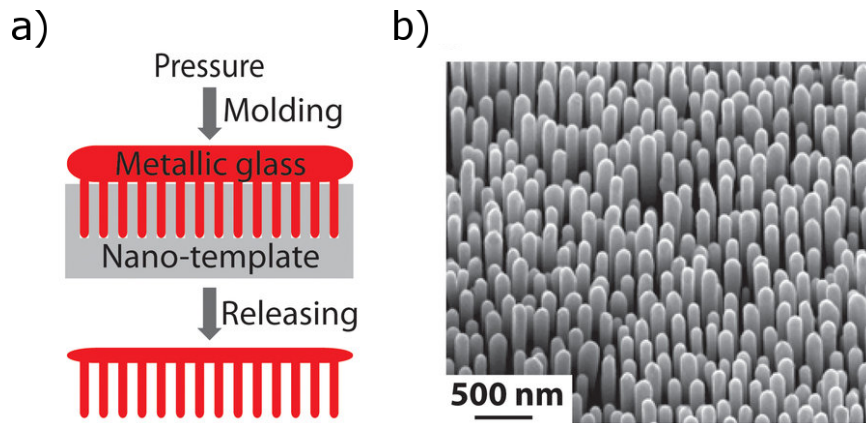


Figure 2.1: a) Pt-glass nanowires are produced by thermoplastic molding at temperatures above T_g . After molding the the mold is etched to release the Pt-glass nanowires. An array of molded nanowires after releases is shown in b).

The Pt-glass nanowires were subsequently mounted to specially prepared AFM cantilevers. Using the FIB, the cantilever end was removed and trenches were milled

parallel to the cantilever axis to aid in nanowire alignment. Using a nanomanipulator (Kleindiek) in a scanning electron microscope (FEI Quanta 600 FEG Mark II), nanowires were harvested and secured to the prepared cantilever using a Pt-based electron beam induced deposition (EBID) material. This process is shown in Figure 2.2.

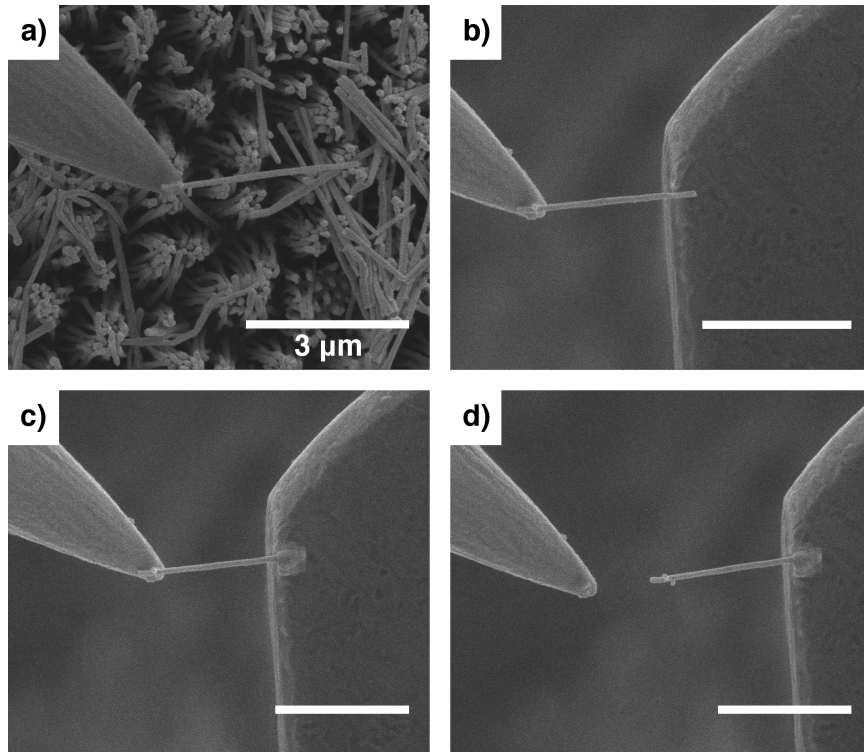


Figure 2.2: In the SEM MG nanowires are harvested by a) placing a probe beneath the desired nanowire. Free hydrocarbons in the chamber are deposited to form a weak bond between the nanowire and probe to enable the nanowire to be removed from the surface. b) After lifting from the substrate the nanowire is transferred to a new substrate for specimen mounting and is brought into contact. c) Pt-EBID is used to anchor the nanowire. d) the probe is removed.

2.1.2. *In situ* Nanomechanical Testing

Quantitative uniaxial tension nanomechanical tests were performed *in situ* in a dual beam SEM/FIB (FEI Strata DB235) using a custom testing platform. The platform, pictured in Figure 2.3, consisted of a closed loop six degree of freedom (DOF) stage (SmarAct GmbH), a stiff linear piezoelectric actuator (Physik Instrumente), and a MEMS based load cell (FemtoTools). The 6 DOF stage allowed for alignment of the sample and load sensor with nanometer accuracy. The actuator provided displacement control with a displacement range of $60\ \mu\text{m}$ and sub nm resolution. The load cell was capable of measuring forces up to $100\ \mu\text{N}$ with $<10\ \text{nN}$ noise under high vacuum.

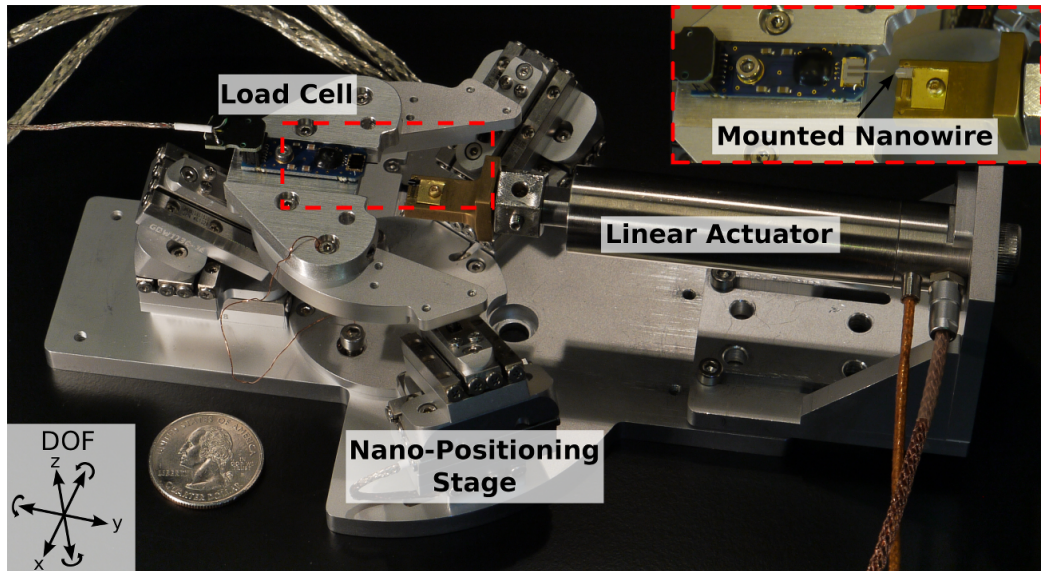


Figure 2.3: The nanomechanical testing platform with the translational and rotational degrees for freedom indicated. A quarter is shown for scale. The inset shows an expanded view of the load cell and sample mount.

To perform a tensile test, the sample was placed on the linear actuator and

aligned with the load cell using the 6 DOF stage. The wire was secured to the load cell using the Pt-based EBID. The nanowire was then strained at a nominal strain rate of $5 \times 10^{-4} \text{ s}^{-1}$ while simultaneously recording load and images of the test. After testing, digital image correlation (DIC) was used to extract strain measurements from the image sequences. Markers placed on the grips were tracked to determine the strain^{278, 279}.

2.1.3. High Temperature Creep Measurements

The thermomechanical behavior of individual metallic glass nanowires was measured in situ in the SEM by adapting our previously reported nanomechanical testing methods (Figure 2.3)^{259, 260}. Individual nanowires were mounted on a copper TEM half grid using Pt-containing electron beam induced deposition (EBID) material to ensure a strong mechanical mount and to allow electrical contact with the nanowire. After manipulating nanowires to a TEM half grid using in situ pick-and-place methods in an SEM with a nanomanipulator (Kleindiek Nanotechnik GmbH), the conductive TEM grid electrically isolated from the testing apparatus by mounting to a custom PEEK sample holder. A compliant copper wire was used to electrically contact the TEM grid and hence the nanowire samples. Electrical feedthroughs allowed access to an external source measure unit (Keithely 2636A), which was controlled by a custom Labview program. Current was sourced from the load cell, which was held at reference ground, to the TEM half, which was negatively biased, such that a constant power

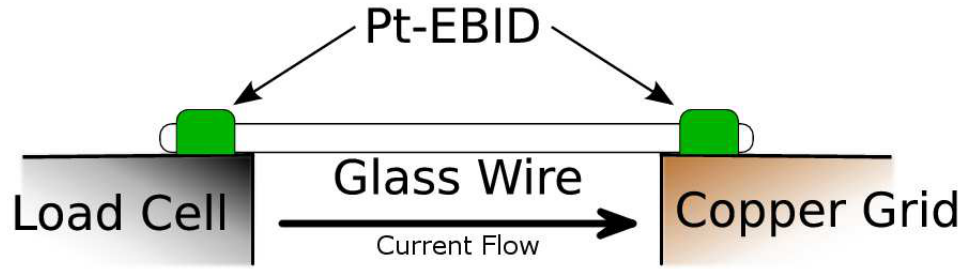


Figure 2.4: A schematic of the testing configuration is shown where a nanowire is gripped between the load cell and a TEM half grid with Pt-based EBID. An electrical current can then be passed from the load cell to the half grid

was dissipated in the nanowire.

In situ creep tests were then conducted in the SEM by bonding the free end of a nanowire to the load cell with Pt-based EBID to complete the load train and electrical circuit. Constant load and constant power dissipation were maintained using proportional-integral-derivative (PID) control; the standard deviation of the load during hold periods was approximately 90 nN. Over the course of a test the power dissipation and/or load were progressively increased while periodically capturing images in the SEM. When programming the PID controller, the feedback was intentionally slowed down in an effort to prevent mechanical or thermal instabilities. SEM image sequences were simultaneously captured and subsequently processed to calculate axial strains using digital image correlation techniques in which Pt-EBID fiducial markers were tracked throughout the image sequence²⁷⁸. The experimental setup is illustrated schematically in Figure 2.4.

Strain was then calculated by tracking the positions of Pt-based EBID fiducial

markers using digital image correlation techniques. After taking a sub image containing a single fiducial marker, a Gaussian was fit to the average x and y profile as shown in Figure 2.5. The marker coordinate is then determined as the peak position of the x and y profile fits. Tracking was accomplished by using the fit to the marker profile from the previous frame as the initial condition for fitting the marker profile in the current frame. The tracking resulted in a trajectory for each marker in both the x and y directions. The trajectories were used to calculate the displacement of each marker and the average displacement of the two grips. The trajectories also allowed the potential in-plane misalignment angle to be calculated for each frame. The true force along the nanowire axis was determined based on the resolved force and the potential in-plane misalignment angle. In this way in plane angles were explicitly accounted for. However, it is important to note that generally the angles were small and did not greatly affect the measurement. Critically, potential out of plane angles and displacements could not be accounted for and are a source of error.

Engineering strains were calculated as the change in nanowire length and accounted for displacement of the grips along the load train and laterally due to thermal drift. The first image of the testing sequence was used as the unstrained reference. Engineering stress was calculated by measuring the nanowire diameter before deformation and assuming a circular cross-section. Subsequently, true stress and strain were calculated by assuming uniform deformation and constant volume during plastic deformation.

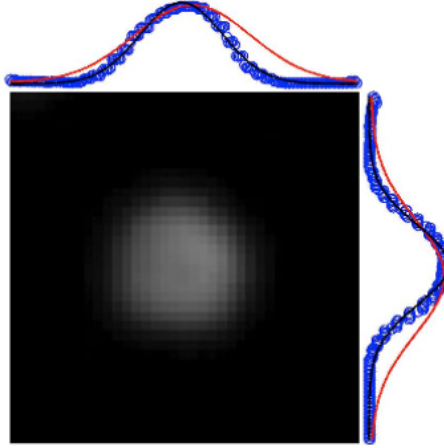


Figure 2.5: A schematic of the fiducial marker tracking method. A sub image containing a single marker is shown. The x and y profiles are shown as blue circles. An initial guess fit is included in red and the profile fit is shown in black. The marker coordinate is then given by the center of the x and y profile fits.

2.1.4. Estimate of Experimental Uncertainty

The primary sources of measurement error in our stress and strain calculations originate from the variance in diameter of the MG nanowire specimens, as well as noise in the load sensor and digital image correlation (DIC) strain measurement.

When possible the area cross sectional area was directly measured from SEM micrographs of the fracture surface. In such cases, an uncertainty in the cross sectional area was determined based on the variance of any electron beam induced deposition material present on the surface of the fracture nanowire. In cases when the fracture surface could not be directly imaged, the cross section of the MG nanowires was approximated as a circle (supported by top down SEM imaging of nanowire arrays) with a diameter, d . Several measurements (>10) were taken immediately after manipulation and preceding tensile testing. The typical variation in diameter for a

tensile testing specimen was approximately 10 nm.

The accuracy of DIC is limited by the pixel resolution of the SEM raster, the signal to noise ratio of the image (dictated by the electron beam dwell time), and the spatial frequency of image contrast variation. Tests performed in the SEM at 80,000 \times magnification or higher had a measured strain noise floor of $\Delta\varepsilon < 4 \times 10^{-4}$. The measured noise floor of the force sensor was $\Delta F \approx 10$ nN (30 Hz sampling rate).

We used the standard expressions for error propagation to calculate the error bars for strength. The engineering uniaxial strength is calculated as $\sigma = F/A$ where F is the force and A is the cross-sectional area directly measured from images of the fracture surface or as $A = 1/4\pi d^2$. Accordingly, we can use Equation 2.1 for the uncertainty of a quantity q that is a product and quotient of other quantities, i.e $q = \frac{r \times \dots \times w}{t \times \dots \times x}$ where the individual uncertainties are assumed to be independent and random²⁸⁰. As a result, the error in the stress measurement is determined as Equation 2.2

$$\frac{\Delta q}{q} = \sqrt{\left(\frac{\Delta r}{r}\right)^2 + \dots + \left(\frac{\Delta w}{w}\right)^2 + \left(\frac{\Delta t}{t}\right)^2 + \dots + \left(\frac{\Delta x}{x}\right)^2} \quad (2.1)$$

$$\frac{\Delta \sigma}{\sigma} = \sqrt{\left(\frac{\Delta F}{F}\right)^2 + 2\left(\frac{\Delta d}{d}\right)^2} \quad (2.2)$$

2.2. Ion Irradiation of Metallic Glass Nanowires

Nanowires were irradiated under a variety of conditions in a dual beam SEM/FIB to vary the irradiated volume fraction and ion fluence. Irradiated volume fraction was controlled by changing the Ga⁺ accelerating voltage of the FIB. To this end, accelerating voltages of 5, 15, and 30 kV were used. Stopping range of ion calculations (SRIM.org) were performed to determine the ion range and damage distribution at each accelerating voltage. Each simulation used 10,000 ions and full damage cascades were calculated. Figure 2.6c-e shows the calculated ion range and damage distributions as well as the irradiated volume fraction calculated using an assumed damage cross section shown in Figure 2.6b. The ion stopping ranges were calculated to be 2.4 nm, 4.7 nm, and 7.6 nm for 5 kV, 15 kV, and 30 kV respectively. To irradiate a nanowire, the electron and ion beams were aligned well away from the sample to ensure that the beams were focused at the same point with the electron beam perpendicular to the nanowire. Then, using the electron beam the sample was located and a reduced scan was placed on the gage length, such that approximately 1 μm was exposed. Using a low beam current (10-30 pA) the ion beam was rastered over the nanowire a controlled number of times. This process is shown schematically in Figure 2.6a.

The experimental ion fluence (f) was calculated according to

$$f = \frac{INt}{qA_{pxl}n_{pxl}} \quad (2.3)$$

where I is the ion beam current, N is the number of times the ion beam was rastered over the sample, t is the ion beam dwell time, q is the elemental ion charge (i.e. for Ga^+ $q = 1$), A_{pxl} is the real area of a pixel, and n_{pxl} is the number of pixels. As a result, the ion fluence was controlled by varying the number of times the ion beam was rastered over the sample. Ion fluences ranging from 0 ions/nm^2 to $\sim 300 \text{ ions/nm}^2$ were used. In addition, the effect of structural relaxation annealing on irradiated wires was

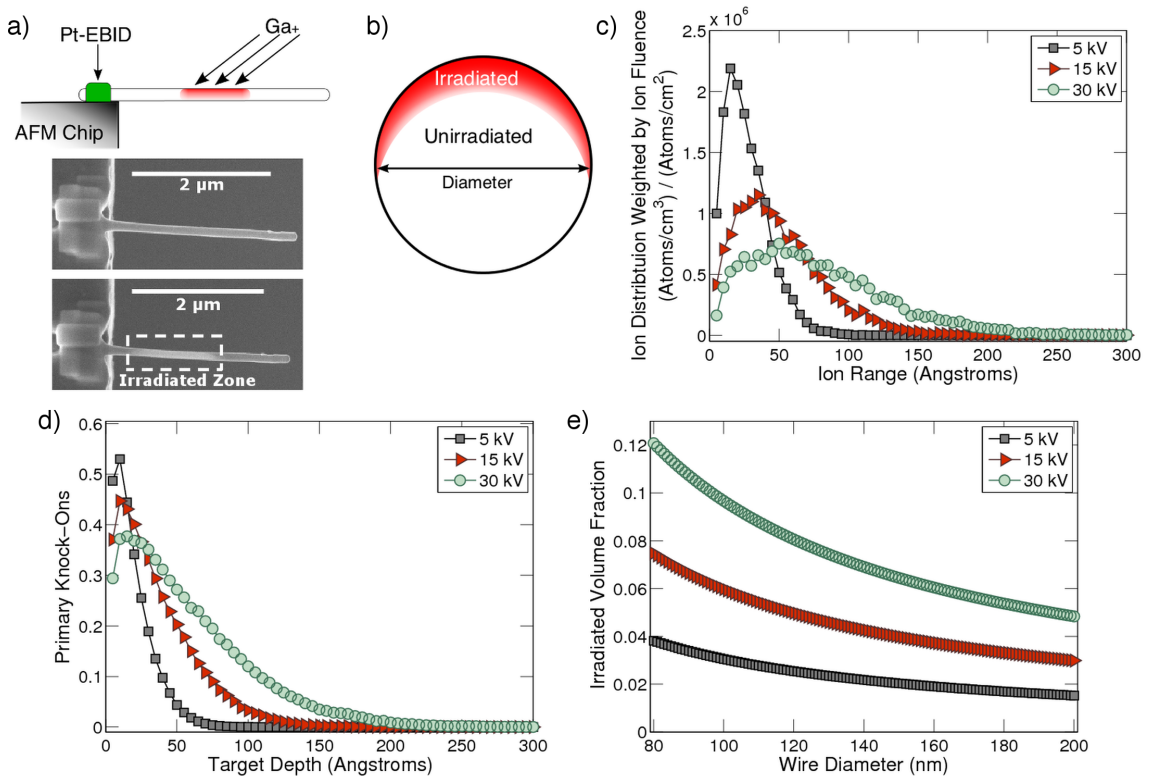


Figure 2.6: a) A schematic of the nanowire irradiation process. In the dual beam SEM/FIB a portion of the gage length is irradiated by a beam with an incidence angle of 38° with respect to the nanowire axis. The assumed cross section used to calculate the irradiated volume fraction is illustrated in b). The red region represents the irradiated material and the white area indicates the unirradiated volume. Results of ion stopping range calculations showing c) ion implantation range and d) distribution of primary knock-on damage. e) shows the calculated irradiated volume fraction for each accelerating voltage.

considered. Selected nanowires were irradiated with fluences between 115 and 145 ions/nm² and subsequently annealed at $0.96T_g$ for 70 minutes, conditions we previously showed to reverse the effect of ion irradiation on deformation mode²⁵⁹.

2.2.1. Characterizing Ion Damage in MG nanowires

Irradiated nanowires were characterized by selected area electron diffraction (SAED) to confirm the amorphous structure. Wires were mounted to TEM lift-out grids to eliminate possible background from carbon grids using the same harvesting process used to prepare tensile specimens. Diffraction patterns were obtained using a JEOL 2100 TEM with an accelerating voltage of 200 keV. Using SAED, a central portion of the nanowire was selected such that the lift-out grid and Pt-EBID did not contribute to the diffraction pattern. To analyze the diffraction patterns, the radial intensities were integrated. The limits of integration were selected to avoid contributions from the beam stop and the same limits of integration were used for all diffraction patterns.

For the quantification of the Ga content in both irradiated and as-molded nanowires atom probe tomography was used. Atom probe tomography was performed by P. Felfer and J. Cairney at the University of Sydney. In the atom probe, the nanowire is subjected to a high electric field, which is used to ionize and remove single atoms from the surface, which are then captured on a 2D detector and identified by their time-of-flight. This allows for precise compositional analysis of very small

volumes of material. For this purpose, nanowires were manipulated via the same methods used to prepare wires for tensile testing and welded with Pt-based EBID onto a support structure for analysis²⁸¹. The ends of the nanowires, which often showed structural irregularities, were cut off using a Ga FIB with an energy of 30 keV. As the atom probe data set was collected from this near-tip region, this implied that the Ga content measured systematically represented an upper limit of the actual Ga composition in tensile specimens. After processing in the FIB, some wires were then annealed before atom probe analysis under the same conditions used to structurally relax wires for tensile testing. The atom probe experiments were carried out in a Cameca LEAP 4000X Si instrument using 90 pJ laser pulses to trigger the field evaporation. The base temperature used was 60 K.

2.3. Sputtered Metallic Glass Thin Films

2.3.1. Deposition

DC magnetron sputtering was employed to deposit $\text{Pd}_{77.5}\text{Cu}_6\text{Si}_{16.5}$ from an alloy target. The target was produced by ACI Alloys Inc. from elemental sources with 99.99% (Pd source) and 99.999% (Cu and Si source) purity. Sputter deposition was performed in collaboration with X. Cheng and L. Ye at Bryn Mawr College in an ATC Orion series magnetron sputter deposition system (AJA International Inc.). Following evacuation of the chamber to base pressures of $<5 \times 10^{-8}$ Torr, an argon plasma was

struck at a working pressure of 4 mTorr and a target power of 125 W. Thin films were deposited simultaneously on Si [100] and soda-lime glass slides.

To control glass structural state, thin films were deposited at varying substrate temperatures. The substrate was radiatively heated using a quartz lamp heater. The substrate temperature was monitored by a shielded thermocouple, which measured heat radiated back from the sample holder. To calibrate the true temperature of the substrate, irreversible temperature sensitive dots (Omega Label) were placed on the sample holder and observed while increasing the heater set point. Therefore, all reported substrate temperatures indicate the true deposition temperature and not the heater set point.

2.3.2. Characterization

The composition was primarily determined by energy dispersive X-ray spectroscopy (EDS) in a FEI Quanta 600 FEG Mark II using a EDAX Octane Super silicon drift detector. All spectra were taken at 5 kV and an incidence angle of 30° to ensure the electron interaction volume was fully contained by the thin film. The resulting spectra were analyzed using EDAX TEAM software suite.

To cross-validate the EDS analysis, MG thin films deposited under similar conditions were analyzed using Rutherford backscatter spectroscopy (RBS). RBS spectra were collected using a NEC Mini-Tandem accelerator operating at 2 MeV.

The RBS detector was calibrated using a spectrum taken from a Pb-doped aluminum oxide. The RBS spectra were analyzed using xRump and SimNRA analysis packages.

The structure of the thin films was observed through x-ray diffraction (XRD). A Rigaku Smartlab diffractometer was operated in a parallel beam geometry to collect $\theta-2\theta$ scans from 30 to 60 2θ from thin films deposited on soda-lime glass. To support the XRD analysis, FIB lift-outs were prepared from select deposition conditions. The lift-outs were observed in a JEOL 2100 transmission electron microscope operating in both bright and dark field conditions. Selected area electron diffraction patterns were also taken from within the thin film.

2.3.3. Assessing Deformation Response

The mechanical properties of the sputtered MG thin films was assessed by nanoindentation. An Agilent (now Keysight Technologies) G200 with XP module and diamond Berkovich tip was used to indent the thin films at a constant loading-rate-to-load-ratio of 0.05 s^{-1} . Depth resolved hardness and modulus were determined by the continuous stiffness method. Nanoindentation and analysis of indentation results were performed by G. Feng at Villanova University.

To observe the deformation morphology, the thin films were indented using a Hysitron Ti 950 Triboindenter equipped with a diamond Berkovich tip. All films were indented at a constant loading rate of $400 \mu\text{N}/\text{s}$ to maximum load of $2000 \mu\text{N}$.

The indent morphology was imaged using the *in situ* scanning probe mode under an applied load of $2\ \mu\text{N}$.

Chapter 3

Tunable Tensile Response of Molded Metallic Glass Nanowires

Portions of this chapter have been reproduced with permission from Scientific Reports, Volume 3, Page 16 (Copyright 2013 Nature Publishing Group).

In this chapter the role of size and processing in thermoplastically molded Pt-based MG nanowires is considered. We describe experiments that reveal a transition from brittle to ductile behavior and quasi-homogeneous plastic flow in nano-sized metallic glasses that originates from structural changes due to ion irradiation, and not directly from specimen size. The changes in the glassy structure resulting from high-energy ion bombardment coerce the MG into a new state that facilitates an entirely distinct mechanism for accommodating plasticity via quasi-homogeneous flow at room temperature. However, this altered state is reversed by annealing below T_g , which induces structural relaxation and returns the MG to a brittle state. The notion of structural changes leading to very different underlying atomic mechanisms and ensuing mechanical responses in glasses, initiated by ion irradiation and reversed by thermal processing, suggests new strategies for controlling the ductility of metallic glasses by suppressing shear band formation. This result mirrors observations of tunable mechanical response in bulk specimens and points to a potentially wider range of achievable response due to reduced dimensionality.

3.1. Nanowire Tensile Response

To gain direct and quantitative insight on the mechanical response and deformation morphology of our MG nanowires, we performed *in situ* tensile testing of individual nanowires at room temperature in a controlled loading geometry. Tensile stress-strain curves for molded nanowires are shown in Figure 3.1a (left panel) The representative tensile behavior for the as-molded nanowires involves linear elastic response until final fracture at strengths of 1.6 ± 0.4 GPa (bulk strength, 1.4 GPa)¹³⁴, which occurred without any detectable signs of gross plastic flow. Specifically, the mechanical behavior was characteristically brittle despite the relatively large range of elastic strain, which is common in MGs²⁷³. The measured tensile response corroborated the fracture morphology, which always occurred heterogeneously (in a localized manner) at angles near 50° with respect to the tensile axis Figure 3.1b, as is consistent with a pressure augmented shear stress failure criterion²⁸². As the cross-sectional areas were fairly constant over the tested lengths of the nanowires, fracture was found to occur at apparently random locations along the gage length, with no correlation between fracture location and strength. Our measurements of brittle tensile response in combination with observations of shear-localized fracture are consistent with the typical tensile response of macroscopic MGs specimens¹⁰, wherein heterogeneous failure driven by shear banding is the predominant deformation mode. However, both our compressive and tensile measurements starkly contrast with numerous reports of homogeneous plastic flow in submicron MG specimens, which in all cases were

prepared by FIB milling

We then considered the role of ion irradiation in preparing micro- and nano-scaled specimens. High-energy ion irradiation is known to impart structural changes in amorphous metals^{242, 255}, leading to measurable changes in mechanical behavior and shear band-mediated plastic response^{242, 250}. This is particularly true in micro- and nanoscale volumes, where the fraction of material altered by ion irradiation is necessarily large. Therefore, we subjected our nano-molded and mounted tensile specimens to ion irradiation *in situ* in a central portion of the gage section. A key advantage of these experiments is direct comparison of the mechanical response and plastic morphology of irradiated MGs to pristine nanowires of the same material and dimensions. The nanowires were subjected to focused Ga⁺ ion irradiation at 30 kV (incident angle 38° with respect to tensile axis) and ion doses varying from approximately 100–300 ions/nm² over a region approximately 1 μm in length. The tensile response is shown in Figure 3.1a (central panel). The measured mechanical behavior was markedly different from the as-molded nanowires, as characterized by clear plastic yielding and inelastic response. In addition to large proportional limits, post-yielding strains were measured to be as large as ~2%. In one case, measurable apparent strain hardening occurred, with yielding occurring at 1.7 GPa and a subsequent fracture stress exceeding 2.5 GPa (green curve in Figure 3.1a). While apparent strain hardening has been previously measured and argued on the basis of a sampling of shear band nucleation sites with increasing strength as deformation increases (i.e. extreme

statistics)²⁷³, other ion irradiated nanowires that we tested did not demonstrate such strain hardening. Nevertheless, the measurements of tensile ductility clearly contrast with the brittle response of as-molded nanowires. Most surprisingly, the fractured regions of the ion irradiated specimens (Figure 3.1c,d) demonstrated copious plastic flow as shown by thinning of the cross-section down to a fine point. Fracture always occurred in the irradiated section, presumably due to smaller cross-sectional areas resulting from removal of material in these regions via ion sputtering. Transmission electron microscopy images of the fractured regions (Figure 3.1d,f) confirm that plastic flow occurs over an extended region along the length of the irradiated region (i.e. quasi-homogeneously), often causing profuse necking down to a tip with a radius of ~ 5 nm. Both fractured ends of the ion irradiated specimens exhibit such morphology along the entire width of the specimen, which indicates a plastic deformation mechanism distinct from heterogeneous shear banding.

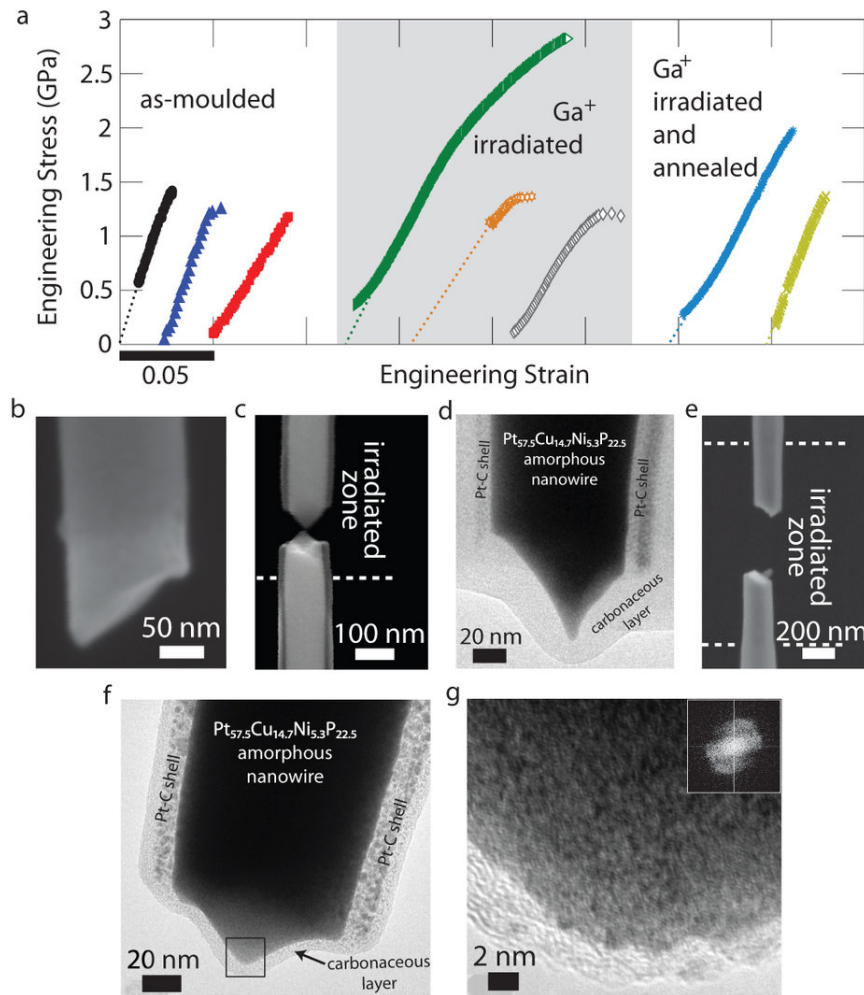


Figure 3.1: (a), Representative stress strain curves obtained from *in situ* tensile testing of as-molded, focused Ga⁺ ion irradiated, and irradiated and annealed ($T=0.96T_g$) nanowires with diameters ranging from ~ 100 - 150 nm. Ion irradiation induces changes to the material allowing for tensile ductility, in contrast to the brittle response measured in all as-molded nanowires. Upon annealing irradiated nanowires below T_g , subsequent tensile testing shows a return to the brittle state, suggesting the mechanical response may be tunable. The measured mechanical response is supported by different morphology for the different preparation conditions, shown in SEM images for: (b), as-molded, (c), ion-irradiated, and (e), irradiated and annealed fractured nanowires. (d), TEM image of deformed ion-irradiated nanowire, showing clear evidence of plastic flow in the irradiated region. (e), TEM image of the fracture site in a MG nanowire subjected to focused Ga⁺ ion irradiation at a dose of 305 ions/nm^2 showing ductile morphology following tensile testing. (g), high resolution TEM image showing heavily deformed ductile zone of fracture surface. No evidence of crystallization is observed, as confirmed by the FFT of the image (inset), suggesting that ductility is accommodated entirely by structural changes to the glass.

3.1.1. Role of Fracture Location

During the testing process, measures were taken to ensure a consistent loading geometry. While the common dog-bone geometry used in macro-scale samples was not employed, steps were taken to mitigate stress concentrations at the grips. There are two effects that mitigate such stress concentrations and add confidence to our experimental results. First, the nanoporous templates used for the molding process naturally result in slightly larger pore openings near the free surfaces, leading to slightly larger wire diameters ($\sim 10\%$ larger) near the ends upon etching of the template. As our manipulation procedures allows for accurate placement of the grips, we ensure proper placement of the uniform section of the nanowire to define the tensile gage section. Second, the electron-beam induced deposition of Pt-based grips generally results in slightly diffuse edges; a consequence of the Gaussian profile of the electron beam and finite mobility of the deposition species. As a result, our nanowire tensile specimens have a natural fillet geometry that minimizes stress concentrations near the gripping surfaces.

Nevertheless, we have taken steps to ensure the accuracy of our results and have analyzed the fracture sites as a function of measured fracture strength, as fracture near the grip could be a result of a stress concentration, lowering the apparent fracture strength of the specimen. Figure 3.2 shows a map of fracture strength as a function of size for the as-molded nanowires (with no dog-bone geometry), with the coloring denoting the fracture location. There does not appear to be any correlation between

the measured strength and the fracture site, suggesting that any degree of stress concentration near the grip is insufficient to control fracture (Figure 3.2). That the fracture sites are distributed at seemingly random locations along the wire length is expected for a brittle material where fracture is described stochastically.

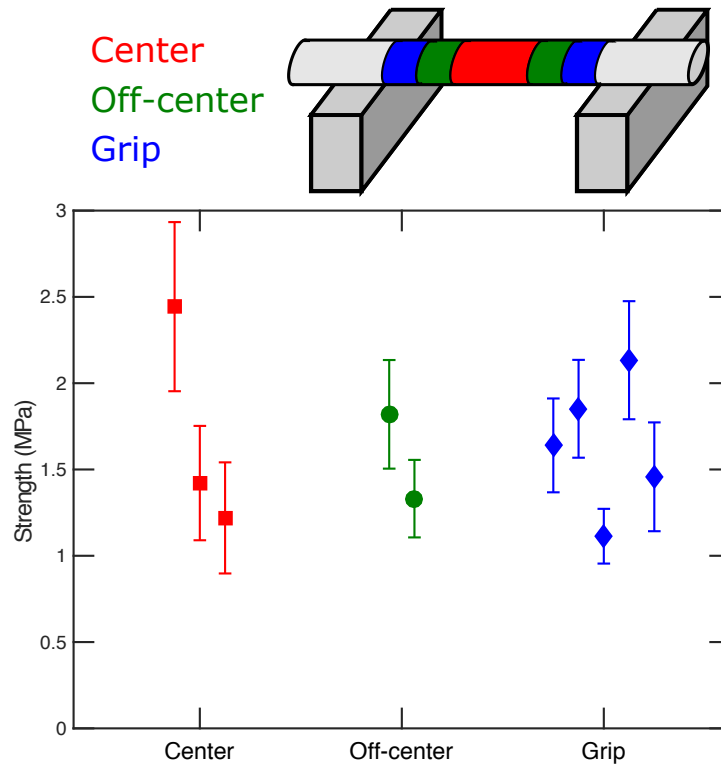


Figure 3.2: Nanowire fracture strengths are group by fracture location. No difference in strength is found between nanowires that fractured in the center, off-center, or the grip.

3.2. Discussion

These experimental results imply that indeed the mechanical response, ductility, and ensuing plastic failure mode can be reversibly transformed by way of structural

changes to the glass; a departure from recent reports claiming that size alone is responsible for such transitions. High-energy ion irradiation leads to measurable tensile ductility and quasi-homogeneous plastic flow, while subsequent sub-T_g annealing induces structural relaxation, returning the glass to a brittle state. The effect of fabrication methods and annealing on the MGs' plasticity, which has been correlated with Poisson's ratio (and accordingly G/B), has been observed in bending and compression geometries^{134, 142, 283}, but never for tensile ductility. Our findings indicate dramatic changes in the structure, beyond a mere reduction in shear localization tendency, to a liquid-like structure^{284, 285} in the irradiated MG. The salient implications of our findings are twofold. First, interpretation of recent reports of a transition between heterogeneous (shear banding) and homogeneous plastic flow in MGs with specimen sizes below several hundred nanometers is complicated by the influence of ion irradiation during specimen fabrication and is likely not representative of the as-cast structural state of the glass. The prevailing view supporting experimental observations of the suppression of shear localization in submicron MGs is that small volumes do not release sufficient elastic strain energy during shear banding to counter the energy penalty of shear disordering (analogous to Griffith theory for crack propagation). In this framework, the critical stress for shear band propagation can be derived to be $\sigma = \sqrt{2^{3/2}\Gamma E/L}$, where Γ is the shear band energy associated with atomic disordering within the small band, E is the Young's modulus, and L is the specimen length²⁶⁵. Comparing reports of transitions in plastic deformation

mode in FIB-made pillars^{250, 265–267, 269, 270, 272, 286–288} with our as-molded nanowires via the Griffith-like prediction for the onset of homogeneous flow (using the reported flow strengths and elastic moduli, and assuming a maximum shear disordering strain of unity and a 10 nm shear band thickness¹⁰), the observed deformation modes are consistent with this theoretical prediction (Figure 3.3a). However, our ion irradiated nanowires displaying tensile ductility and homogeneous flow (open green symbols) show behavior contrary to this prediction, well into the regime where heterogeneous behavior is predicted. Furthermore, changes to E and Γ owing to ion irradiation would likely lower the threshold for shear banding. Therefore, our experiments suggest a distinct mechanism for accommodating plastic flow.

Both liquids and glasses lack long-range structural order, yet liquids differ in their capacity for facile flow. Whereas cooling rates of bulk MGs sufficiently rapid to retain vestiges of the liquid state (known to suppress shear localization in deformed amorphous Si at room temperature²⁸⁵) are difficult to attain, ion irradiation of nanoscale volumes could introduce a substantial fraction of liquid-like states^{284, 285} that facilitate homogeneous plastic flow. At ion accelerating energies of approximately 30 kV, the penetration depth of ions was estimated to be approximately 9 nm (compared to 5 nm for glancing ion incidence for pillar fabrication) based on simulations of ion range (see Methods 2.2). Thus, the resulting volume fraction of structurally modified glass would scale with specimen diameter. Provided a structural change leading to a more liquid-like state in our irradiated MGs, the requisite structural contrast between

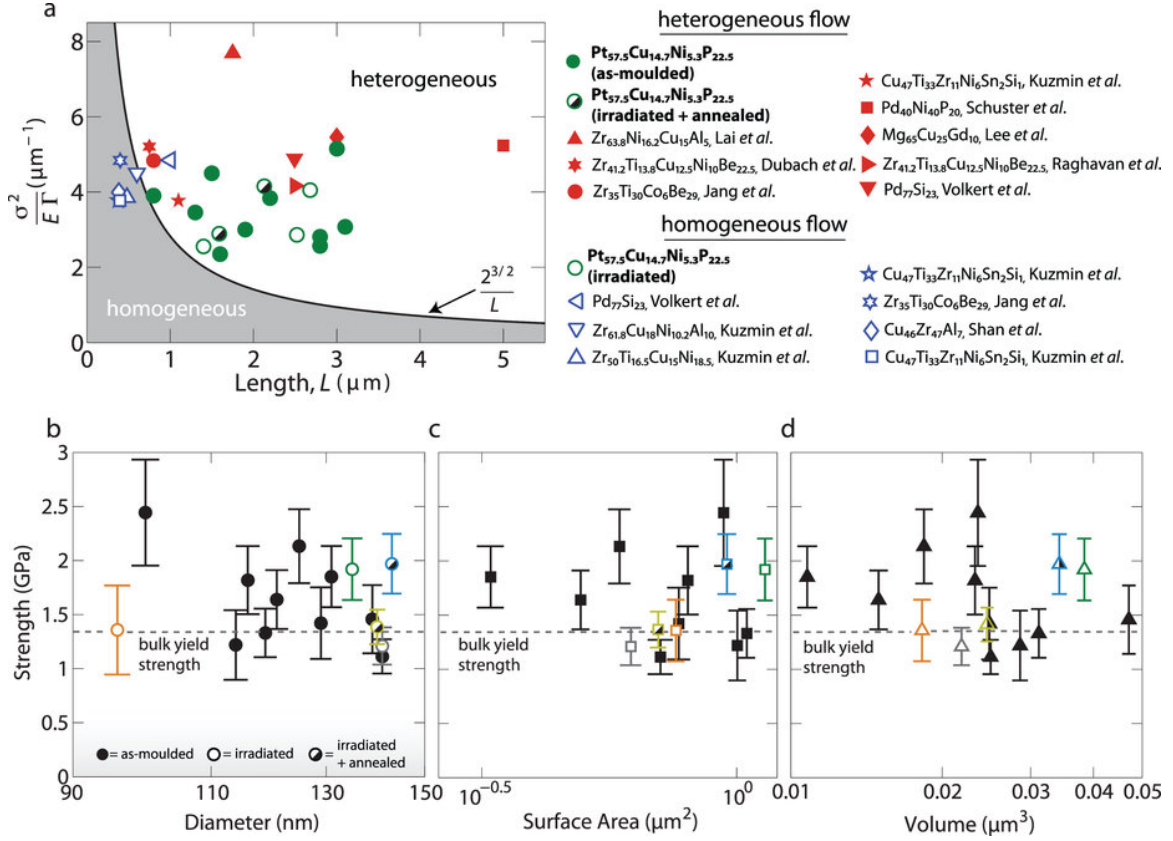


Figure 3.3: (a), Deformation mechanism map giving normalized metric for energy of shear band propagation vs. specimen length for our measurements (green symbols) and various metallic glass small scale experiments^{250, 265–267, 269, 270, 272, 286–288}, shown in comparison to the prediction of a size-dependent transition to homogeneous flow²⁶⁵. See text for details. While this theory predicts the transition for previous reports (homogeneous flow shown as open symbols), it fails to describe the tensile ductility observed in our ion irradiated molded nanowires (open green symbols), suggesting a distinct mechanism for accommodating plastic flow. Literature values are estimated by the mean stress for each deformation mode, and lower and upper limits for the length of specimens showing heterogeneous and homogeneous flow, respectively. (b), Measured strength of MG nanowires as a function of size, (c), surface area, and (d), volume. Closed, open, and partially filled symbols represent as-molded, ion irradiated, and irradiated and subsequently annealed (below T_g) nanowires, respectively. Fracture strength is plotted for nanowires showing brittle response (as-molded and irradiated and annealed), while 0.2% offset yield strength is shown for ductile nanowires (irradiated). No clear size effect is measured beyond the experimental uncertainty over the tested range, irrespective of the processing condition. Colors of irradiated, and irradiated and annealed data points in (b-d) correspond to those used in the stress strain curves of Figure 3.1a.

the parent glass and the shear disordering occurring during a localization event would diminish. Thus, plastic flow would manifest more homogeneously, even at testing temperatures below T_g .

3.3. Conclusion

This chapter demonstrates that accurate deconvolution of any true size scale effects with those from irradiation during specimen fabrication requires pristine MG specimens with nanoscale dimensions. For instance, incorporation of Ga into the surface of testing samples would cause local changes to chemistry, which could affect the mechanical response. However, the clear transitions in deformation mechanisms and concomitant mechanical behavior following annealing of our irradiated nanowires back that measured in as-molded specimens following both irradiation and annealing suggests that chemical changes are not sufficient to preclude structural relaxation.

Our findings evoke a second key implication. Namely, these insights provide a potential avenue for the design of ductile and tough amorphous metals. In contrast to crystalline metals, where strength and toughness often are sacrificed for one another, glassy materials maintain high strength even in their ductile states. As shown in Figure 3.3, neither ion irradiation nor annealing changes the strength of the nanowires beyond the uncertainty of our measurements. Moreover, no clear size, surface area, or volume dependence of strength occurs (Figure 3.3). In contrast to previous research that suggests the utilization of nanosize length scales in a MG microstructure as a

design tool to achieve tensile ductility, our findings suggest that such ductility can be achieved through structural modifications towards a more liquid-like structure. The present technique is potentially a powerful approach to generate ductility in nano and micron size MG samples and device features, accessible by a variety of established processing schemes in addition to the one presented herein (e.g. vapor deposition, electrochemical deposition, plastic deformation-mediated thinning). Due to the limited depth penetration of ion implantation, modifying the structure of MGs to more liquid-like in bulk samples would require novel processing techniques such as severe plastic deformation²⁸⁹, shot peening²³⁰, or innovative approaches that would resemble the effects of high cooling rates. Such developments of efficient and economic techniques to achieve tensile ductility in bulk samples may become central to the widespread use of MGs in structural settings.

Chapter 4

Systematic Study of Ion Irradiation

Portions of this chapter have been reproduced with permission from Acta Materialia, Volume 74, Page 165 (Copyright 2014 Elsevier).

In the previous chapter, ion irradiation and annealing were demonstrated as effective methods to tune the tensile response in MG nanostructures. In the following chapter we report an in depth study of the effects of ion irradiation on the structure and mechanical response of Pt-based MG nanowires. By systematically varying the irradiated volume fraction and ion fluence, a transition from originally brittle-like to ductile-like tensile behavior was measured, a direct result of changes to the structural state of the glass. Above a threshold of ion fluence and irradiated volume fraction, the plastic response was characterized as more ductile, deformation became quasi-homogeneous and a reduction in yield stress was measured. The observed increase in ductility and reduction in yield stress are understood by changes in the fictive temperature of the MG caused by ion irradiation. Finally, we present a unified model for the scaling of yield strengths in MGs that is capable of describing the variety of structural states available

4.1. Structural Characterization of Irradiated Nanowires

To verify that the nanowires remained fully amorphous and to attempt observations of changes in structure, irradiated wires are examined via TEM. Figure 4.1 shows diffraction patterns of as-molded nanowires and irradiated nanowires for two different ion fluences. No crystal diffraction spots are observed in the unirradiated or irradiated diffraction patterns, indicating an amorphous structure. However, subtle changes in the second diffuse scattering ring are observed. The integrated intensities and corresponding difference curves (Figure 4.1e, f) show that the wires irradiated at 123 ions/nm^2 and 221 ions/nm^2 undergo a structural change which induces a detectable change in the second ring. Before irradiation the second diffraction ring is relatively broad (Figure 4.1a, c) and shows signs of splitting as evidenced by the integrated intensities (Figure 4.1e,f). After irradiation, peak splitting is no longer detectable in the second diffraction ring. This subtle change may be indicative of changes in the mid-range order and point to a more liquid like structure as corroborated by recent MD simulations showing reductions of icosahedral cluster populations owing to ion irradiation²⁴³; however, systematic quantification proved challenging.

Results from atom probe analysis of nanowires in the as-molded state give a composition of $\text{Pt}_{56.0}\text{Cu}_{16.7}\text{Ni}_{7.3}\text{P}_{20.0}$, which agrees very well with the composition of the starting MG materials, confirming that the molding process does not significantly alter the composition of the resulting nanowires. Analysis from both the irradiated and irradiated plus annealed state indicate that there is a measurable decrease in the

Ga content beneath the surface of the wires after annealing. For the volumes analyzed, the total amount of Ga found 15-30 nm below the surface was 2.0 ± 0.4 at.% before annealing and 0.25 ± 0.05 at.% after annealing. As previously discussed, these values represent upper limits of the Ga concentration (relative to irradiated tensile specimens) owing to the preparation of atom probe tips. The ends of the wires prepared for atom probe had been trimmed with the 30 kV ion beam, thus the ion implantation profile is expected to be close to equilibrium²⁹⁰. However, since the exact equilibrium shape is unknown, we cannot quantify the precise Ga dose or account for variations

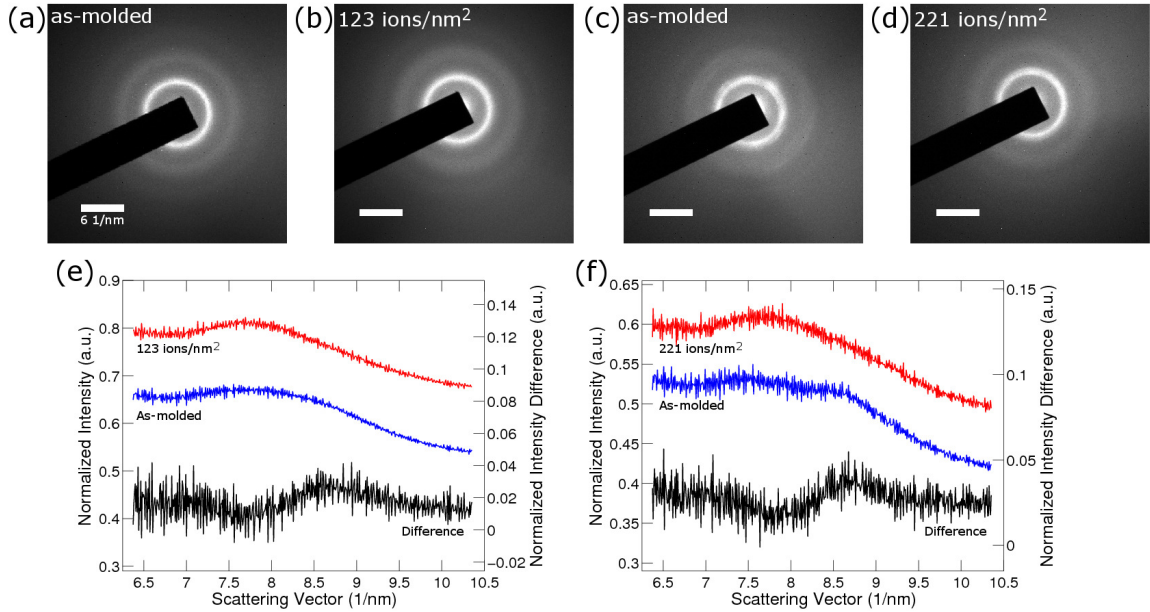


Figure 4.1: Selected area TEM diffraction patterns of nanowires irradiated at different ion fluences. (a) and (c) show diffraction patterns from two individual wires before irradiating. (b) shows a diffraction pattern of the wire in (a) after irradiated at 123 ions/nm^2 , (d) shows a diffraction pattern of the wire in (c) after irradiated at 221 ions/nm^2 . In all patterns, no obvious crystal diffraction spots are observed. (e) and (f) show integrated intensity profiles of the second peak for patterns (a) and (b), and (c) and (d) respectively with the difference between the two patterns shown. The intensities are normalized by the intensity of the first peak and offset for clarity.

in dose from wire to wire due to differences in sample preparation. Therefore, it is not possible to precisely quantify the reduction in Ga concentration for the nanowires used for mechanical testing. Nevertheless, we are able to qualitatively confirm that the Ga concentration in the sub-surface regions is reduced after annealing.

4.2. Tensile Response of Irradiated Nanowires

Whereas any major structural changes are virtually undetectable by the scattering methods used here and the extent of Ga incorporation was shown to be minimal, the amorphous structure was retained following all ion irradiation treatments and clear changes in mechanical response were measured as a function of the different irradiation treatments. Figure 4.2 shows representative stress-strain curves of MG nanowires irradiated at 5 kV and 30 kV for diameters ranging from 100 to 160 nm. We first describe our reference behavior, which is that of the as-molded nanowire, which shows linear elastic loading followed by abrupt failure. This is characteristic of metallic glasses tested in tension at room temperature¹¹. In contrast, the irradiated nanowires show an increasing amount of plastic strain and decrease in the apparent yield stress (as defined as the stress at which the response clearly deviates from linear elasticity) as the ion fluence is increased. These general trends appear to be relatively insensitive to the ion accelerating voltage (and thus the irradiated volume fraction), as shown for the stress strain curves corresponding to 5 kV (Figure 4.2a) and 30 kV (Figure 4.2b). We note that the appearance of inelasticity occurs at relatively low ion

fluence levels ($\sim 30 \text{ ions/nm}^2$) for both accelerating voltages. The nanowires irradiated at 30 kV (and to a lesser extent those irradiated at 5 kV) show significant scatter in the apparent Young's moduli, which we attribute to the compliance of the gripping materials that contributes to the measured strain²⁷⁹. While the DIC techniques used to measure strain yield a noise floor ($\Delta\epsilon$) of $\sim 4 \times 10^{-4}$, the strain is measured from markers placed on the grips. Thus the strain measured is the total strain in the nanowire-EBID grip system. Using the elastic modulus of the bulk allow¹³⁴, we estimate the nanowire stiffness to be within an order of magnitude of the EBID grip stiffness. Therefore, the uncertainty in any modulus measurement is roughly 10 to 20% from the grip compliance alone²⁷⁹. This uncertainty is typically greater than that due to other factors (i.e. force and cross section measurement) and is much higher than the expected change in modulus due to modification of the glass structural state¹⁵¹. Thus, despite the reported correlation between glass structure and elastic modulus that supports our observations of lower modulus with increasing ion damage, the resolution and scatter of our elastic modulus measurements prove inconclusive.

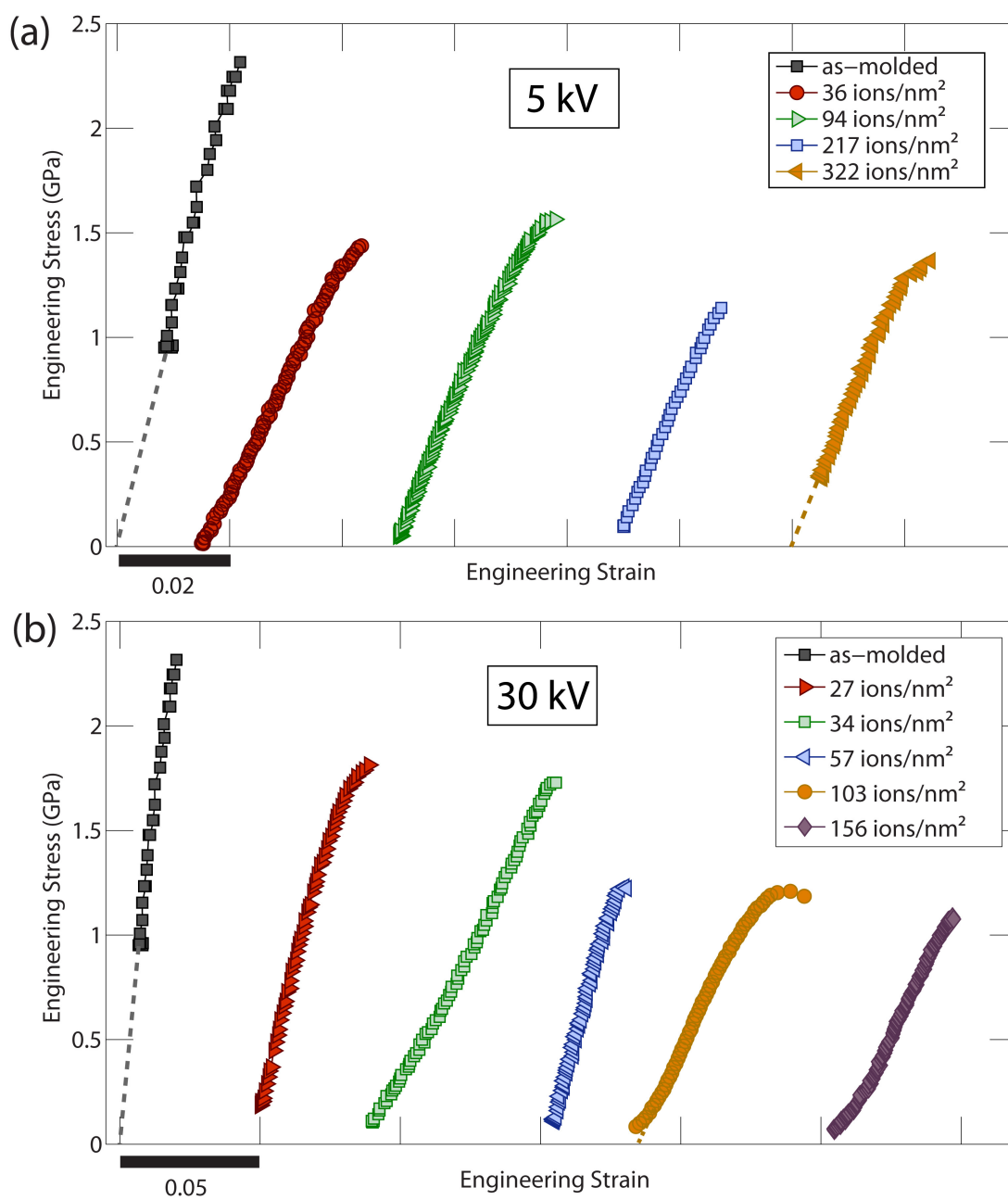


Figure 4.2: Representative stress-strain curves for nanowires irradiated at (a) 5 kV and (b) 30 kV and increasing ion fluences.

4.2.1. Effect of Ion Irradiation on Tensile Ductility and Yield Strength

To systematically demonstrate the effect of ion fluence and irradiated volume fraction on the amount of plastic deformation observed, we compile a deformation mechanisms map showing both the plastic strain normalized by the total strain to failure (color) as well as the failure mode as a function of ion fluence and irradiated volume fraction (Figure 4.3a). In the map, triangles indicate failure characterized by shear banding. The circles indicate wires whose deformation was characterized as ductile (quasi-homogeneous). The diamonds indicate nanowires which failed in a mode which was neither a shear band nor ductile which we describe as “intermediate.” The type of deformation is determined based on the force-time curves and images of the fracture surface that showed a diversity of morphologies as shown in Figure 4.3b-d. Representative and normalized force time curves are shown alongside corresponding fracture morphologies to facilitate comparison between the different deformation modes. The brittle-like mode with signature shear band-mediated failure is characterized by a force-time curve with a constant slope up until failure (black curve in Figure 4.3b) and a sharp angled fracture surface indicative of a shear band. In contrast, the ductile-like mode is indicated by a clear change in slope of the force-time curve (yellow curve in Figure 4.3d) before failure and a fracture surface that shows clear evidence of plastic deformation (e.g. rounding of the fractured edges). The “intermediate” mode is characterized by a less distinct change in slope of the force-time curve (as indicated by the deviation of the red curve in Figure 4.3c from the dashed blue line) and fracture

surfaces that can not clearly be delineated as shear band-mediated or ductile; rather, they show signatures of both behavior simultaneously.

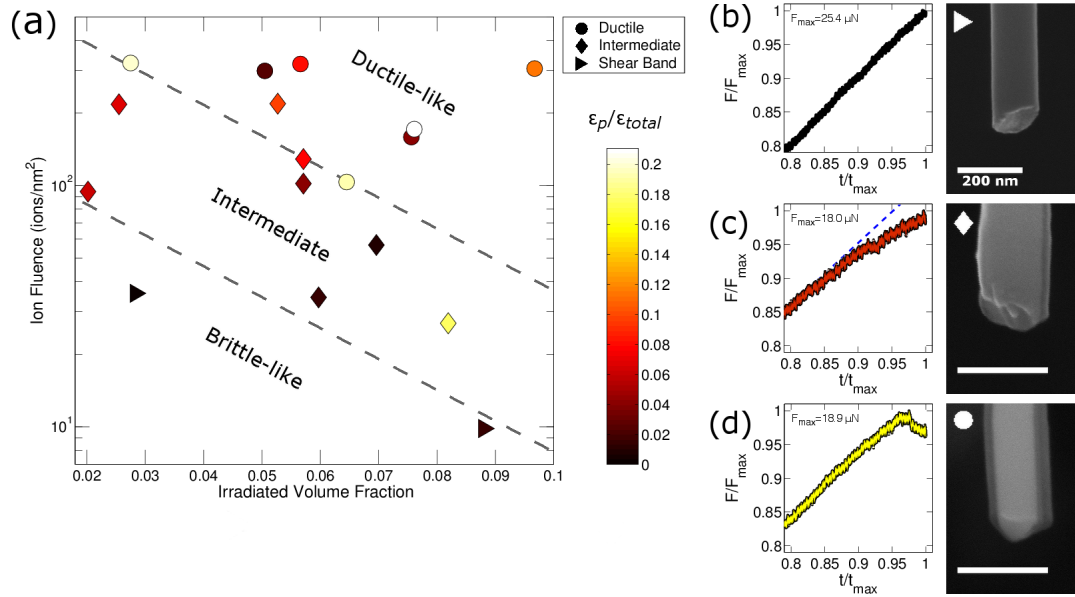


Figure 4.3: (a) Deformation map showing the influence of ion fluence and irradiated volume fraction on amount of plastic strain. The plastic strain is normalized by the total strain to account for differences in grip compliance. The dashed lines are to guide the eye to the transition between deformation regimes. (b-d) show typical force-time curves and fracture morphologies for the shear band, intermediate, and ductile type deformation respectively. The force-time curves are normalized by the maximum force, which is indicated on the plot, and time at failure in order to facilitate comparison of the different deformation modes. The colors of the curves match the color scale of (a) marking the approximate extent of plastic strain.

The deformation map for plastic strain shows two trends. First, there is a clear trend in the mode of deformation (indicated by the data marker symbol type in Figure 4.3). At low ion fluence and irradiated volume fraction, the deformation mode is characterized as shear band-mediated similar to the as-molded case. At high ion fluences and irradiated volume fractions, the deformation mode is characterized as ductile. Between the shear band and ductile regimes an intermediate regime is

observed. In this region, some plastic deformation is detected but the fracture surface is not clearly a shear band or ductile mode. The dashed lines in the Figure 4.3 show the transition between the deformation modes.

The other trend apparent in our data is a general increase in the amount of plastic deformation with increasing ion fluence and irradiated volume fraction. Unlike the transition in deformation mode, the correlation between plastic strain and ion irradiation conditions is not as pronounced. Some nanowires characterized as intermediate showed more plastic deformation than nanowires characterized as ductile. These observations suggest that the extent of ductility in a glass, much like that in crystalline materials, is not a deterministic parameter and instead is governed by the stochastic nature of local inelastic rearrangements (e.g. STZs) and the evolution of plastic damage in disordered materials.

Similar to the amount of measured plastic deformation, the decrease in yield stress shows a trend with ion fluence and irradiated volume fraction, as shown in the yield stress deformation map of Figure 4.4. At low ion fluence and irradiated volume fraction, the yield stress is similar to the previously reported mean yield stress of 1.6 GPa for the as molded Pt-glass nanowires²⁵⁹. As the ion fluence and irradiated volume fraction increase, a decrease in yield stress is observed. To determine the predominant factor, irradiated volume fraction or ion fluence, linked to changes in yield stress, we examined the correlations individually as shown in Figure 4.4b and c. The plot of yield stress versus irradiated volume fraction (Figure 4.4b) shows no clear correlation in the range

of volume fractions sampled. The plot of yield stress versus ion fluence (Figure 4.4c), however, shows a trend towards decreasing yield stress with increasing ion fluence. A linear fit is shown in Figure 4.4c to emphasize the trend towards lower strength. In addition, the linear fit shows good agreement with the as-molded strength. From these analyses, it is clear that ion fluence (thus, extent of displacement damage) plays the dominant role in changing glass structure and concomitant mechanical behavior in our study despite the difference in ion energies (and hence range). The importance of extent of damage is further bolstered by measurements of the tensile behavior of ion-irradiated nanowires subsequently subjected to structural relaxation annealing. Five irradiated wires, subjected to ion fluences between 115 and 145 ions/nm², were administered structural relaxation annealing before measuring the tensile response. The yield strength of the irradiated and annealed samples returned to the yield strength of the as-molded level or even higher as shown by the open symbols in Figure 4.4c.

The insensitivity to irradiated volume fraction over the range studied can be reconciled by considering the distribution of damage created by ions at different accelerating voltages. Despite the different damage distributions, the peak damage occurred within 5 nm of the surface irrespective of ion accelerating voltage (Figure 2.6c). Nevertheless, it is interesting to note that substantial differences in mechanical behavior can be detected even with irradiated volume fractions as small as 2%. Taken as a whole, the yield strength changes measured as a result of ion irradiation (decreasing strength) and subsequent annealing (increasing strength) suggest the ability of our

treatments to strongly modify the glass structure so as to manifest as substantial changes in the plastic behavior of our nanowires. In the sections that follow, we discuss this correlation between glass structure and mechanical strength and propose a universal model capable of predicting the yield strength of a metallic glass across a wide range of structural states.

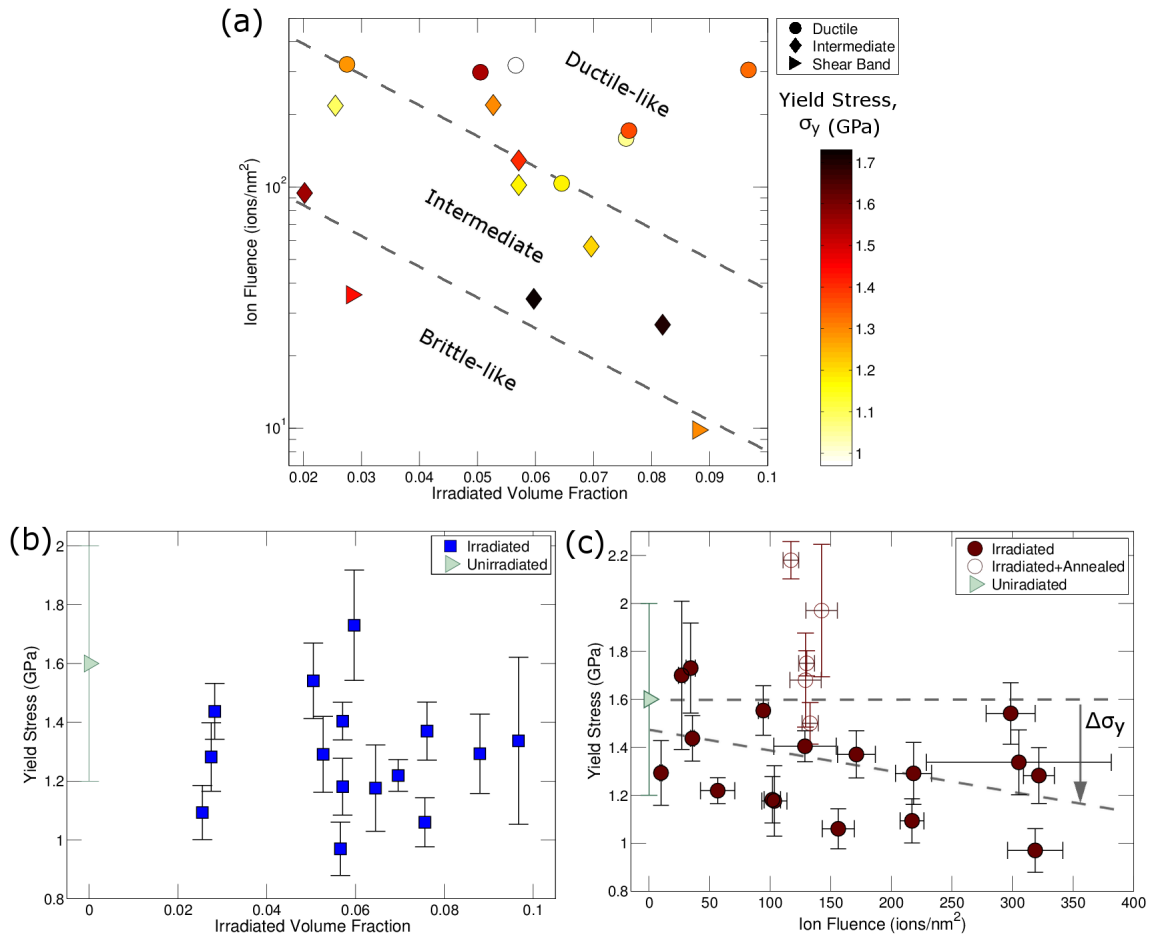


Figure 4.4: (a) Deformation map showing the influence of ion fluence and irradiated volume fraction on yield stress. The dashed lines are to guide the eye to the transition between deformation regimes. (b) Yield stress plotted versus irradiated volume fraction. No clear trend with irradiated volume fraction is observed. (c) Yield stress as a function of ion fluence. The average yield stress of the as-cast nanowires is indicated by the green triangle. Closed circles represent irradiated nanowires while open circles represent irradiated nanowires subjected to a relaxation anneal. Yield stress appears to decrease linearly with increasing ion fluence. The horizontal line indicates the as-molded yield stress and the sloped line is the linear fit used to determine decrease in yield stress. For (b) and (c) the error bars for the unirradiated state are the standard deviation of 10 tensile tests while the error bars for the irradiated and irradiate+annealed states are estimated errors based on experimental uncertainty. Error estimates for ion fluence are also included in (c) based on the measured ion beam current standard deviation of 1 pA.

4.3. Discussion

4.3.1. *Size-Independent Transition in Plastic Deformation Owing to Ion Irradiation*

In order to more clearly highlight the differences in glass structure and the corresponding effect on strength, we also show the measured strength grouped by treatment in Figure 4.5. In Figure 4.5, the average strength of the as-molded, heavily irradiated, and irradiated and subsequently annealed samples are shown as a bar with an error bar corresponding to the standard deviation of the group. Here, the heavily irradiated condition is considered to be top third of the ion fluences used, which corresponds to ion fluences greater than 200 ions/nm^2 . As previously reported, the as-molded nanowires showed a mean yield strength of $1.6 \pm 0.4 \text{ GPa}$ ²⁵⁹. The mean yield strength and standard deviation of the heavily irradiated and irradiated then annealed groups are $1.25 \pm 0.2 \text{ GPa}$ and $1.8 \pm 0.26 \text{ GPa}$ respectively. This strongly indicates that the behavior of the heavily irradiated samples is distinctly different than that of the as-molded and irradiated then annealed samples. We note that the apparent trend in strength as a function of ion fluence contains a stochastic character, which is presumably due to the probabilistic nature of the ion collision cascade process. Indeed, atomistic simulations on ion irradiated metallic glasses²⁴³ suggest a more deterministic relationship between yield strength and potential energy per atom, which is unfortunately not easily measured in our experiments

To explain the observed changes in mechanical behavior of our MG nanowires,

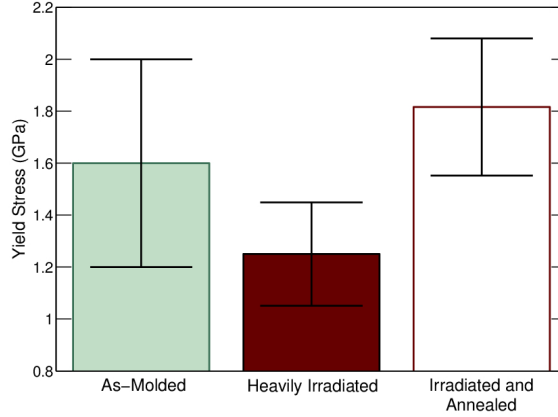


Figure 4.5: Direct comparison of the effect of different Ga ion treatments on the average measured strength. Here, the as-molded strength (1.6 GPa) is directly compared to the highest third of ion fluences employed (1.25 GPa) and the irradiated and subsequently annealed treatments (1.8 GPa). The error bars are the standard deviation of each treatment group. This comparison emphasizes the significant decrease in strength due to ion irradiation and the subsequent recovery due to relaxation annealing.

we consider glass parameters that could contribute to our experimentally measured increases in ductility and decreases in yield stress. Possible factors could include changes in structure, chemistry, free volume, or corresponding elastic constants. However, detecting site-specific structural changes in our nanowires through electron diffraction have proven to be elusive due to limited resolution. Measuring changes in free volume in an irradiated nanowire would be similarly challenging. Free volume is often directly measured through positron annihilation spectroscopy. Yet the high energies and large spot sizes are mainly suited for probing bulk structures and not single nanowires²⁹¹. Other possible metrics for evaluating irradiation induced changes in the glass are the elastic properties. While high Poisson's ratio (or low ν/B) is often associated with more ductile metallic glasses, recent work by Kumar *et al.* has shown the elastic properties to be insensitive to different structural states as

evidenced by measurements of fictive temperature T_f ^{91, 151, 283}. Yet glasses prepared in different structural states show a transition from brittle to extended plastic behavior, casting doubt on the use of Poisson's ratio alone as a predictive metric for ductility. Furthermore, the changes in elastic properties demonstrated by Kumar *et al.* are small compared to the resolution of our nanoscale experiments^{91, 151}. We thus focus our attention on other glass parameters with known sensitivity to glass processing and, correspondingly, structural state, which may explain the dramatic changes in plastic response that we have measured.

4.3.2. Effect of Ga Implantation on the Observed Mechanical Response

From the atom probe results, it is clear that a non negligible amount of Ga is incorporated in the nanowire during irradiation. In the irradiated wire, up to 2 at.% Ga was observed. However, it is important to note that this concentration was measured in the near surface region where the wire was cut using the focused ion beam. As a result this concentration may be taken as an approximate upper limit of Ga incorporation. Yet at all fluence levels, dilute Ga will be incorporated into the nanowires. Therefore, the possible effect of Ga on the mechanical properties is considered here.

Ga incorporation may alter the observed mechanical response through several mechanisms: induced residual stresses, compositional effects, or the formation of a composite structure. Ion implantation leads to structural damage from collision

cascades, but could also induce residual stress, with a gradient resulting from the ion range distribution. Recently the effect of residual stress on the observed mechanical response of MGs was studied via shot-peening²³⁰. While shot peening could result in large compressive residual stresses at the surface, the measured yield stress was not significantly changed relative to unpeened samples. This contrasts with our results showing substantial and recoverable reductions in yield strength, which we thus ascribe to structural changes in the glass.

With regards to chemical shifts from ion implantation, results from literature also suggest that small compositional changes should not significantly affect the properties of the Pt-based glass employed in this study²⁹². Over a range of Pt compositions between 42.5 and 60 at.%, T_g and Vickers hardness showed only small changes of less than 3% and with composition. As a result, the substantial changes in both tensile ductility and yield strength measured in our irradiated nanowires are not commensurate with differences tied to the inclusion of small amounts of Ga and thus minor chemical shifts. The impact of residual stresses and composition is likely further diluted by the relatively small affected volume in the nanowire. In this work, the largest irradiated volume fraction was less than 10%. As a result the majority of the nanowire is unaffected by irradiation, yet the net mechanical response significantly changes.

Finally, it is conceivable that the irradiation process may create a composite structure consisting of a rejuvenated skin and a largely unaffected core. We believe

that both our measured yield strength and the plastic deformation mode is largely controlled by the irradiated volume of the specimen, whereas the measurement of ductility only weakly so. We hypothesize a mechanistic view of this as follows. First, ion irradiation clearly leads to softening of the material. Therefore, the ion-damaged region is likely to commence yielding before the undamaged core thereby controlling the measured yield point. Upon yield, the previously supported load is relaxed in the irradiated region due to plastic deformation and the majority of load bearing must now be borne by the core, which has a smaller cross-sectional area. Thus the stress rises rapidly in the core. Provided this increase in stress exceeds the elastic limit of the as-molded value, this event likely gives rise to yielding of the core that follows in rapid succession. As a result, we believe it is reasonable to assume that our measurements of yield stress are predominately governed by the damaged zone of our irradiated specimens. This picture is supported by simulations of ion irradiation and mechanical properties in MGs²⁴³ where ion collisions near the surface create a damage gradient from the surface to the core. This ion damage was also associated with a reduction in strength in excellent agreement with our results.

In contrast, the quasi-isostrain configuration makes interpretation of ductility in such a composite structure complex. Plastic strain must be accommodated in both the rejuvenated skin and the unaffected core. Therefore, the achievable plastic strain is controlled by both regions. However the undamaged core region is more susceptible to plastic instabilities or fracture, as shown by the brittle failure we observed in

as-molded nanowires, which likely dominate the failure strain. Taken as a whole, we conclude that the measured changes from ion irradiation are primarily due to changes in glassy structural state, as quantified by fictive temperature, and not due to stress or compositional effects.

4.3.3. Effects of Ion Irradiation on Atomic Structure

In contrast with crystalline materials where irradiation damage produces observable defect structures⁹⁷, the atomic effects of irradiation in metallic glasses are generally difficult to experimentally observe. Thus, MD investigations, whose intrinsic timescale closely matches that of ion interactions, have been employed to further the understanding of atomic scale structural effects. Collectively, these MD simulations observed increased volume and distortion of atomic packing configurations, resulting in fewer ideal icosahedral packings, as a result of simulated ion irradiation^{242–248}. Critically, recent work by Baumer and Demkowicz shed light on the mechanisms of irradiation induced structural modification^{246, 247}. Specifically, a damage zone, extending beyond regions of both primary and secondary knock-on events, was observed by considering the local temperature during irradiation. Here, regions that were rapidly heated above T_g as a consequence of ion interactions then quenched to the thermostat temperature were observed and described as “super-quenched zones” with high fictive temperature^{246, 247}. Finally, comparison with uniform liquids subjected to comparable quench rates demonstrated an equivalence between the effects of ion irradiation and

extreme quench rates in terms of density and potential energy^{242, 246, 247}.

4.3.4. Revisiting Kinetic and Thermal Phenomena in Amorphous Materials Below the Glass Transition

We consider kinetic and thermodynamic physical properties of MGs, namely, glass transition and fictive temperatures, respectively, as descriptors of structural state and thus changes in mechanical behavior. We begin our discussion by briefly reviewing the conceptual notions and experimental considerations that underlie the use of glass transition and fictive temperatures to connect to inelastic mechanical behavior. The glass transition is a kinetic phenomenon^{293, 294}. As the liquid is quenched (or the solid is heated), a temperature – the glass transition temperature – is reached where structural relaxation times are on the order of ~ 100 seconds as the material transitions from supercooled liquid to a kinetically frozen glass (or vice versa)^{37, 293}. Measurements of T_g are often performed using calorimetric means, with T_g depending on the cooling or heating rate used to make the measurement. Higher cooling rates result in higher T_g , but orders of magnitude changes in rate produce relatively small changes in T_g ⁸². However, asymmetric cooling and heating (i.e. cooling faster than heating) results in a different measured T_g on heating versus cooling. As a result, to obtain a consistent and reproducible T_g , the glass should be cooled and heated at the same rate and as close to equilibrium as possible while still avoiding crystallization²⁹³. For experimental practicality, within the metallic glass community T_g is typically

reported on heating at approximately 20 K/min.

In addition to the effect of cooling rate, small changes in T_g can be induced through processing treatments such as annealing. For instance, changes in the glass transition due to aging of a MG can be measured^{144, 155, 295}. Aging a MG at temperatures below T_g has been shown to relax the structure, reducing the free energy and free volume. Changes to T_g due to aging are typically less than 10 K even for complete relaxation of the glass, although the amount varies for different glass compositions^{144, 155, 295}. Mechanical treatments such as severe plastic deformation have also been reported to have little effect on T_g despite reports of large changes in hardness, elastic modulus, and calorimetrically measured exothermic peaks prior to the glass transition^{50, 198}.

Whereas T_g is insensitive to cooling rate, annealing, and severe plastic deformation treatment, T_f can be widely varied^{86, 88-90}. In contrast to T_g , the fictive temperature is a thermodynamic variable describing the temperature at which the kinetically frozen structure would be at equilibrium with the liquid⁸⁷, and is qualitatively related to structural descriptors like free volume²⁹⁴. A given fictive temperature does not specify a unique glass structure; rather many possible structures may result in the same observed fictive temperature²⁹⁶. Importantly, T_f can be greater than or less than T_g and varied semi-independently of the T_g . While T_g typically changes <10 K for a fully relaxed glass, the fictive temperature has been observed to change by more than 20 K for shorter relaxation times⁸⁶. Hyperquenching oxide glasses has also resulted in glasses with T_f as high as $1.22T_g$. Yet, T_g has been reported to change

little after relaxing the quenched glass⁸⁹. Finally, the large excess enthalpies observed in glasses subjected to HPT indicates a high fictive temperature yet T_g was observed to be invariant^{50, 198}. These results collectively point to T_f as a much more sensitive predictor of the structural state of a given glass as supported by systematic calorimetric measurements in the literature^{81, 297}, which suggests a correlation between T_f and the concentration of flow defects²⁹⁷. In the discussions and analysis that follow, we assume T_g to be relatively constant for our metallic glass experiments and attribute the observed change in material response owing to ion irradiation and subsequent structural relaxation annealing to changes in structural state as reflected in T_f .

4.3.5. Correlations between T_f and Plastic Deformation, and T_g and Yield Strength

We next examine correlations between the thermodynamic and kinetic properties of a metallic glass with its mechanical behavior. A recent report by Kumar *et al.* showed that increasing T_f in several MGs increased the capacity for plastic deformation in bending⁹¹. Thus, the increase in plastic deformation that we measured could similarly be justified through an increase in T_f due to ion irradiation. Analogously, the increase in tensile ductility could be attributed to an increase in liquid-like states or higher free volume^{298, 299}. In the case of yield strength, the observed changes could be rationalized through changes in T_g as recently proposed. Yang and Liu reported unified predictions of yield stress entirely as a function of a given MG's molar volume and $T_g - T_o$, where

$T_o \ll T_g$ is the testing temperature (the details of this prediction will be presented in greater detail in the following analysis)^{14, 15}. Briefly, a glass with a higher T_g or lower molar volume would be expected to exhibit a higher yield strength (and elastic modulus). Based on this prediction, we can examine the effect that irradiation has on the expected change in yield strength of our MG nanowires. Assuming that irradiation effectively shifts our MG along Yang *et al.*'s universal scaling curve, our measured reductions in yield stress owing to ion irradiation would indicate a decrease in T_g of ~ 40 K (changes in molar volume are estimated to be negligible). Such a reduction of T_g estimated by this yield stress prediction is opposite what one would expect for a more ductile glass. Rather, a reduction of T_g indicates a more relaxed glass state (analogous to a relatively slow cooling rate), which would be expected to be more brittle in comparison to the as-molded condition. This failing of the unified strength scaling to describe our experimental results suggests that the structural state of a given MG system is not described by this relationship. Thus, in order to properly account for the observed changes in ductility and yield stress, we propose the incorporation of a structural state descriptor given by T_f , which can capture the processing dependence of a given MG.

4.3.6. *New Analytical Model for Universal Strength Scaling Dependent on Glass Structural State*

To understand the influence of T_g and T_f on yield strength, we begin by revisiting the universal MG yield strength predictions presented by Yang and Liu^{14, 15}. Both models are predicated on equating the change in internal energy as a glass is taken through the glass transition into the supercooled liquid regime to the work performed to initiate a mature shear band. Mechanistically, this equality is rooted in the similar structural signatures associated with local plastic shearing and the glass transition, wherein dilation and free volume production occur in both cases, as quantified by decreases in viscosity. Two analytical models have been proposed that result in the same scaling with subtly different approaches, with Yang's prediction¹⁴ implicitly assuming a free volume mediated mechanism to formulate their theory. Liu *et al.*¹⁵, on the other hand, developed their model on simple thermodynamics without recourse to an assumed deformation mechanism. Despite these differences, the net results and scaling behavior are equivalent as the latter model recovers the former.

Liu *et al.* assumed the plastic yield process is volume preserving. Thus the work done can be written as $dW = V_s \gamma_0 d\tau$ where V_s is the volume undergoing a transition due to plastic flow, γ_0 is the critical strain for shear instability, and τ is the applied shear stress¹⁵. Furthermore, for a constant volume system, the change in internal energy can be written as $dU = \rho V_s C_v dT$. By assuming that the heat released during yield is much less than the work done by the applied stress (i.e. $dQ \ll dW$),

an expression was derived equating the work done to changes in internal energy (Equation 4.1)¹⁵.

$$V_s \gamma_0 \int_0^{\tau_y} d\tau = V_s \int_{T_o \ll T_g}^{T_g} \rho C_v dT \quad (4.1)$$

The integration bounds represent a transit through the yield point, and equivalently, from room temperature (T_o) through the glass transition.

While Liu assumed the Dulong-Petit limit of heat capacity, Yang adopted the Debye model for heat capacity^{14, 15}. By integrating the Debye heat capacity, the yield stress was related to the glass molar volume and T_g as

$$\sigma_y \approx \frac{6Nk(T_g - T_0)}{\gamma_0 V} \quad (4.2)$$

where N is Avagadro's number, k is Boltzman's constant, γ_0 is the shear disordering strain which is assumed to be of order unity, and V is the molar volume. This scaling of yield strength is equivalent to Liu's prediction¹⁵. Such universal scaling between stress and temperature (and thus viscosity) in a MG and the physics underlying a stress-induced glass transition is also supported by MD simulations of a Zr-based MG³⁰⁰.

However, we observe that this prediction does not account for the state in which the glass is kinetically frozen, which would suggest that a given glass's yield strength and capacity for plastic flow at a given temperature is insensitive to the processing route and thermomechanical history. This is in stark contrast to experimental evidence,

including ours, showing substantial changes in strength and hardness of a given MG system in different structural states^{129, 154, 227, 230}. In fact, if we assume a maximum change in T_g to be ~ 10 K, as measured previously in other glass systems^{144, 155, 295}, we find that the predicted yield stress would change by only ~ 70 MPa, which is inconsistent with our results. Therefore, we propose a revised model, which explicitly accounts for the wide structural spectrum in which a given MG can exist. Glasses are well known to store excess enthalpy, with the magnitude of such enthalpy depending on cooling rate, aging/rejuvenation annealing treatments⁸³, and degree of severe plastic deformation¹⁹⁸. Therefore, by noting that the T_g used as an integration bound is measured via the consistent measurement method (and is therefore constant), we include an additional term representing the excess enthalpy with respect to a known reference state, such as the as-quenched glass, normalized by the molar volume. This excess enthalpy allows glasses prepared into different states to be distinguished; a feature not captured in previous unified strength models. Accordingly, we propose a new yield prediction:

$$\sigma_y \approx \frac{6Nk}{\gamma_0 V} (T_g - T_0) - \frac{\Delta H_{g-g'}}{V} \quad (4.3)$$

where $\Delta H_{g-g'}$ is the excess enthalpy with respect to a glass reference state such as the as-quenched glass (g'). The presence of such excess enthalpy would add to the stored elastic energy during deformation, which is consequently balanced by the internal energy of the system, and thus could be considered as an excess defect energy. In our experiments, the defect energy would be incorporated via ion irradiation-induced

changes in the glass structure and could be reduced through subsequent structural relaxation annealing as we have performed.

To compare with experimentally tractable properties, we relate this additional excess enthalpy term to T_f by considering the measurement and analysis of T_f . From Moynihan *et al.* T_f is determined according to⁸⁸

$$\int_{T'}^{T_{eq}} (C_p - C_{pg}) dT = \int_{T_f}^{T_{eq}} (C_{pl} - C_{pg}) dT \quad (4.4)$$

where C_p is the measured heat capacity, C_{pg} is the equilibrium glass heat capacity extrapolated to high temperatures, C_{pl} is the equilibrium liquid heat capacity extrapolated to low temperatures, T' is any temperature well below the glass transition, and T_{eq} is any temperature well above the glass transition where the heat capacity has reached its equilibrium liquid value. To obtain an expression for T_f , we adapt the method described by Yue *et al.*⁸⁹, where the left side of Equation 4.4 is simply the enthalpy difference between the glass state at T' and liquid state at T_{eq} (ΔH_{l-g}). From Adams and Gibbs, $C_{pl} - C_{pg}$ is assumed to be constant close to the glass transition³⁰¹. Indeed, if we consider the heat capacity difference for the Pt-glass used, $C_{pl} - C_{pg}$ varies by less than 30% over $T_g \pm 50$ K³⁰². Therefore, a simple expression to estimate T_f can be developed by integrating the right hand side of Equation 4.4 and solving for T_f (Equation 4.5). Since ΔH_{l-g} is a measurable quantity, T_f can be estimated from calorimetric measurements.

$$T_f = \frac{-\Delta H_{l-g}}{C_{pl} - C_{pg}} + T_{eq} \quad (4.5)$$

Next, we consider two glasses prepared in different states, denoted a and b . The two glasses will therefore have distinct $\Delta H_{g-g'}$ and ΔH_{l-g} , and consequently a difference in T_f between the two states can be related to the enthalpy difference of the two states as given by Equation 4.6.

$$\Delta T_f = \frac{\Delta H_{a-b}}{C_{pl} - C_{pg}} \quad (4.6)$$

Taking the difference in yield stress between two states provides the energy difference between the two states as (Equation 4.7).

$$\Delta \sigma_y = -\frac{\Delta H_{a-b}}{V} \quad (4.7)$$

Finally Equation 4.6 and Equation 4.7 are combined to relate the yield stress difference to a change in fictive temperature (Equation 4.8).

$$\Delta T_f = \frac{-\Delta \sigma_y V}{(C_{pl} - C_{pg})} \quad (4.8)$$

Here, we have developed this relationship between T_f and yield stress based

on the assumption that T_f changes to a much larger extent than T_g . However, it is important to note that this assumption is not central to the expressions developed, as it is similarly effective to begin with the observation that the unified yield stress models of Yang and Liu incorrectly predict changes in T_g . Indeed, one could simply add the excess enthalpy term to (Equation 4.3) where the T_g term is taken to be a known reference state. In this case, the as-quenched glass state would be the appropriate choice, and subsequently the fictive temperature changes could be introduced again using the as-quenched state as the reference. Finally, by equating the enthalpy differences, we recover Equation 4.8 without considering the relationship between T_g and T_f , but instead simply comparing all yield stresses and T_f to a known reference state.

Using Equation 4.8, the changes in T_f due to glass processing, in our experiments ion irradiation, can be estimated from changes in yield stress. From Figure 4.5, the yield stress decrease is approximately as $\Delta\sigma_y = -350$ MPa based upon the processing groups. The heat capacity difference is estimated to be 30.6 J/mol K at T_g ³⁰² and V is calculated based on a linear rule of mixtures to be $8.76 \text{ cm}^3/\text{mol}$ ¹³⁴. The resulting maximum change in fictive temperature is thus ~ 100 K or $0.2T_g$. Achieving such changes in T_f through cooling rate variation in a typical MG would require rates approximately 7 orders of magnitude higher than for the standard as-cast state³⁰³. Taken as a whole, our experimental measurements of yield strength changes and modeling strongly suggest that ion irradiation dramatically influences the structural

state of our glass by the incorporation of large defect energies (rejuvenation) that can be recovered via structural relaxation annealing treatments. This latter point also implies that any chemical changes to our MG nanowires as a result of ion implantation cannot, to first order, explain the large changes in mechanical behavior and its inherent reversibility.

4.3.7. Application of Yield Strength Prediction to Severely Deformed Metallic Glasses

To test the validity and robustness of our new model, we also apply our analytical formulation and analysis to HPT results from the literature, whereby both changes in hardness and excess enthalpy as a function of cumulative plastic deformation were reported¹⁹⁸. Meng *et al.* performed HPT on a Zr-based glass and measured hardness and elastic modulus via nanoindentation, and correlated such changes to calorimetric measurements of relaxation enthalpy as a function of number of rotations and subsequent relaxation annealing¹⁹⁸. As the number of rotations increased, the hardness decreased from 6.1 GPa for the as-cast glass to 4.9 GPa for 50 rotations; concomitant changes in relaxation enthalpy were approximately 1960 J/mol. Furthermore, HPT induced a change in indent morphology. In the as cast state, clear shear bands were observed around the indent. As the number of rotations increased, a decrease in shear banding was observed. At 50 rotations no shear bands were observed. Additional samples subjected to 50 rotations were annealed at $0.97T_g$ for 1 hour, which recovered

the as cast hardness, elastic modulus, and indent morphology. As a whole, these HPT experiments show remarkable similarity to the ion irradiation experiments presented here in terms of the trends in yield stress, deformation behavior, and reversibility making the HPT results an apt test bed for the yield stress model presented here.

To apply our analytical model we estimated the yield strength as one third the hardness³⁰⁴. We then apply Equation 4.7 to estimate the energy difference between the as-cast and HPT (50 rotations) samples. The yield stress decrease is estimated to be -400 MPa for 50 rotations which indicates an energy change of 4600 J/mol according to our model. From Equation 4.6 and substituting ΔH , we then estimate ΔT_f to be 154 K. Based on the experimentally measured enthalpy relaxation, ΔT_f is estimated to be 65 K and $\Delta\sigma$ is estimated to be -170 MPa. Finally, structural relaxation annealing following HPT treatments recovered the hardness values of the as-cast MG.

Figure 4.6a shows the experimentally measured¹⁹⁸ and calculated changes in yield stress as a function of number of HPT rotations (i.e. cumulative plastic strain) as well as the predicted yield stress from Yang's model¹⁴. The calculated annealed yield stress was determined by assuming complete relaxation (i.e. zero excess enthalpy in the system). In all cases, the approximated and calculated yield stresses are well below the predicted yield stress. Figure 4.6b shows the changes in enthalpy and fictive temperature due to HPT determined using our newly developed analytical model. From these calculations we observe that the values determined from the hardness measurements are roughly three times greater than the values estimated

from the enthalpy relaxation measurements (Figure 4.6b). We attribute this apparent discrepancy to the radially varying plastic strain inherent to the HPT disks; indeed, the center of the disk is less deformed than the edge. Thus, the enthalpy relaxation measurements are probing the average change of the whole sample while the hardness measurements probe only a highly deformed region. However, the nominal shear strain gradient can be estimated as $\gamma = 2\pi Nr/t$ ^{49, 50}, where N is the number of rotations, r is the radial position, and t is the thickness of the disk. The von Mises strain can then be estimated as $\varepsilon = \gamma/\sqrt{3}$ for small shear strains ($\lesssim 0.8$). However, in Meng's work, $\gamma \gg 0.8$ even for one rotation. As a result, an upper and lower limit of

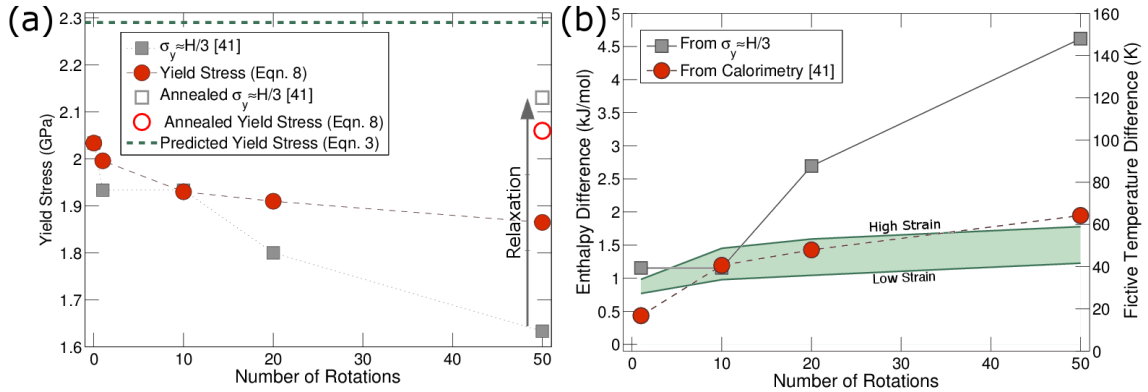


Figure 4.6: HPT results¹⁹⁸ analyzed using the yield stress relationship to fictive temperature. (a) shows changes in the yield stress (approximated as one third of the hardness) determined from mechanical testing and calculated from the enthalpies of relaxation. The calculated yield stresses were determined using Equation. 4.7 using the as-cast glass as a reference state. The results after structural relaxation annealing (indicated by the arrow) are shown as open symbols. (b) The enthalpy difference between the HPT samples and the as cast sample were determined from the approximated yield stress, directly measured by calorimetry, and integrated from the yield stress assuming a linear relationship between von Mises strain, and yield stress. The green band is determined from the high strain and low strain estimates for HPT³⁰⁵; see text for details. Enthalpy differences were calculated from Equation 4.7 and fictive temperature changes were determined from Equation 4.8.

accumulated strain will be considered. Two common strain estimates for materials subject to HPT are $\varepsilon = \left(\frac{2}{\sqrt{3}}\right)\ln\left[(1 + \gamma^2/4)^{1/2} + \gamma/2\right]$ and $\varepsilon = \ln(\gamma)$ which we will consider as an upper and lower estimate of strain respectively³⁰⁵. In light of the reported complexity of the strains incurred by HPT in polycrystalline materials, we note that the absence of microstructure and strain hardening mechanisms in metallic glasses greatly simplifies the picture and thus such modifications to the accumulated strain can be neglected. Thus by fitting the reported yield stress data as a function of number of rotations (and hence strain), the yield stress at each radius can be estimated. By applying Equations 4.7 and 4.6 and integrating over the disk radius, the total enthalpy and yield stress difference can be calculated. Figure 4.6b shows the enthalpy and fictive temperature differences determined from the measured yield stress, calorimetric measurements, and integrated estimate using the high strain and low strain estimates as upper and lower bounds respectively. It is observed that the integrated estimate agrees well with the enthalpy difference as measured via calorimetry, providing additional validation of our model. This analysis thus shows that our revised model connecting plastic yielding in MGs is not only capable of describing strength differences between different glass systems, but can also successfully capture the continuum of structural states within a given glass system brought about by distinct treatments. We expect this approach to be applicable to various processing routes that either structurally relax or rejuvenate glasses.

4.4. Conclusion

Drawing connections between fundamental thermodynamic and physical parameters of glassy materials and their mechanical resistance to plastic deformation is a tantalizing goal. This is a notion that has long eluded predictions of plastic deformation in crystals where structural descriptions of defects and obstacles are more apt. The non-equilibrium nature of MGs and its special property of kinetic frustration at low temperatures, leading to a glass transition, apparently correlates with destabilization by means of mechanical energy. The broad spectrum of structural states in which a glass can exist, a result of its structural heterogeneity and rugged potential energy landscape, is a unique characteristic that allows for a wide range of mechanical behavior. This tunability is appealing from a structural materials perspective in which a given glass chemistry can be designed, for instance, for formability or environmental concerns, and the mechanical behavior could be subsequently varied by relatively low energy processing approaches.

In this chapter, we have shown that Pt-based MG nanowires subjected to ion irradiation and annealing treatments embody these principles and can be taken to extreme structural states, from well relaxed to heavily rejuvenated approaching a liquid-like state. Our systematic experimental study using quantitative *in situ* tensile testing shows the influence of irradiation conditions on inelastic response, which is well captured by a unified analytical model that incorporates the structural state of the glass. Specifically, we draw the several conclusions.

First, Pt-based MG nanowires produced by thermoplastic molding using nanoscale templates exhibit high strengths, brittle-like tensile behavior, and failure mediated by shear banding. Ion irradiation of these nanowires changes the structural state by further disordering the glass, leading to significant tensile ductility, quasi-homogeneous plastic deformation, and measurable reductions in yield strength. Sub- T_g annealing of ion irradiated nanowires elicits structural relaxation and returns the glass state to its as-molded condition and corresponding mechanical behavior. Our systematic study over a range of ion fluences (0-300 ions/nm²) and irradiated volume fraction (0-0.1) suggests that ion fluence and consequent damage shows a stronger correlation with yield strength reductions over the ranges studied.

However, observation of changes in structure or composition show minimal differences. For instance, structural characterization by selected-area TEM diffraction show subtle changes in the integrated intensity profiles, suggesting a more disordered or liquid-like state in ion-irradiated nanowires. Similarly, quantification of Ga inclusion shows only small concentrations on the order of 2%. Despite the small differences in scattering signatures and composition the yield strength reductions are as large as 0.5 GPa.

Finally, previously reported universal scaling laws linking the yield strength of a given MG and T_g can not adequately describe the changes in yield strength as a result of ion irradiation and annealing. In contrast, our newly developed analytical model incorporating the structural state enables predictive capability and captures

our results well. We estimate that ion irradiation at high fluence levels (~ 300 ions/nm²) lead to changes in T_f of over 70 K, which corresponds to approximately 7 orders of magnitude in cooling rate in bulk MGs. We demonstrate the robustness of our model by applying it to literature reports of hardness reductions from several plastic deformation of MGs, and show that the changes in mechanical properties can be used to adequately predict the excess enthalpies of the glass subjected to varying plastic strain.

Our results not only show that the mechanical properties and plastic deformation mode of small-scale MGs can be varied substantially within a given glass system, but also demonstrate the diversity of processing routes that can be used to tailor the structural properties of MGs. Our results and analysis could potentially be used to design new processing treatments that lead to a broader library of properties and more graceful failure modes in glassy materials.

Chapter 5

Thermoplastic Deformation of Individual Nanowires

Portions of this chapter have been reproduced with permission from Scientific Reports, Volume 6, Page 19530 (Copyright 2016 Nature Publishing Group).

Tensile tests on MG nanostructures at temperatures far below T_g reveal a greater sensitivity to processing owing to reduced dimensions. Such sensitivity necessitates an understanding of the role different fabrication routes play. In particular, all specimens studied thus far have been produced by thermoplastic molding. While bulk MG flow behavior has been extensively investigated, comparatively little is understood about elevated temperature deformation at small length scales despite strong interest in employing thermoplastic deformation at the nanoscale. In order to advance the understanding of high temperature deformation of MGs at the nanoscale we performed novel thermomechanical tensile experiments on individual molded Pt-based MG nanowires at temperatures near T_g and examined the flow behavior and failure morphology across a range of viscosities. We further compared these results to thermomechanical compression experiments on bulk specimens of the same composition. Our experiments provide quantitative thermomechanical properties based on individual nanowire experiments, which provide crucial insight for further developments in nanoscale thermoplastic processing.

5.1. High Temperature Creep Measurement

To measure the thermomechanical properties of individual nanowires in creep-like conditions, stress and strain must be applied and measured, respectively, under a variety of temperatures. Here, the temperature is increased by passing an electrical current through the nanowire during mechanical testing, giving rise to Joule heating in the nanowire.

Figure 5.1a shows a representative data set from a thermomechanical experiment, which consists of axial strain and load as a function of time while the power dissipation is increased in a stepwise fashion. The strain vs. time response under Joule heating conditions shows strains that far exceed the room temperature elastic strain limit, indicating homogeneous deformation at elevated temperature in the nanowire. The initial strain of 3% (measured with respect to the initial state of the nanowire) represents the onset of near steady-state conditions where measurements were extracted; strains leading up to this point (not shown) were associated with settling of the power and load feedback circuits. Apparent transients are likely a convolution of both material effects and the experimental feedback control used to maintain constant force and power. Notably, the high strain to failure (>20%) indicates that Joule heating enabled superplastic-like deformation behavior in the amorphous state, which is indicative of high temperatures close to T_g . The extent of deformation is further demonstrated in Figure 5.1b, which shows the first micrograph and final micrograph before mechanical failure from the testing sequence. The white dashed lines illustrate

the initial nanowire length. Notably, the observed steady-state strain rate depends on the dissipated power (related to temperature); as the dissipated power increased the strain rate correspondingly increased. During this experiment, the force data showed little deviation from the set point of $10\ \mu\text{N}$, demonstrating that the electrical current negligibly affected the applied force

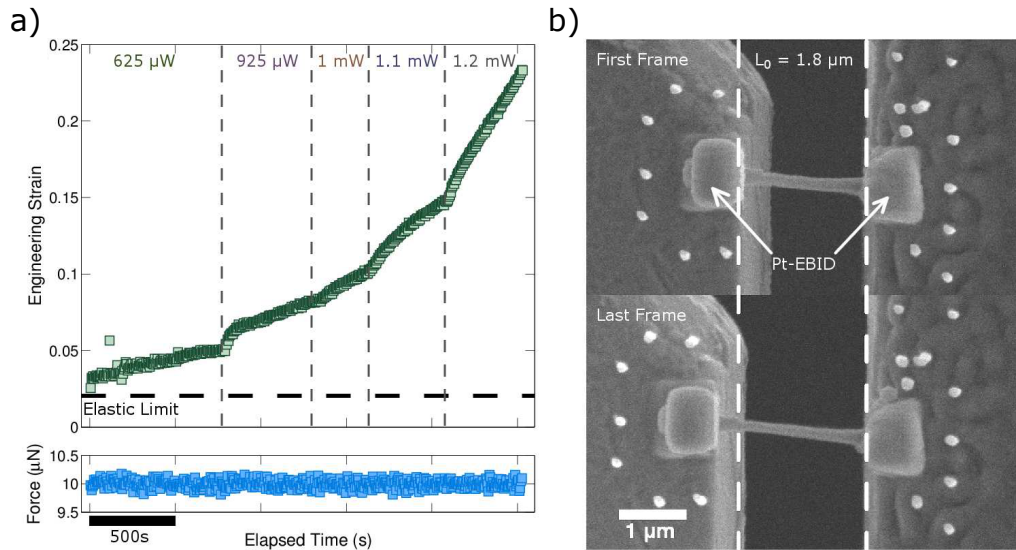


Figure 5.1: An example raw data set is shown in (a), which includes strain measured from the image sequence and force over time. Regions of different power dissipation are also indicated. To emphasize the large strains achieved through thermoplastic deformation the first and final frame of the testing sequence are shown in (b) with the original length indicated by the dashed lines.

From the strain-time data, segments of steady state plastic deformation were isolated. The true strain was determined from the measured engineering strain quantities based on the assumption of uniform deformation and constant volume during plastic deformation. Figure 5.2a shows the steady-state segments of true strain as a function of relative time extracted from the data shown in Figure 5.1a. From these segments the steady-state strain rates were determined as a function of power,

as indicated below each segment. When determining the strain rate the average error was estimated to be less than 1%. To gain additional insight on the thermomechanical response, we performed additional load jump tests on individual nanowires. A portion of a load jump data set from a different nanowire specimen is shown in Figure 5.2b. In this data segment, a constant power of 1.1 mW was applied to a single nanowire. Upon stabilization of power dissipation the force was increased quasi-instantaneously in $2 \mu\text{N}$ steps from $2\text{-}8 \mu\text{N}$. After increasing the force a brief transient was observed followed by extended steady-state deformation. For all data sets the true stress was calculated from the area reduction given by the true-strain. The uncertainty in stress was estimated to be 11% primarily from errors associated with determination of the cross-sectional area. Using the true stress (σ) and true strain rate ($\dot{\epsilon}$), the viscosity was determined according to $\eta = \sigma/3\dot{\epsilon}^{93}$. The resulting error in viscosity was estimated to be 11% across all tests.

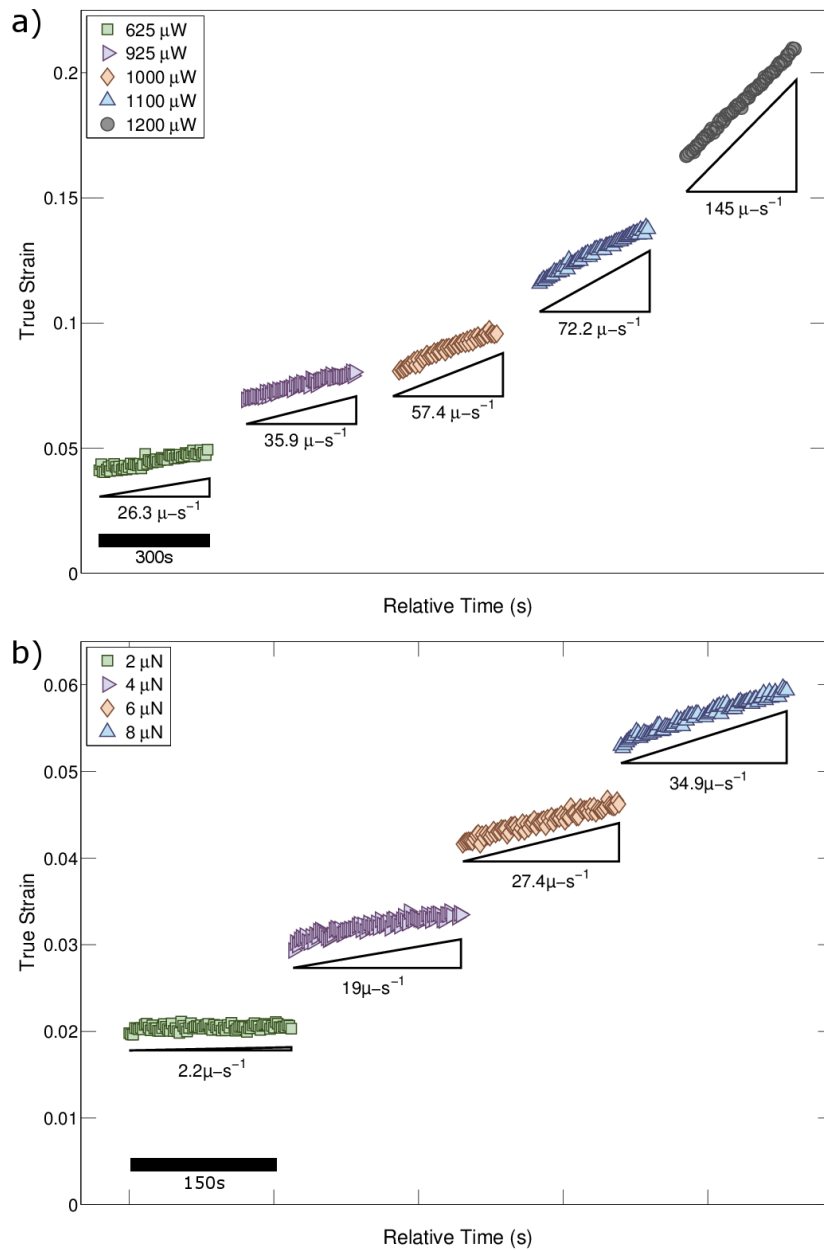


Figure 5.2: The strain data is converted to true-strain and representative regions of constant strain rate and power dissipation are isolated as shown in (a). Here, each segment is a period of steady state plastic deformation under an applied load of $10 \mu\text{N}$. The strain rate of each segment is indicated below the data. Potential stress dependent flow was examined by load-jump tests. An representative portion of strain data from a load jump test on a different nanowire specimen is shown in (b). In this example data 1.1 mW were dissipated in the nanowire and the force was increased in $2 \mu\text{N}$ increments from $2 \mu\text{N}$ to $8 \mu\text{N}$.

5.1.1. Viscosity Scaling with Power Dissipation

The viscosities determined from nine thermomechanical tests (each symbol type is a distinct nanowire) are shown in Figure 5.3 as a function of power dissipated times length squared ($\mu W\text{-}\mu\text{m}^2$), which normalizes to $T - T_{heat}$ sink from the solution to the heat equation for steady state heat generation and conduction³⁰⁶. The inset shows the measured viscosity as log-viscosity versus power dissipated times length squared. From Figure 5.3 it is observed that the measured viscosity varied from $2 \times 10^{14} - 8 \times 10^{11}$ Pa-s, which further indicates temperatures approaching T_g . Additionally, the shape of the viscosity-normalized power relation appears to be exponential. In glassy solids many relaxation processes vary exponentially with temperature, as often described by the Vogel-Fulcher-Tammann (VFT) relationship³⁸. The VFT relation, which was derived from a reaction rate theory, describes the viscosity dependence on temperature by the fragility parameter. A low fragility, or strong glass, indicates a near-Arrhenius-like relationship between viscosity and temperature, whereas a high fragility (weak glass) indicates a strong deviation from Arrhenius dependence of viscosity on temperature. Thus the apparent exponential dependence of viscosity on normalized power indicates that the nanowire temperature is dependent on power dissipation, consistent with Joule heating. However, while the VFT parameters for the Pt-based glass studied here can be estimated, the large scatter in the viscosity data precludes an accurate fit and a true conversion of dissipated power to nanowire temperature³⁰².

It is important to consider sources of scatter in the power dissipated. In partic-

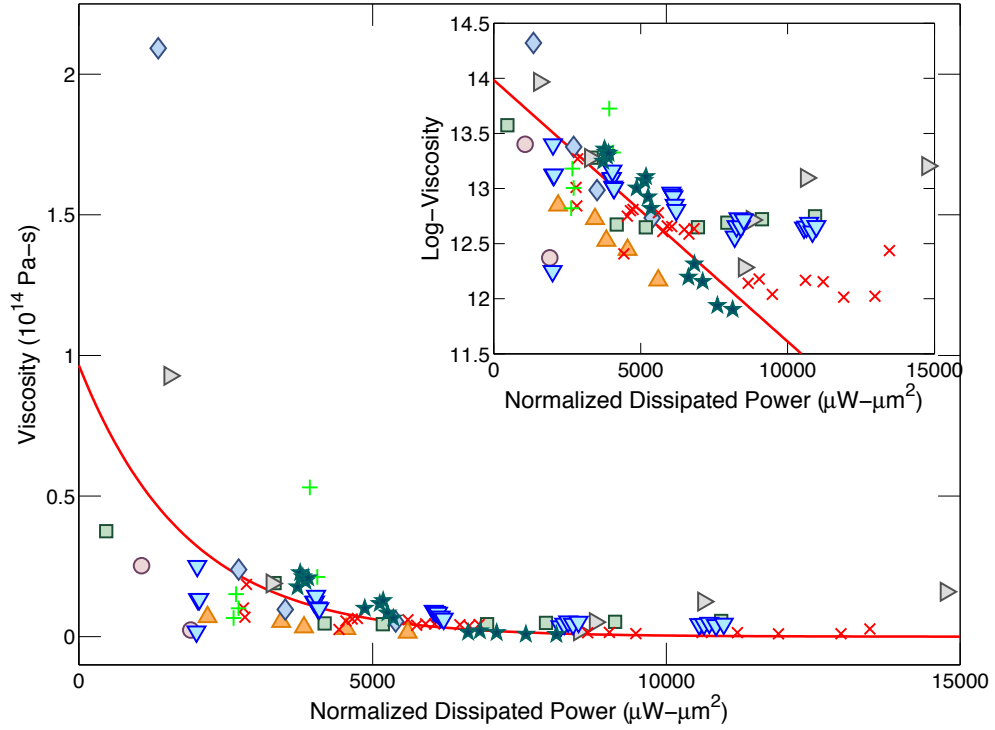


Figure 5.3: Using the measured strain rates and stress the viscosity of the all thermo-plastically deforming nanowires was determined. When plotted against power-length², the normalization for ΔT derived from the heat equation for conduction in one dimension, the viscosity shows an apparent exponential dependence. Here, each symbol type represents a unique nanowire experiment. The inset shows the viscosity data as log-viscosity vs. power-length² to further show the apparent exponential relationship between viscosity and power-length².

ular, the Pt-based electron beam induced deposition (EBID) material used as both mechanical grips and electrical contacts likely produces a large amount of scatter. Generally, the electrical properties of EBID are variable with a strong dependence on the deposition conditions⁶. However, even at consistent deposition conditions larger scatter in resistivity is often observed^{307–309}. Thus, the large variability in the power dissipation and the corresponding material response is likely influenced by the EBID electrical contacts.

5.1.2. Preservation of Amorphous Structure

When assessing the flow behavior of a metallic glass it is critical to ensure that the response is not influenced by nucleation and growth of crystalline domains. Notably, transmission electron microscopy (TEM) observations of failure surfaces confirmed that the nanowires remained amorphous following thermomechanical testing. Electron diffraction (Figure 5.4a) showed several diffuse scattering rings and no crystal spots, which is indicative of a disordered structure. Furthermore, TEM imaging revealed no observable crystallites within the deformed nanowires (Figure 5.4b-c). Indeed, from time-temperature-transition studies of this Pt-based glass, crystallization is not expected under these experimental conditions until very long times greater than 10 hours as estimated from Legg *et al.*³⁰² The calculated crystallization times are shown in Figure 5.4d as a function of the reduced temperature T/T_g . This calculation, in concert with the post-mortem TEM observations, provides significant confidence that crystallization is not an important factor when determining the flow response.

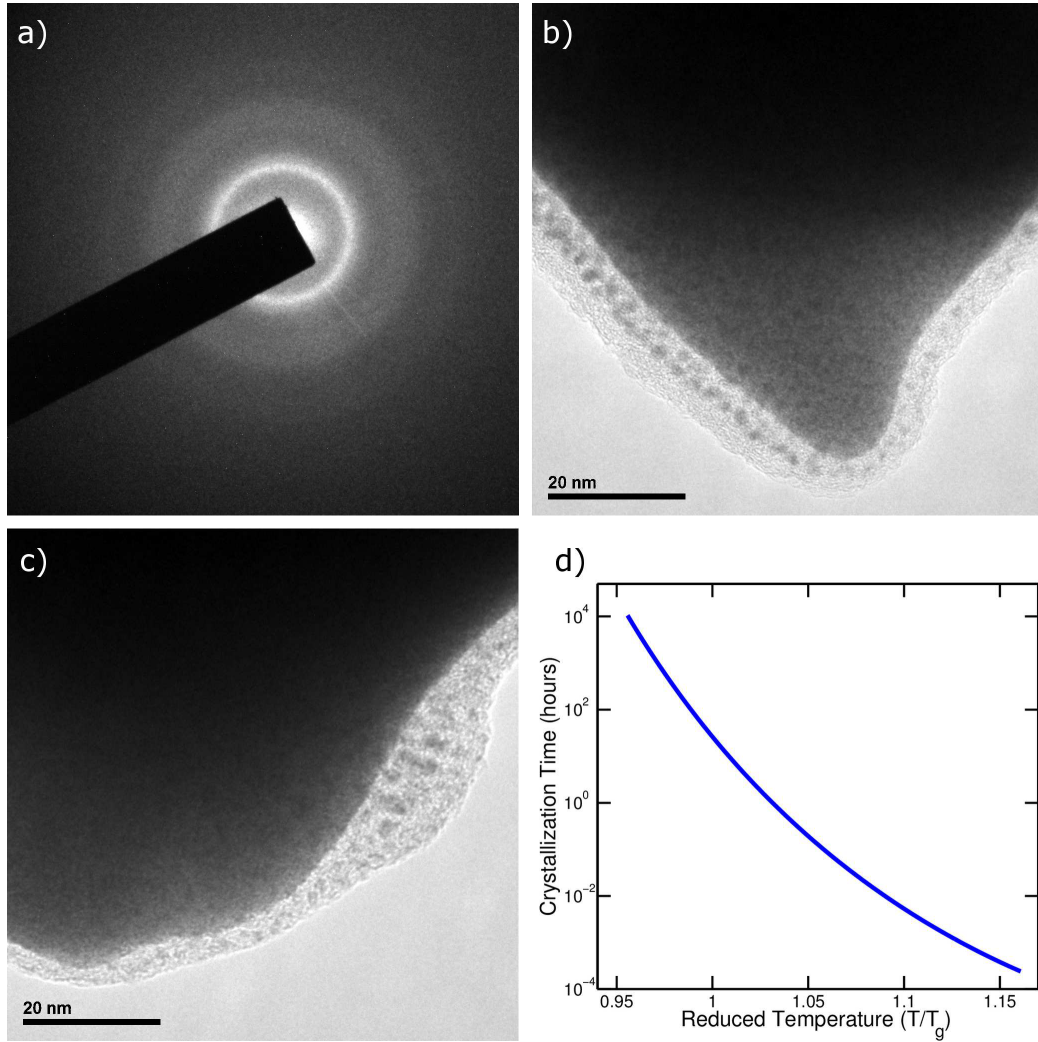


Figure 5.4: Post mortem TEM imaging provides evidence that the nanowires remain fully amorphous. a) SAED patterns taken on from a melted nanowire show no signs of crystal diffraction spots. Bright field images in b) and c) show uniform contrast and no lattice fringes within the nanowire failure surface. In d) the estimated time until the onset of crystallization as a function of temperature is calculated using parameters from³⁰².

5.2. Transition in Flow Behavior

5.2.1. Determination of Flow Regime

Performing tests over a wide range of applied stresses and powers enabled us to examine the full collection of thermomechanical testing results in terms of the steady-state strain rate dependence on stress, as shown in Figure 5.5a, where the symbol color indicates the estimated viscosity. Here, the outlined data points show the highest and lowest approximate iso-viscosity lines, which can be compared to the constitutive law for Newtonian flow given above. A deviation from a strain rate sensitivity of $m = 1$ would indicate non-Newtonian flow. The dashed lines are polynomial fits to the iso-viscosity points to guide the eye. From Figure 5.5a it was observed that the stress varies sub-linearly with measured strain rate, indicating a transition to non-Newtonian flow above a certain stress level.

Load jump tests provide additional insight into the transition from Newtonian to non-Newtonian behavior. Figure 5.5b shows the log-strain rate vs. log-stress for a representative load jump test on a single nanowire, where each symbol type represents a steady-state condition at a different power dissipation. Additionally, each segment is labeled with the mean viscosity of the segment, which decreases as the dissipated power is increased. At each steady state condition, a polynomial function was fitted to $\log \sigma$ vs. $\log \dot{\epsilon}$ to determine the strain rate sensitivity as a function of the experimentally measured strain rate. To identify the transition from Newtonian to non-Newtonian

flow, a threshold strain rate sensitivity was selected. Strain rate sensitivities greater than $m = 0.7$ were identified as Newtonian while strain rate sensitivities less than $m = 0.7$ were labeled as non-Newtonian. In Fig. 4b, the polynomial fits are colored according to this threshold, with red indicating Newtonian ($m > 0.7$) and black indicating non-Newtonian ($m < 0.7$).

Changes in deformation morphology can be used as an additional signature of the transition to non-Newtonian deformation¹¹⁹, which we examine here to corroborate our thermomechanical measurements. While all samples demonstrated plastic deformation in excess of the elastic limit, the failure morphologies varied greatly as shown in Figure 5.5c,d. Figure 5.5 4c shows failure by a drawing down to a sharp point and an absence of system spanning shear character. While such pronounced failure was only observed in one sample, similar morphologies were observed in many samples and signify Newtonian flow. Figure 5.5d presents a typical shear-dominated failure morphology, which is often associated with non-Newtonian deformation at elevated temperatures¹¹⁹.

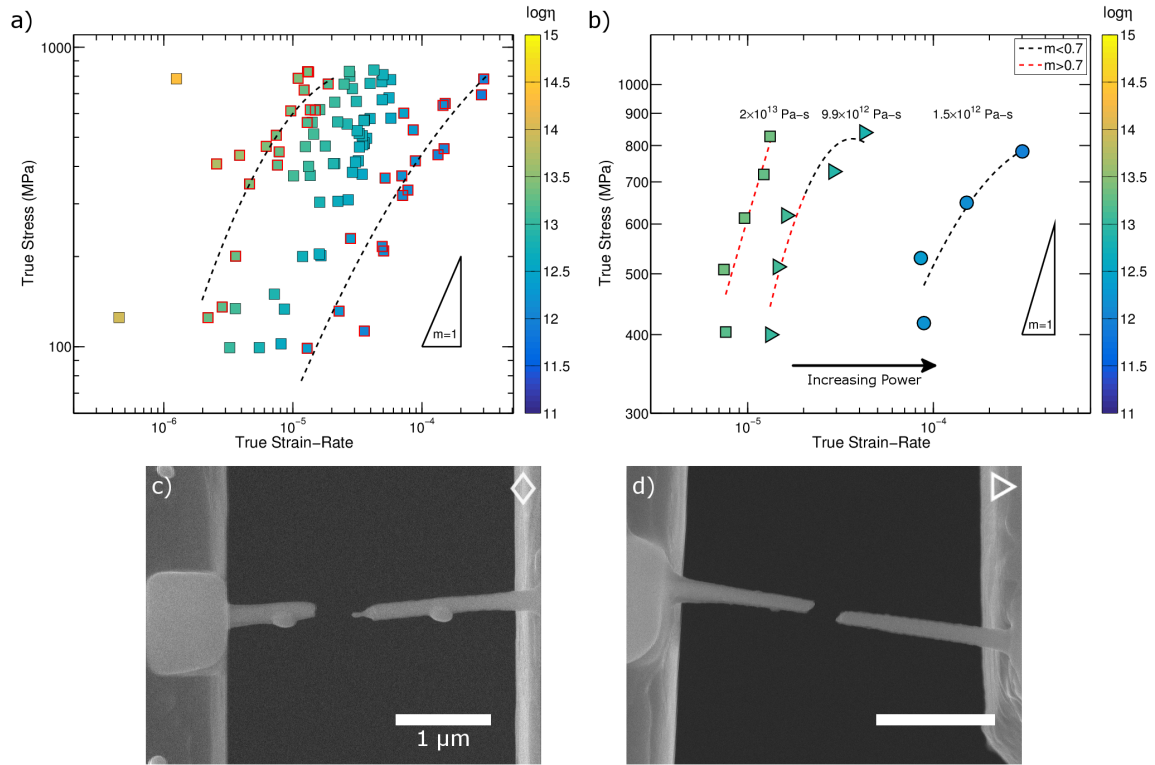


Figure 5.5: To account for potential stress effects on viscosity, the results are plotted as strain rate versus stress in (a). The color scale indicates the log of viscosity. Here, the results from all samples are plotted together. To highlight possible non-Newtonian behavior the highest and lowest iso-viscosity points are highlighted. The dashed lines represent a polynomial fit to these points to guide the eye. A slope of 1, which indicates Newtonian behavior, is provided as a reference. To clarify the behavior observed in (a) we consider only samples subjected to load jump tests. A representative results from a load jump test on a single nanowire is provided in (b), as a function of increasing power (each symbol type indicates steady state at different power dissipation). Each segment is further labeled with its average viscosity. In addition, simple fits are shown to help approximate the strain rate sensitivity, m . The slope of the simple fit is used as an approximated strain rate sensitivity. The fits are colored according to the threshold used to determine the transition from Newtonian ($m > 0.7$) to non-Newtonian flow ($m < 0.7$). Micrographs showing the representative failure morphologies due to (c) necking down to a sharp point, denoted as a diamond, and (d) shear dominated failure, denoted as a triangle, are included. Such morphologies are indicative of Newtonian and non-Newtonian deformation respectively

5.2.2. Size Dependent Flow Transition

To characterize the complete spectrum of thermoplastic deformation in the MG nanowires a deformation map is constructed (Figure 5.6a). The map is constructed from the observed failure morphologies (slashed symbols) and estimated strain rate sensitivities from load jump tests. Here, the symbol types correspond to the symbols from Figure 5.5c,d. Failure morphologies showing no shear character or segments with high strain rate sensitivities are described as Newtonian (diamonds). Failure morphologies showing significant shear character or segments with low strain rate sensitivities are described as non-Newtonian (triangles). In cases when SEM observations were insufficient to definitively assign a failure category, TEM tilt series were used to corroborate SEM characterization. Regardless of the deformation type, extensive plastic deformation was observed before failure in all deformation regimes. From the deformation map a transition from Newtonian to non-Newtonian deformation is observed as the strain rate is increased for a given viscosity. As the viscosity decreases, the transition shifts to higher strain rates.

For a comparison of length scales over four orders of magnitude, included in Figure 5.6a are results from compression of millimeter sized bulk specimens made from the same MG composition. For comparison, bulk specimens of the same composition were compressed at elevated temperatures. Bulk ingots were cut into compression samples with diameter of 2 mm and height of 4 mm (aspect ratio 2:1). The samples were carefully polished to ensure parallelism. Uniaxial compression was subsequently

conducted at temperatures between 240 °C and 255 °C under strain rates between $1 \times 10^{-3} \text{ s}^{-1}$ and 1 s^{-1} . Bulk experiments were conducted at higher temperatures to ensure good temperature control and avoid uncertainties with determination of temperature, resulting in lower viscosities. Consistent with the observation from nanowires, a transition from Newtonian to non-Newtonian deformation was observed. As the viscosity decreased the strain rate required to undergo the transition increased.

To provide context to our results, flow data for nine bulk MGs obtained from literature was compiled in Figure 5.6b^{118, 120–127}. The deformation mode is again determined from the strain rate sensitivity as previously described for the nanowire and bulk compression experiments presented here. Figure 5.6b shows that our measurements on the bulk Pt-based glass are largely consistent with other reports from the literature. Furthermore, the compiled data indicates the Newtonian to non-Newtonian transition to be consistent across the different glass compositions and over 8 orders of magnitude in viscosity. To highlight the transition, a dashed line is included in Figure 5.6b. Critically, the transition from Newtonian to non-Newtonian deformation in bulk specimens occurs at similar strain rates and viscosities regardless of glass composition. Thus, we use the cumulative data set (including the Pt-based alloy used for nanowire measurements) for a large number of bulk metallic glass compositions to construct a linear fit to demarcate the transition between Newtonian and non-Newtonian flow and is also include in Figure 5.6a for direct comparison to the measured transitions in our Pt-based nanowires.

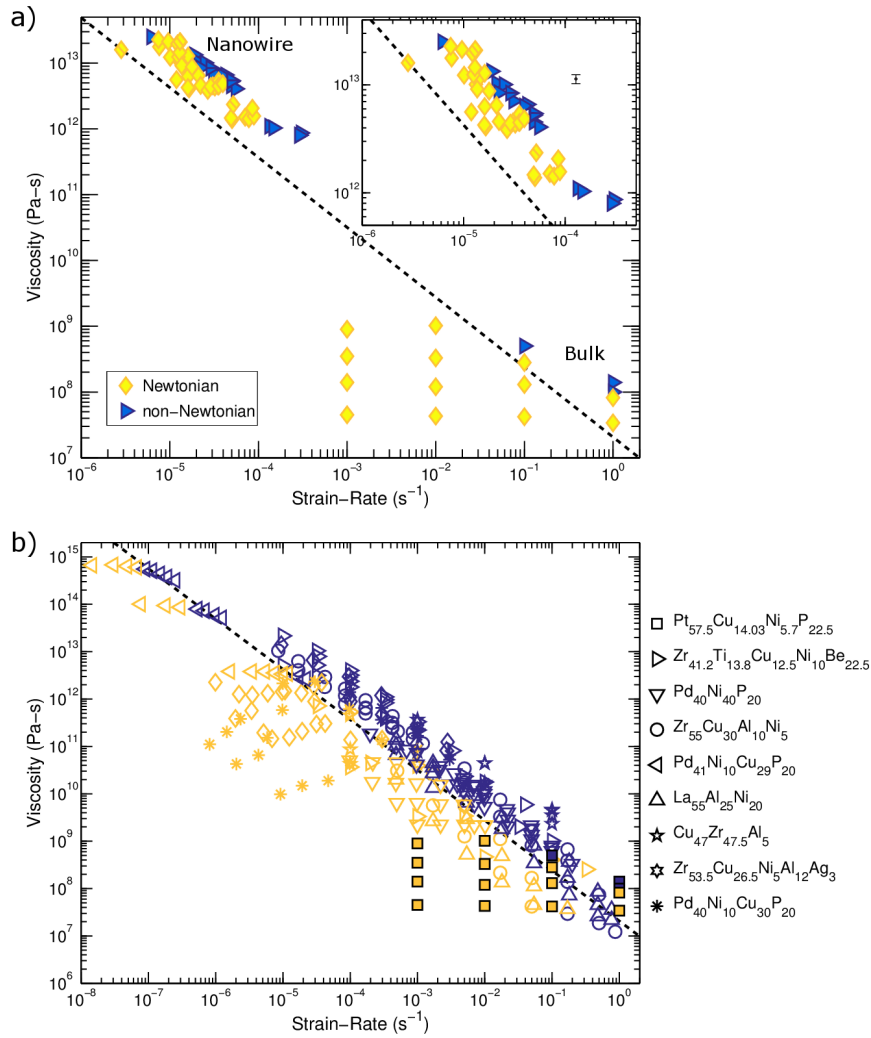


Figure 5.6: (a) A deformation map is constructed from observed failure morphologies (slashed symbols) from all tests and estimated strain rate sensitivities determined from load jump tests on nanowires and bulk specimens. The inset highlights the nanowire results. From the deformation map a transition from Newtonian (yellow diamonds) to non-Newtonian deformation (blue triangles) is observed as the strain rate increases. The symbol types match the deformation morphologies from Figure 5.5c,d respectively. The black data marker in the inset represents the mean uncertainty in the determination of viscosity. The uncertainty in strain rate is smaller than the marker size. A black dashed line, determined from (b), is included to highlight the transition at different viscosities for compiled bulk data. Compiled bulk data from this work (filled squares) and the literature^{118, 120–127} in (b) shows a deformation map over a range of viscosities and strain rates. From the compiled data, an average transition from Newtonian to non-Newtonian deformation is determined as shown by the dashed black line.

5.3. Discussion

Using our results, we can examine the nature of thermoplastic flow in nanoscale specimens as compared to bulk specimens. Phenomenologically, nanoscale and bulk specimens behave similarly. Across all length scales a transition from Newtonian to non-Newtonian deformation is observed as the strain rate increases. Failure morphologies also show similarity; when deforming nanowires in the Newtonian regime the failure surfaces show extensive deformation down to small diameters (Figure 5.5c). In the non-Newtonian regime failure surfaces show shear character (Figure 5.5d). These nanowire deformation morphologies agree with bulk observations¹¹⁹. The hot-pulling experiments further support this qualitative similarity between bulk and nanoscale response, as the estimated transition strain rates are similar in magnitude to those of the bulk material and the deformation morphologies are consistent.

However, a direct comparison between nanoscale and bulk flow behavior indicates a measurable change in the onset strain rate of non-Newtonian deformation at the nanoscale. In Figure 5.6a, the average bulk transition, which does not depend on glass composition, determined from nine bulk MGs shown in Figure 5.6b is reproduced as a black dashed line. When compared with the bulk transition, all nanowire observations, both Newtonian and non-Newtonian, are at higher strain rates than the bulk flow transition. At a given viscosity, the transition strain rate at the nanoscale increases nearly four-fold signifying a significant difference in the flow behavior in our nanowires. This increase is well above the estimated uncertainty in strain rate of $<1\%$. Similarly,

at a given strain rate the flow transition in nanoscale specimens occurs at viscosities nearly four times higher than in bulk. Again, the observed difference in the viscosity at which the Newtonian to non-Newtonian flow occurs in bulk versus nanoscale specimens is much greater than the estimated uncertainty in viscosity of 11%.

To explain the distinct behavior observed at the nanoscale we consider possible differences between nanowire and bulk specimens. Conceptually, the onset of non-Newtonian flow occurs when shear induced free volume generation surpasses thermal relaxation of free volume, resulting in a higher overall free volume and lower viscosities^{69, 99}. As the viscosity decreases the relaxation rate increases resulting in a new steady state at higher free volumes. From Figure 5.6a it is observed that the nanowire specimens examined here maintain Newtonian flow at strain rates up to four times greater than bulk MGs at a given viscosity. This suggests that the nanowire specimens may accommodate greater free volume generation before softening and establishing a new steady state. However, identifying the mechanism leading to the enhanced accommodation of free volume based on fitting bulk formalisms without an explicit temperature measurement is challenging. Instead we consider potential phenomenological explanations for the unique behavior observed at the nanoscale.

The flow behavior of the MG nanowires could be altered by both intrinsic and extrinsic factors. For instance the nanoscale dimensions of the specimen could result in an intrinsic alteration to the relaxation response due to the free surface. To accommodate increased free volume production during deformation the surface would

need to act as a sink of free volume. In such a scenario, newly generated free volume would diffuse to and annihilate at the nanowire surface. This viewpoint is supported by molecular dynamics studies that specifically probe how free surfaces alter glass properties³¹⁰⁻³¹². In all cases, the surface was observed to have enhanced free volume or atomic mobility as compared to the material core. Enhanced surface mobility has been demonstrated to lead to enhanced relaxation and increased ordering at simulated metallic glasses surfaces³¹³. As a result, at reduced length scales the free surface may act as an effective sink of free volume. However, the extent of the surface is limited to the first several atomic layers potentially limiting the effectiveness of the surface at the sizes studied here.

Additionally, the fabrication methods, an extrinsic factor, could alter the free volume distribution relative to bulk structures and enable more free volume to be accommodated. Importantly, in the viscosity range examined relaxation times are still relatively long and the quenched-in free volume likely still influences the nature of deformation. During the molding process the nanowires are held at elevated temperature for an extended period of time resulting in structural relaxation and reduction of free volume. Such a mechanism is supported by Zhang et al. who demonstrated that free volume in nanowires is preparation dependent³¹². Wires produced by simulated hot imprinting showed lower free volume than the bulk as indicated by lower average Voronoi volumes. The reduction in free volume then manifested as distinctly different mechanical responses in agreement with experiments

on MG nanowires, which illustrate a strong post-processing effects^{259, 260, 314}. Thus, the thermoplastic modeling technique employed to produce the nanowires studied likely resulted in a lower initial free volume thereby enabling greater accommodation of free volume generated by plastic deformation.

Regardless of the mechanism resulting in the measured deviation from bulk behavior these results could be useful guides for future thermoplastic forming operations. The hot-pulling results demonstrate the scalability of thermoplastic forming and drawing. The sensitivity of the resulting structures to the strain rate emphasizes the need for in depth studies of high temperature deformation at the nanoscale. Previous studies demonstrated deviations from bulk behavior, such as increasing viscosity at reduced length scales³¹⁵ or nanoscale effects on crystallization³¹⁶. Here, we present the first instrumented study of high temperature flow in amorphous metallic nanowires. We observe that fundamentally the deformation mechanisms (i.e. the transition from Newtonian to non-Newtonian flow) remain unaltered at the nanoscale as indicated by changes in the strain rate sensitivity and deformation morphology. However, measurements and observations of the transition from Newtonian to non-Newtonian flow suggest an increased accommodation of free volume at the nanoscale potentially allowing higher strain rates or stresses to be employed during forming. Thus, while bulk measurements should serve as a suitable guide when designing a thermoplastic forming operation, this work provides important insights for thermoplastic forming of nanoscale features. Finally, our high temperature study presented here in con-

junction with our previous studies at low temperature^{259, 260} further indicate that the observed brittle-to-ductile transition^{264, 275, 276} in amorphous metals is likely mediated by processing effects which could be intertwined with true size effects.

5.4. Conclusion

In summary, we presented a series of experiments to investigate the deformation of nanoscale MGs at elevated temperature. To investigate the high temperature deformation of nanoscale MGs we conducted thermomechanical tests on individual MG nanowires. By varying the power dissipated and applied load a deformation map was constructed from failure morphologies and estimated strain rate sensitivities. The deformation map revealed a transition from Newtonian to non-Newtonian flow at strain rates consistently higher than the average bulk transition. Shifting the flow transition to higher strain rates is consistent with the accommodation of larger amounts of free volume produced by plastic deformation. We hypothesize that the difference in behavior is due to enhanced relaxation at the free surface and a lower steady state free volume resulting from the fabrication process. These experiments are expected to have potential impact on future thermoplastic forming operations by demonstrating that the deformation mechanisms are fundamentally similar across four orders of magnitude in length scale. The results of our work also suggest that higher strain rates or stresses may be employed at the nanoscale owing to the enhanced capacity for free volume production in the Newtonian flow regime, and point to the

importance of sample processing in mediating the ensuing deformation behavior.

Chapter 6

Vapor Deposited Metallic Glass Thin Films

In the preceding chapters, the interplay between reduced length scale, sample history, and mechanical properties was explored in metallic glass nanowires. Observations of the effect of ion irradiation, high temperature annealing, and thermoplastic flow reveal a potentially wider range of achievable structural states as indicated by differences in T_f . Despite these continuing advances in understanding the interplay between processing, structure, and properties in MGs, post-glass forming treatments dominate efforts to control mechanical properties in MGs and the bounds of structural state have yet to be established.

In contrast, control over structural state in organic glasses at the time of production has been achieved in physical vapor deposited (PVD) organic glasses^{317, 318}. By varying the substrate temperature during deposition, the structural state, as indicated by the fictive temperature, and material properties are controlled³¹⁷⁻³¹⁹. In addition, a unique glassy state with exceptionally low fictive temperature and enhanced stability, referred to as an ultrastable glass, was produced in organic glasses and thin film MGs³²⁰, as a result of enhanced surface mobility enabling adatoms to diffuse to a lowest energy disordered configuration³²¹. Thus, while the ultrastable glass is likely

the lowest energy bound on structural state, highly liquid-like structures may also be produced by PVD owing to effective cooling rates far greater than conventional thermal processing; this full spectrum of structural states has not been investigated in PVD thin film MGs. Therefore, based on the isochemical control over structural state, PVD deposition of thin film MGs is proposed as a method to tailor the hardness, modulus, and plastic deformation response at the time of glass formation rather than through tailoring alloy composition or post-glass forming treatments.

6.1. Characterization of Sputtered Thin Films

The measured compositions of all thin films are summarized in Table 3. Here, the error is estimated from the percent error when fitting the spectra. The results demonstrate that the substrate temperature does not affect the film composition, implying that all property changes reflect isochemical changes in the glass. In addition, the average film composition is $\text{Pd}_{78.3}\text{Cu}_{6.2}\text{Si}_{15.5}$, which agrees well with the target compositions of $\text{Pd}_{77.5}\text{Cu}_6\text{Si}_{16.5}$. The oxygen content was also analyzed by EDS. Given the challenges in assessing light elements by EDS we focus on the qualitative result that most thin films appeared to have consistent oxygen content with two notable exceptions. The room temperature and 483K deposited thin films contain approximately 100% and 50% more oxygen than the remaining thin films, respectively.

Figure 6.1 shows structural characterization of the MG thin films. XRD patterns for thin films deposited at an actual substrate temperature of 333 K, 394 K, 461 K,

Table 3: Composition of sputtered Pd-based MG thin films at different substrate temperatures as determined by EDS. The errors are determined from the percent error when fitting the EDS spectra.

Substrate Temperature (K)	Pd (at. %)	Cu (at. %)	Si (at.%)
298	77.6 ± 10	6.2 ± 1.0	16.2 ± 1.7
333	78.6 ± 10	6.2 ± 0.9	14.6 ± 1.7
394	79.7 ± 10	5.9 ± 0.9	15.6 ± 1.6
461	78.7 ± 10	6.3 ± 1.0	15.0 ± 1.6
483	77.3 ± 10	6.5 ± 1.0	15.8 ± 1.7
553	77.5 ± 10	6.5 ± 1.0	15.9 ± 1.6

483 K, and 553 K (Figure 6.1a) show characteristic amorphous patterns, indicated by a single diffuse peak around $40^\circ 2\theta$ at elevated temperatures. In contrast, the film deposited at 298 K is crystalline as indicated by the narrow peak at $40^\circ 2\theta$ and the secondary peak around $46^\circ 2\theta$, which likely correspond to the (111) and (200) peaks from a crystalline Pd phase. XRD observations are supported by bright field TEM cross-sectional images, where a thin film deposited at 298 K shows clear evidence of crystallites, which is supported by the inset selected area electron diffraction pattern (SAED) (Fig. 1b). Bright field TEM observations on a cross section of a representative glassy thin film deposited at 461 K shows that the film is featureless and the SAED pattern shows only diffuse hallos which indicates an amorphous structure (Fig. 1c).

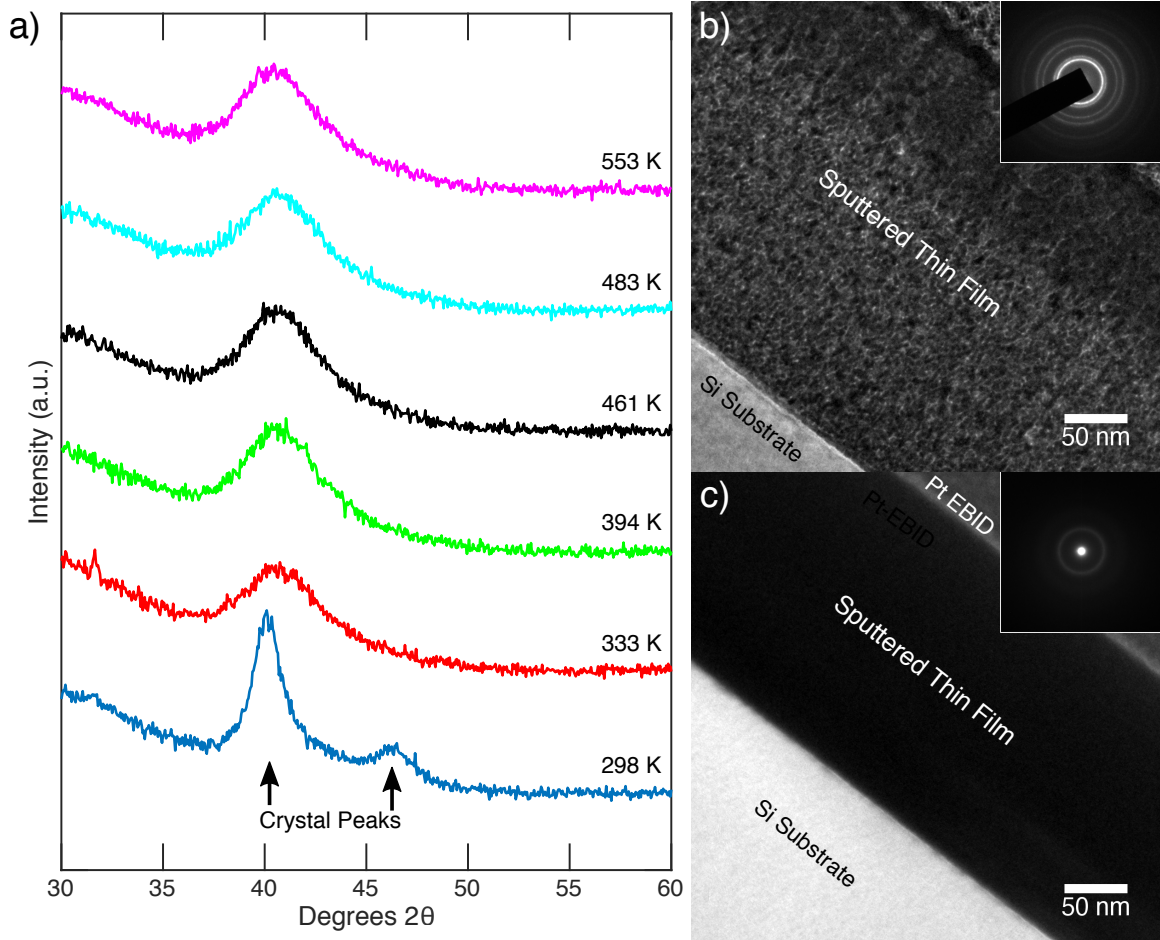


Figure 6.1: a) Structural characterization of sputtered thin films was performed by XRD. The thin film deposited at 298 K appeared crystalline as indicated by the two distinct crystal diffraction peaks, which likely correspond to the (111) and (200) peaks from a crystalline Pd phase. All other films were x-ray amorphous as indicated by the single broad diffraction peak. XRD observations were supported by TEM on the 298 K film b) and 461 K film c). Again the 298 K film appeared crystalline as evidenced by bright field contrast within the film and multiple sharp diffraction rings in the electron diffraction pattern (inset). The 461 K film was amorphous as evidenced by the lack of contrast within the film and diffuse halos in the electron diffraction pattern (inset).

6.2. Mechanical Properties

The nanoindentation of MG films on their native deposition substrates was performed using the CSM method and the depth-resolved results are shown in Figure 6.2. The Oliver-Pharr modulus and hardness depth profiles are shown in Figure 6.2a and Figure 6.2b, respectively. Here, each point is an average of 16 indentations and the error bar is the standard deviation of the included data. The 298 K film shows an apparent plateau in modulus and hardness at indentation depths between 25 nm and 50 nm before rapidly increasing. All other films show increasing hardness and modulus before plateauing by 50 nm for the 333 K film and 25 nm for the remaining thin films.

Due to the small difference ($\sim 10\%$) between the modulus of the MG films and Si, the substrate has a limited effect on the Oliver-Pharr modulus and hardness for indentation depths smaller than 25 % of the film thickness^{322, 323}. Furthermore the increases in modulus and hardness at small depths (< 20 nm) are likely due to the indenter tip blunting and surface roughness³²⁴. Accordingly, to compare the effect of deposition temperature an average modulus and hardness are extracted by averaging over 45-55 nm of indentation depth and are plotted in Figure 6.2c. The depth windows are indicated in Figure 6.2a,b. From Figure 6.2c it is observed that the modulus and hardness increase with increasing deposition temperature until 461 K, indicative of an increasingly relaxed glass structure. Above 461 K the modulus and hardness decrease with increasing substrate temperature suggesting more rejuvenated glasses at higher temperatures.

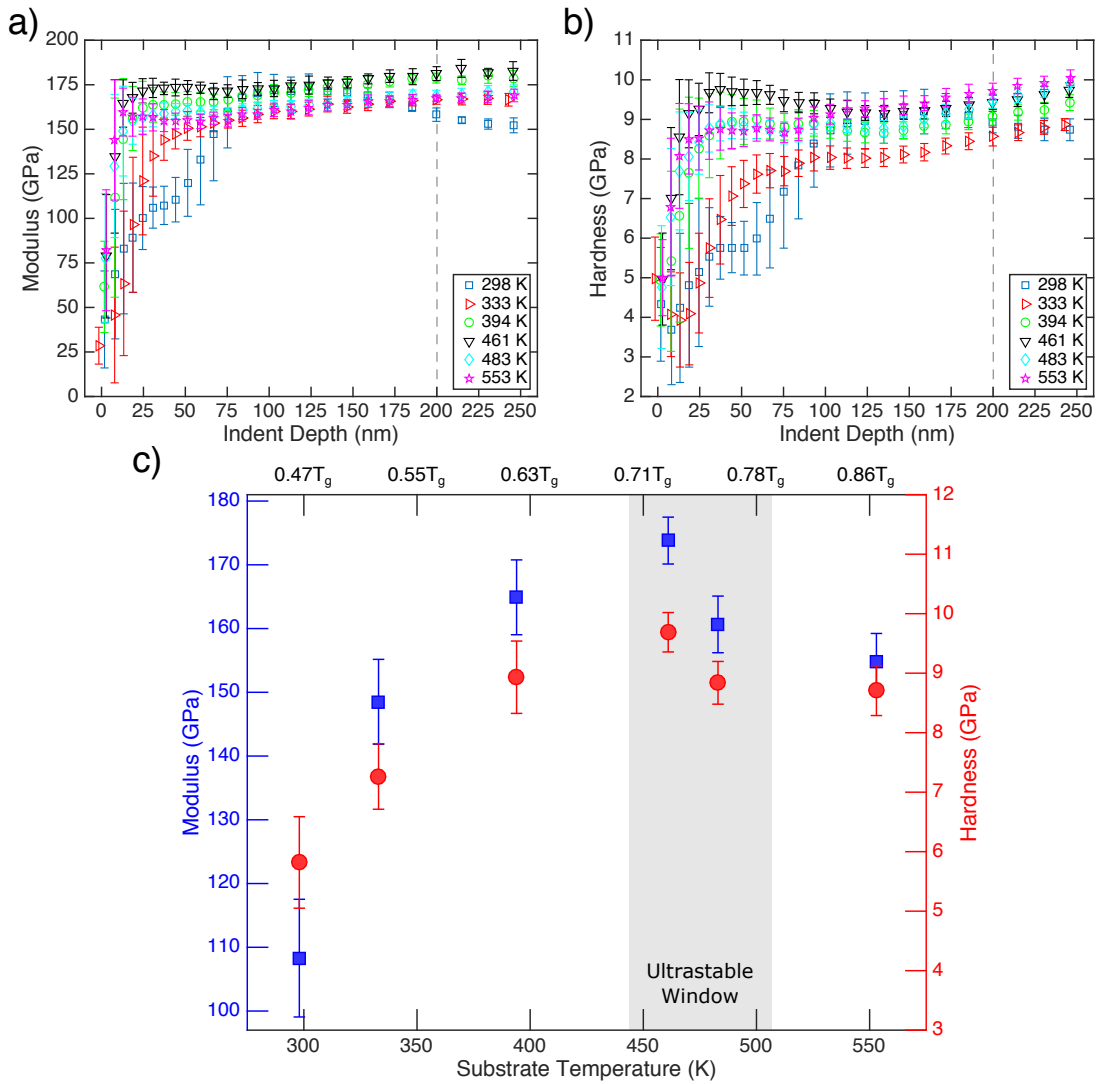


Figure 6.2: Modulus and hardness were measured by nanoindentation using the continuous stiffness method. The depth profiles for modulus and hardness are shown in a) and b) respectively. The film properties were then determined as an average over the depth range of 45-55 nm. The resulting average mechanical properties are presented in c) as a function of the measured substrate temperature. The error bars represent the standard deviation across the sampled depth window.

To elucidate differences in plastic deformation accommodation modes for films deposited in different structural states, the deformation morphology in the vicinity of the indent impressions was also observed by in situ scanning probe imaging. Figure 6.3 shows gradient force images of the indent morphologies, which are the scanning probe set point error and indicate the slope of the surface. The force images are selected to aid in clearly identifying topological features due to the increased sensitivity to changes in height. The identified surface features are then analyzed from the height images. The 298 K film shows no pileup around the indent indicating that no shear bands form when the film is crystalline. As the deposition temperature increases shear bands are observed around the indent, primarily at the top of the impression. At 333 K a few large shear bands are identified at the top of the indent, with an average step height difference of 10.6 nm. As the substrate temperature increases the shear bands become more pronounced and become visible at the lower left edge of the indents. The thin film deposited at 461 K exhibits the largest and most distinct shear bands with an average step height of 12.55 nm. Above 461 K the shear bands become less distinct until shear bands are poorly resolved at 553 K. However, measurement of the step heights reveal an average shear band height of 10 nm, which qualitatively agrees with the shear band heights at 333 K. In addition, it is important to note that the observation of shear bands is influenced by potential variations in indent depth under the same applied load. In particular, the 333 K film was indented deeper than the 461 K film potentially resulting in larger shear bands. Yet the 461 K film showed

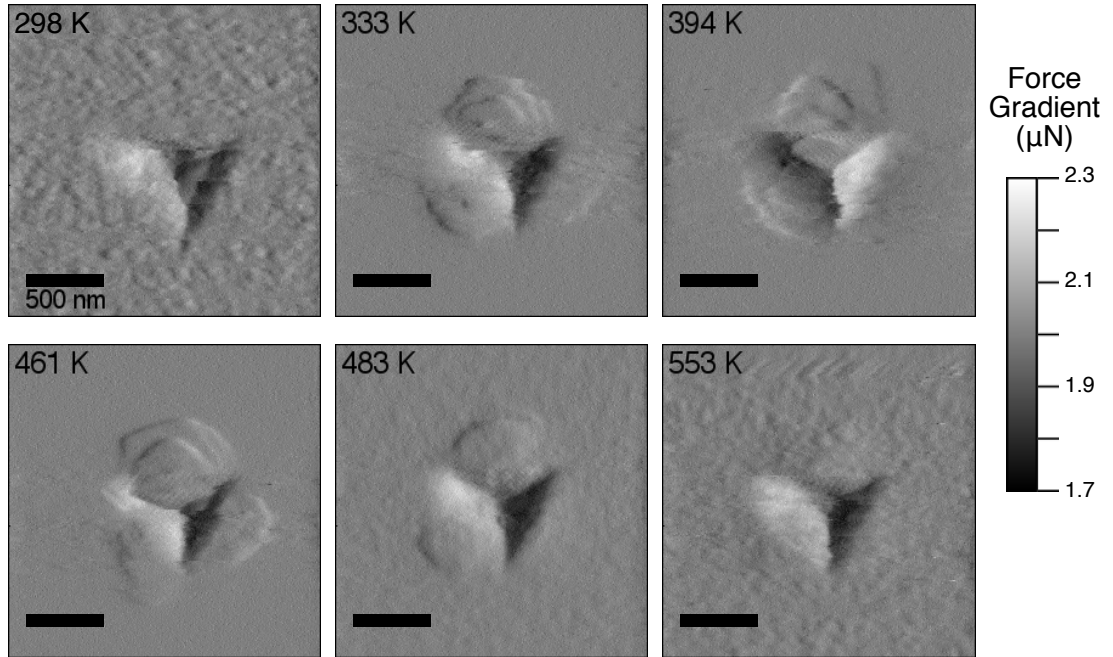


Figure 6.3: Indent morphologies are observed in situ after indenting to $2000 \mu\text{N}$ using the scanning probe mode under an applied load of $2 \mu\text{N}$. Here, gradient force images, which are the scanning probe set point error and indicate the slope of the surface, are shown to identify changes in indent morphology. As the deposition temperature increases shear bands become more pronounced with the 461 K film showing the most distinct shear bands. Further increasing the deposition temperature results in less distinct shear bands. While interpretation of the indent morphology is complicated by potential influence of the substrate the 461 K film showed the shallowest indent and the largest indents, which emphasizes its most well relaxed structure.

the largest shear bands despite having the shallowest indent. Thus, while variations in indent depth influence the observation of shear bands, careful analysis reveals a transition in shear band behavior towards relatively large, distinct shear bands in the most relaxed structural state.

6.3. Structural State in Sputtered Thin Films

From the nanoindentation results it is evident that the substrate temperature strongly influences the resulting mechanical properties through isochemical modifications to the glassy structure. The hardness increases from 7.26 ± 0.55 GPa at 333 K to 9.69 ± 0.33 GPa at 461 K, a difference of 2.43 GPa (33.5% increase). Further increasing the deposition temperature results in decreasing hardness to 8.71 GPa at 553 K. The changes in hardness are further reflected in changes in indent morphology, highlighting changes in both the extent and mode of plastic deformation. Taken as a whole, the changes in mechanical response are indicative of changes in glass structural state that are not reflected in scattering measurements (Figure 6.1) and a most relaxed glass occurring at 461 K ($0.73T_g$ for the bulk glass³²⁵).

In the context of ultrastable glasses from the literature³¹⁷⁻³²⁰ we find favorable comparisons in the reported trends in thermal properties with our mechanical property measurements. Here, the observed changes in the mechanical response complement calorimetric measurements from the literature on PVD metallic and organic glasses, which demonstrate smoothly varying structural states as the deposition temperature is varied. In sputtered metallic glasses Samwer et al. found that as the deposition temperature increased up to the ultrastable condition, the measured T_g shifted to higher temperatures indicating enhanced kinetic stability of the glass³²⁰. Similarly, a transition to higher T_g and a minimum in T_f is observed in the ultrastable state of organic glasses further indicating that the ultrastable glass has both enhanced kinetic

stability and exceptionally relaxed structure³¹⁷. These trends in kinetic stability and fictive temperature are mirrored by the measured increase then decrease in hardness and modulus with increasing deposition temperature found in our sputtered MG thin films. Furthermore the peak in mechanical properties was observed at 461 K ($0.73T_g$). This maximum falls within the expected range ($0.7T_g$ to $0.8T_g$) of temperatures, indicated in Figure 6.2c as the shaded grey region, for the formation of ultrastable MGs as reported by Samwer et al³²⁰.

However, we also observe that the film deposited at 483 K ($0.76T_g$) lies within the expected ultrastable deposition temperature window. Yet the 483 K film shows a lower hardness of 8.84 GPa compared to the 461 K film. This discrepancy likely stems in part from the higher oxygen content (50 % higher than) in the 483 K film. Increased oxygen content has been linked to decreased strength³²⁶ and worse glass forming ability³²⁷. The detrimental effect of oxygen on glass forming ability likely contributes to the crystallization observed in the thin film deposited at 298 K, which showed twice the oxygen content, as well.

Taken as a whole the mechanical property results suggest two deposition regimes, which agrees well with previous reports on both organic and metallic glasses^{317, 318, 320}. At low temperatures, below the peak modulus and hardness condition, increasing the deposition temperature results in a more relaxed structural state. At high temperatures, above the peak modulus and hardness condition, further increasing the deposition temperature results in a more rejuvenated structural state. In both regimes, the

resulting structure is determined by the increased surface mobility of vapor deposited adatoms as compared to atoms in the bulk^{317, 318}. In the low temperature regime increasing the substrate temperature increases the surface mobility and allows adatoms to find deep positions in the PEL. In contrast, in the high temperature regime, the adatoms have high mobility. As a result, the adsorbed atoms have sufficient thermal energy to overcome local energy barriers and move up the rugged PEL landscape. This suggests that the high mobility surface atoms behave similarly to the supercooled liquid^{317, 318}, leading to structures and properties analogous to quenched glasses.

In order to quantify the changes in structural state and develop relationships between mechanical and thermal properties we apply a previously developed model for metallic glass strength²⁶⁰. Briefly, the mechanical energy required to initiate plasticity in a MG is equated to the thermal energy required to reach the glass transition^{14, 15}. This equivalence is supported by simulations which observe a simple scaling relationship between temperature and glass strength³⁰⁰. By applying the model and comparing two MGs prepared in different structural states, changes in strength can be equated to changes in fictive temperature, which describes the temperature at which a glass structure would be at equilibrium, as $\Delta T_f = -\Delta\sigma_y V / (C_{pl} - C_{pg})$, where ΔT_f is the difference in fictive temperature, $\Delta\sigma_y$ is the change in yield strength, V is the molar volume, C_{pl} is the supercooled liquid heat capacity extrapolated from well above T_g , and C_{pg} is the glass heat capacity extrapolated from well below T_g ²⁶⁰. Using an experimentally determined Tabor factor of $H/3.5 = \sigma_y$ ²²⁰, $C_{pl} - C_{pg} \approx 18.6 \text{ J/mol}\cdot\text{k}$ ³²⁵,

and a calculated molar volume of $8.92 \text{ cm}^3/\text{mol}$, T_f is estimated to increase by 333 K from the 333 K film to the 461 K film. Similarly comparing the 461 K deposition to the 553 K deposition suggests a fictive temperature decrease of 134 K by increasing the deposition temperature past the peak hardness condition. Owing to the potential influence of the substrate and potential indentation strain rate effects³²⁸ the estimated fictive temperature changes are likely an upper bound. Regardless this large difference signifies large variations in glass structure that are potentially beyond the limits of conventional MG processing effects, such as changing cooling rate or severe plastic deformation processes^{139, 198}. Furthermore these changes in glass structure are enacted at the time of glass formation at temperatures and time scales far below those necessary for post-processing structural relaxation treatments³²⁹.

As a result, the hardness results point towards the range of structural states achievable in this Pd-based MG. Here, one limit is the apparent ultrastable glass deposited at 461 K; this represents the most relaxed glass possible. The other observed limit is the film deposited at 333 K, which shows the lowest hardness indicating the most rejuvenated glass. The fictive temperature analysis suggests that the most relaxed and most rejuvenated glasses differ by 6.19 kJ/mol in excess enthalpy, which indicates a 333 K difference in T_f . In comparison to previous reports on fictive temperature differences, this is beyond the variation in T_f ($\sim 100 \text{ K}$) achievable through annealing⁹¹. Furthermore, the changes in excess enthalpy and T_f due to different deposition temperatures are greater than the previously reported changes

due to both ion irradiation and high pressure torsion in a Pt-based glass ($\sim 3 \text{ kJ/mol}$ and $\sim 100 \text{ K}$)²⁶⁰ and Zr-based glasses ($\sim 4.5 \text{ kJ/mol}$ and $\sim 150 \text{ K}$)^{198, 330}.

6.4. Conclusion

In conclusion, we have demonstrated isochemical control over thin film MG properties by varying the deposition temperature. Rather than relying on post processing, the structural state and resulting mechanical properties and deformation morphology are programmed at the time of glass formation. Based on the hardness increase of 2.19 GPa we estimate T_f to increase by 300 K, which exceeds fictive temperature differences enacted by previously explored methods including thermal treatments, ion irradiation and high pressure torsion. This control arises due to the different role of enhanced surface mobility in a low and high temperature deposition regime. As a consequence, these results indicated that varying the deposition temperature during PVD enables the greatest range of glass structural states, from ultrastable to highly liquid-like, to be achieved in metallic glasses.

Chapter 7

Conclusion and Perspectives

In this dissertation, we have explored the interplay between processing and mechanical properties in metallic glasses. Despite significant interest in employing MGs as structural materials, particularly at the micro- and nanoscale, a holistic understanding of how processing determines properties has remained surprisingly absent. In order to quantify the effect of processing on MGs the excess enthalpy and fictive temperature were proposed to be appropriate structural metrics for glass structural state. We then considered methods previously employed to relax or rejuvenate MG structures, leading to lower excess enthalpies and fictive temperatures or higher excess enthalpies and fictive temperatures respectively. The effects of reducing MG specimen size to the micro- and nanoscale and the resulting mechanical properties were then considered. Here, it was found that potential size effects were convoluted with the strong processing sensitivity of metallic glasses.

In order to shed light on the processing sensitivity of MGs and explore potential size effects we employed thermoplastically molded MG nanowires and novel nanomechanical testing techniques. In Chapter 3 we first demonstrated that controlled ion irradiation in the FIB resulted in a transition from bulk-like tensile deformation, characterized by brittle failure and shear band fracture morphologies, to quasi-homogenous deformation, as indicated by the observation of plastic deformation and suppression

of shear bands, in MG nanowires. We further found that annealing under conditions known to relax the MG structure reversed the effect of the FIB irradiation. These findings indicated that potential size effects are likely convoluted with potential processing effects. Furthermore, it was revealed that reduction of length scale allows access to a potentially unique tunability of MG structure, and hence mechanical response.

To further understand the effect of ion irradiation on the tensile behavior of molded MG nanowires a systematic study of FIB irradiation was presented in Chapter 4. By systematically controlling both the ion fluence and irradiated volume fraction a trend towards homogeneous deformation, increased tensile ductility, and reduced yield strength were found. However, electron diffraction observations revealed only subtle changes in MG structure. In order to understand the effect of processing on MG structure and strength a model for glass strength was developed that specifically incorporated excess enthalpy to account for structural differences. The changes in excess enthalpy were further extended to differences in fictive temperature. Together, the changes in excess enthalpy and fictive temperature, as estimated from changes in strength, suggest structural changes beyond the limits of conventional thermal processing.

In order to gain a greater understanding of the thermoplastic molding process employed to fabricate the MG nanowires the high temperature flow response was measured in Chapter 5. Using software feedback on both applied load and electrical power dissipation, the stress and temperature applied to individual nanowires was

varied. By considering the strain rate sensitivity and failure morphology a transition from Newtonian to non-Newtonian flow was observed. By comparing to collective bulk flow behavior, the flow transition was found to occur at higher strain rates, indicating an enhanced ability to annihilate strain induced free volume. This suggests that the free surface may be an effective sink for free volume leading to faster relaxation.

Finally, physical vapor deposition was explored as a method to determine the structural state in MG thin films at the time of deposition in Chapter 6. We demonstrated that varying the substrate temperature for sputter deposition from an alloy target leads to isochemical variation in mechanical properties. In agreement with reports from the organic glass literature, two deposition regimes were found. At a low temperatures increasing the deposition temperature produces a more relaxed glass with enhanced mechanical properties. Above a critical substrate temperature, increasing the deposition temperature results in a more rejuvenated glass with decreased hardness and modulus. These thin film growth regimes are understood to arise from increased surface mobility enabling to explore low energy configurations and escape to high energy configurations in the low and high temperature regimes respectively.

Collectively, the work presented in this dissertation offers several key implications. First, it was demonstrated that the mechanical response of MGs at small length scales is a convolution of the strong processing sensitivity of MGs with potential size dependent behavior. This manifests as an enhanced ability to vary structural state at the nanoscale and subtle differences from the bulk response, namely higher tensile

strengths and greater accommodation of plasticity induced free volume at elevated temperatures. Second, a general approach for quantifying MG structural state was developed, pointing to a potential structural state – processing – property relationship for MGs. Specifically the relationship between glass strength and structural metrics, including excess enthalpy and fictive temperature, suggests glass behavior is easily predicted from thermodynamic quantities. Finally, a method for accessing the full range of potential structural states was demonstrated. By fabricating MG thin films via PVD at different substrate temperatures the structural state was varied at the time of glass formation from an ultrastable glass to a highly rejuvenated glass.

Based on these conclusions, several avenues for future investigation are suggested. First, a calorimetric study of sputtered thin film metallic glasses should be conducted. For instance, several nanocalorimetric measurement techniques for thin films have been reported^{331–335}. Such a study would provide a measurement of the excess enthalpy and fictive temperature for incorporation into the model for metallic glass strength, further strengthening the proposed structural state – processing – property relationship.

In addition, calorimetric measurements would enable investigation of changes in kinetic process such as the glass transition and crystallization. Previous studies in both organic and metallic glasses indicate significant changes to the glass transition^{317, 318, 320}. However, the effect of heating rate, which strongly influences the glass transition and other processes^{81, 83, 88}, has not been investigated. Such an investigation would be further enhanced by the wide range of cooling rates achievable by thin film

nanocalorimeter^{334, 335}.

Additionally, a measure of energy dissipation as a function of structural state is highly desirable. While global changes in elastic modulus are observed, it is unclear how the underlying elastic interactions are affected. Furthermore, a measure of energy dissipation would enable better comparison to the PEL model for MG structural state and mechanics. A potential avenue for measuring energy dissipation is through amplitude-modulation atomic force microscopy. When operated in a purely repulsive contact the cantilever phase shift may be related to dissipation of energy in the contact³³⁶. This technique has previously been employed to investigate the mechanical heterogeneity in MG thin films^{57, 160, 337, 338}. However, while shifts in the average dissipation were observed in annealed¹⁶⁰ and ultrastable MGs³²⁰, there is still a need to specifically explore the interrelationship between structural state and energy dissipation.

Similarly, the effect of glass composition on the range of achievable structural states merits investigation. Specifically, the role of fragility, which describes the temperature dependence of relaxation behavior around T_g ³³⁹, depends on glass composition and plays a role in MG properties³⁸. Here, a low fragility indicates weak temperature dependence while high fragility indicates strong temperature dependence. Furthermore, the fragility correlates with entropic contributions to free energy^{340, 341} and affects the Kauzmann temperature, the temperature at which the entropy difference between glass and crystal reaches zero^{37, 342}. Simulations and experiments

on vapor deposited glasses also suggested that the Kauzmann temperature affects formation of ultrastable structures^{321, 329, 343, 344}. As a result, MG fragility may be varied^{345, 346} and likely plays a role in determining the ideal condition for formation of an ultrastable glass.

Finally, the holistic consideration of how MG processing affects properties suggests novel materials architectures based around MGs. Specifically, the design of kinetically controlled MG composites is proposed. These MG composites would take advantage of the strong temperature dependence of relaxation and rejuvenation process in metallic glasses to create new materials with controllable deformation response. For instance, composite coatings may be produced by PVD. As demonstrated in Chapter 6, the mechanical properties of MG thin films is determined at the time of deposition by the substrate temperature. Therefore, both spatial and temporal temperature gradients may be used to create alternating regions of MGs with low fictive temperature to impart high strength and high fictive temperature to provide damage tolerance.

Similar structures at bulk length scales may also be produced through a combination of mechanical and thermal processes as well. By combining two MGs with significantly different glass transition temperatures, the low T_g glass could be relaxed at time scales that do not affect the high T_g glass structural state. Again regions of MGs with low fictive temperature impart high strength while high fictive temperature areas provide damage tolerance.

Appendix A

Operation of SmarPod Nanomechanical Testing Apparatus

In the following Appendix a step by step guide to safe installation, operation, and uninstallation of the SmarPod nanomechanical testing apparatus is described. This guide is intended to assist in the installation and operation of the SmarPod in the either the Quanta or FIB (full and proper training must be completed on these instruments first). This Guide describes the necessary steps for safe installation of the SmarPod and PI micro/nano mechanical testing apparatus which uses the FemtoTools load cells.

A.1. Required Equipment

The following equipment is required to operation of the SmarPod nanomechanical testing apparatus:

- The Gianola Group laptop cart
- Keithley 2100 digital multimeter
- Labview USB Compact DAQ
- PI actuator control amplifier with appropriate sensor module

- FemtoTools USB controller
- All SmarPod and actuator apparatus Components
- Any additional equipment necessary for your experiment

A.2. Installation Procedure

1. Log into the microscope and vent the chamber. While venting move the stage to $x=0$, $y=0$, and z =minimum height (either home the stage or simply move to the coordinate)
2. At this time plug in the cart power strip and start the laptop
3. Vent the SmarPod vacuum storage pod and remove the load cell boxes. Set the load cells to the side.
4. Once the chamber is vented, set the actuator on the microscope bench to the side of the chamber. Plug in the vacuum and air-side Actuator cables. Carefully arrange the vacuum side cables under the microscope stage such that the cables do no interfere with critical microscope components.
5. Turn on the Keithley 2100. Once the Keithley is fully started, turn on the actuator control box and check the voltage read out. The voltage should read around 6 mV. If this reading is not correct ensure there is no applied offset voltage and that all cables are properly connected.

6. Manual sweep the voltage on the Actuator using the DC Offset knob over the full range of expected operation.
7. Return the DC Offset to 0 V and turn off the actuator. **Pumping/venting the microscope with the actuator powered on can cause severe and permanent damage to the actuator.**
8. Holding the SmarPod firmly by the baseplate lift it out of the storage pod while also supporting the cables. Place on microscope stage and secure using the three screws in the baseplate (2.5mm Allen wrench). **Be careful not to over tighten the screws or torque the microscope stage.**
9. Connect the SmarPod vacuum and air-side cables ensuring 'A' is connected to 'A' and 'B' is connected to 'B.' **When handling the vacuum side cable always handle by the two large LEMO connectors and support the remainder of the cable.** The weight of the large connectors may be sufficient to damage the internal cable components if improperly handled.
10. Connect the vacuum side cable to the SmarPod baseplate by the three plastic connectors. Again ensure 'A' is connected to 'A,' 'B' is connected to 'B,' and 'C' is connected to 'C.' The cables are labeled by washers attached to the plugs while the baseplate has labels scribed onto the connector block.
11. Turn on the SmarPod control box and start the SmarPod software. After a few seconds click Connect. If the software fails to connect check cable connections

and restart software before reconnecting.

12. Run the Reference function in the software. After referencing perform several trial movements to ensure proper operation.
13. Move the SmarPod to (0, -10 mm, 0). This position is stored in the software as “Sample Load Position.”
14. Attach the vacuum and air-side FemtoTools cables and set them out of the way
15. Mount sample to the actuator then attach the Actuator bracket to the SmarPod baseplate. Adjust the position of the bracket such that your sample is as close to the center as possible.
16. Connect the FemtoTools Controller and start the FemtoTools software.
17. Click “Connect,” select the desired channel, and set the scale to “Auto.”
18. Set the gain to 1 and zero the reading. Plug in the ribbon cable adapter. The load should now read about 1.4 V. Connect the air-side cable to the adapter
19. Place the desired load cell on the top of the chamber door. Remove the case by rotating it away from the silicon device portion.
20. Connect the vacuum-side cable to the load cell. The load should now read between 2 and 2.3 V.

21. If excessive noise is observed, attach the ground pin on the rear of the Femtotools controller with a jumper to the cable feed through flange and the FemtoTools controller ground. The peak to peak signal should be less than 1 mV at 200 Hz.
22. While holding the load cell by the cable plug, unscrew it from the post (1.5 mm Allen wrench) and mount it to the SmarPod. **Do not apply pressure to the SmarPod. Doing so may slip the piezoelectric actuators, damage the actuators, or release the top plate from its frictional couplings.**
23. Approach your sample with the SmarPod. Move the load cell as close to the sample as possible now as this coarse alignment is much easier in air.
24. Ensure that all cables are safely positioned and close the chamber door. **Attempting to pump the chamber with cables in the seal will severely damage the cables and may cause the microscope to shutdown.**
25. Pump the chamber the microscope chamber.

A.3. Operation Checklist

1. Start the appropriate Labview Program for the test you will be performing.
2. Once the desired base pressure is attained, start the SEM high voltage and locate the sample. Turn on the Actuator control box and ensure the proper voltage reading.
3. Raise the sample to the proper working distance, align the sample (stage or

beam rotation) and perform all beam alignments

4. Locate the load cell tip and perform in plane alignment.
5. Observe the working distance and move SmarPod such that it is at the same working distance as your sample.
6. Carefully approach your sample using progressively smaller movements and speeds.
7. Fine tune the SmarPod height and perform your mechanical test.
8. After your test, move your sample safely away from the load cell and set the Labview control voltage to 0 V.

A.4. Uninstallation Checklist

1. Ensure there are no applied voltages to the Actuator and turn off the control box. **Venting the chamber with the Actuator powered on can cause severe and permanent damage to the actuator.**
2. Move the SmarPod a safe distance away from your sample.
3. Vent the chamber.
4. Uninstall the load cell and return it to the appropriate box.
5. Detach the Actuator bracket from the SmarPod baseplate and set it on the microscope bench. Remove your sample.

6. Move the SmarPod to the zero position. Click “Disconnect” and turn off the control box.
7. Disconnect all vacuum-side cables
8. Return the SmarPod to the vacuum storage pod. Remount the Actuator bracket to the SmarPod baseplate.
9. Safely stow all cables and load cells in the vacuum storage pod.
10. Disconnect all air-side cables.
11. Close and pump the chamber.
12. Unplug the FemtoTools controller and shut down the laptop.
13. Turn off any remaining equipment. Unplug the cart power strip.
14. Log off of the microscope.

Bibliography

- [1] M. Soinski, W. Bulica, K. Cieslewicz, and J. Szczyglowski, “Current transformer with cut core made of metallic glass ribbon,” *Ieee Trans. Magn.*, vol. 24, pp. 1871–1872, 1988.
- [2] G. Konczos, É. Kisdi-Koszó, and A. Lovas, “Recent progress in the application of soft magnetic amorphous materials: alloys, preparation, devices,” *Phys. Scr.*, vol. T24, pp. 42–48, 1988.
- [3] V. R. V. Ramanan, “Metallic glasses in distribution transformer applications: an update,” *J. Mater. Eng.*, vol. 13, pp. 119–127, 1991.
- [4] A. Inoue and A. Takeuchi, “Recent development and application products of bulk glassy alloys,” *Acta Mater.*, vol. 59, pp. 2243–2267, 2011.
- [5] H. Matsumoto, A. Urata, Y. Yamada, and A. Inoue, “Novel FePBNbCr glassy alloys SENNTIX with good soft-magnetic properties for high efficiency commercial inductor cores,” *J. Alloys Compd.*, vol. 509, pp. S193–S196, 2011.
- [6] a. Inoue, F. Kong, S. Zhu, E. Shalaan, and F. Al-Marzouki, “Production methods and properties of engineering glassy alloys and composites,” *Intermetallics*, vol. 58, pp. 20–30, 2015.
- [7] W. Klement, R. H. Willens, and P. Duwez, “Non-crystalline structure in solidified goldsilicon alloys,” *Nature*, vol. 187, pp. 869–870, 1960.
- [8] W. L. Johnson, “Bulk amorphous metal - an emerging engineering material,” *Jom*, vol. 54, pp. 40–43, 2002.
- [9] A. Inoue, X. M. Wang, and W. Zhang, “Developmens and applications of bulk metallic glasses,” *Rev. Adv. Mater. Sci*, vol. 18, pp. 1–9, 2008.
- [10] C. Schuh, T. Hufnagel, and U. Ramamurty, “Mechanical behavior of amorphous alloys,” *Acta Mater.*, vol. 55, pp. 4067–4109, 2007.
- [11] M. Ashby and A. Greer, “Metallic glasses as structural materials,” *Scr. Mater.*, vol. 54, pp. 321–326, 2006.

- [12] M. Chen, “Mechanical behavior of metallic glasses: microscopic understanding of strength and ductility,” *Annu. Rev. Mater. Res.*, vol. 38, pp. 445–469, 2008.
- [13] W. Johnson and K. Samwer, “A Universal Criterion for Plastic Yielding of Metallic Glasses with a $(T/T_g)^{2/3}$ Temperature Dependence,” *Phys. Rev. Lett.*, vol. 95, pp. 2–5, 2005.
- [14] B. Yang, C. T. Liu, and T. G. Nieh, “Unified equation for the strength of bulk metallic glasses,” *Appl. Phys. Lett.*, vol. 88, p. 221911, 2006.
- [15] Y. Liu, C. Liu, W. Wang, A. Inoue, T. Sakurai, and M. Chen, “Thermodynamic origins of shear band formation and the universal scaling law of metallic glass strength,” *Phys. Rev. Lett.*, vol. 103, p. 065504, 2009.
- [16] M. Barmatz and H. S. Chen, “Young’s modulus and internal friction in metallic glass alloys from 1.5 to 300 K,” *Phys. Rev. B*, vol. 9, pp. 4073–4083, 1974.
- [17] N. Morito and T. Egami, “Internal friction and reversible structural relaxation in the metallic glass Fe₃₂Ni₃₆Cr₁₄P₁₂B₆,” *Acta Metall.*, vol. 32, pp. 603–613, 1984.
- [18] J. J. Lewandowski, W. H. Wang, and A. L. Greer, “Intrinsic plasticity or brittleness of metallic glasses,” *Philos. Mag. Lett.*, vol. 85, pp. 77–87, 2005.
- [19] M. D. Demetriou, M. E. Launey, G. Garrett, J. P. Schramm, D. C. Hofmann, W. L. Johnson, and R. O. Ritchie, “A damage-tolerant glass,” *Nat. Mater.*, vol. 10, pp. 123–8, 2011.
- [20] A. L. Greer, K. L. Rutherford, and I. M. Hutchings, “Wear resistance of amorphous alloys and related materials,” *Int. Mater. Rev.*, vol. 47, pp. 87–112, 2002.
- [21] A. Inoue, B. Shen, H. Koshiba, H. Kato, and A. R. Yavari, “Cobalt-based bulk glassy alloy with ultrahigh strength and soft magnetic properties,” *Nat. Mater.*, vol. 2, pp. 661–3, 2003.
- [22] J. P. Chu, J. C. Huang, J. S. C. Jang, Y. C. Wang, and P. K. Liaw, “Thin film metallic glasses: preparations, properties, and applications,” *Jom*, vol. 62, pp. 19–24, 2010.
- [23] J. P. Chu, J. S. C. Jang, J. C. Huang, H. S. Chou, Y. Yang, J. C. Ye, Y. C. Wang, J. W. Lee, F. X. Liu, P. K. Liaw, Y. C. Chen, C. M. Lee, C. L. Li, and C. Rullyani, “Thin film metallic glasses: unique properties and potential applications,” *Thin Solid Films*, vol. 520, pp. 5097–5122, 2012.
- [24] T. Fukushige, S. Hata, and A. Shimokohbe, “A MEMS conical spring actuator array,” *J. Microelectromechanical Syst.*, vol. 14, pp. 243–253, 2005.

- [25] M. Kanik, P. Bordeenithikasem, J. Schroers, N. Selden, A. Desai, D. Kim, and R. M'Closkey, "Microscale three-dimensional hemispherical shell resonators fabricated from metallic glass," in *2014 Int. Symp. Inert. Sensors Syst.*, pp. 1–4, IEEE, 2014.
- [26] G. Kumar, H. X. Tang, and J. Schroers, "Nanomoulding with amorphous metals," *Nature*, vol. 457, pp. 868–72, 2009.
- [27] G. Kumar, A. Desai, and J. Schroers, "Bulk metallic glass: the smaller the better," *Adv. Mater.*, vol. 23, pp. 461–76, 2011.
- [28] J. Schroers, G. Kumar, T. M. Hodges, S. Chan, and T. R. Kyriakides, "Bulk metallic glasses for biomedical applications," *Jom*, vol. 61, pp. 21–29, 2009.
- [29] Y. Wang, X. Xie, H. Li, X. Wang, M. Zhao, E. Zhang, Y. Bai, Y. Zheng, and L. Qin, "Biodegradable CaMgZn bulk metallic glass for potential skeletal application," *Acta Biomater.*, vol. 7, pp. 3196–3208, 2011.
- [30] Y. Wang, H. Li, Y. Cheng, Y. Zheng, and L. Ruan, "In vitro and in vivo studies on Ti-based bulk metallic glass as potential dental implant material," *Mater. Sci. Eng. C*, vol. 33, pp. 3489–3497, 2013.
- [31] J. Li, L.-l. Shi, Z.-d. Zhu, Q. He, H.-j. Ai, and J. Xu, "Zr₆₁Ti₂Cu₂₅Al₁₂ metallic glass for potential use in dental implants: Biocompatibility assessment by in vitro cellular responses," *Mater. Sci. Eng. C*, vol. 33, pp. 2113–2121, 2013.
- [32] Z. Parlar, M. Bakkal, and A. J. Shih, "Sliding tribological characteristics of Zr-based bulk metallic glass," *Intermetallics*, vol. 16, pp. 34–41, 2008.
- [33] B.-T. Jang, S.-H. Yi, and S.-S. Kim, "Tribological behavior of Fe-based bulk metallic glass," *J. Mech. Sci. Technol.*, vol. 24, pp. 89–92, 2010.
- [34] E. Fleury, S. Lee, H. Ahn, W. Kim, and D. Kim, "Tribological properties of bulk metallic glasses," *Mater. Sci. Eng. A*, vol. 375-377, pp. 276–279, 2004.
- [35] A. Greer, Y. Cheng, and E. Ma, "Shear bands in metallic glasses," *Mater. Sci. Eng. R Reports*, vol. 74, pp. 71–132, 2013.
- [36] M. D. Ediger, C. Angell, and S. R. Nagel, "Supercooled liquids and glasses," *J. Phys. Chem.*, vol. 100, pp. 13200–13212, 1996.
- [37] P. G. Debenedetti and F. H. Stillinger, "Supercooled liquids and the glass transition," *Nature*, vol. 410, pp. 259–267, 2001.
- [38] R. Busch, J. Schroers, and W. H. Wang, "Thermodynamics and kinetics of bulk metallic glass," *Mrs Bull.*, vol. 32, pp. 620–623, 2007.

- [39] J. Schroers, "Processing of bulk metallic glass," *Adv. Mater.*, vol. 22, pp. 1566–1597, 2010.
- [40] W. L. Johnson, "Bulk glass-forming metallic alloys: science and technology," *Mrs Bull.*, vol. 24, pp. 42–56, 1999.
- [41] M. Telford, "The case for bulk metallic glass," *Mater. Today*, vol. 7, pp. 36–43, 2004.
- [42] X. H. Lin and W. L. Johnson, "Formation of Ti-Zr-Cu-Ni bulk metallic glasses," *J. Appl. Phys.*, vol. 78, pp. 6514–6519, 1995.
- [43] Q. Cao, J. Li, Y. Zhou, and J. Jiang, "Mechanically driven phase separation and corresponding microhardness change in Cu₆₀Zr₂₀Ti₂₀ bulk metallic glass," *Appl. Phys. Lett.*, vol. 86, p. 081913, 2005.
- [44] Q. P. Cao, J. F. Li, Y. H. Zhou, and J. Z. Jiang, "Microstructure and microhardness evolutions of Cu_{47.5}Zr_{47.5}Al₅ bulk metallic glass processed by rolling," *Scr. Mater.*, vol. 59, pp. 673–676, 2008.
- [45] O. Haruyama, Y. Nakayama, R. Wada, H. Tokunaga, J. Okada, T. Ishikawa, and Y. Yokoyama, "Volume and enthalpy relaxation in Zr₅₅Cu₃₀Ni₅Al₁₀ bulk metallic glass," *Acta Mater.*, vol. 58, pp. 1829–1836, 2010.
- [46] N. Van Steenberge, S. Hóbor, S. Suriñach, A. Zhilyaev, F. Houdellier, F. Mompou, M. D. Baró, Á. Révész, and J. Sort, "Effects of severe plastic deformation on the structure and thermo-mechanical properties of Zr₅₅Cu₃₀Al₁₀Ni₅ bulk metallic glass," *J. Alloys Compd.*, vol. 500, pp. 61–67, 2010.
- [47] H. W. Sheng, W. K. Luo, F. M. Alamgir, J. M. Bai, and E. Ma, "Atomic packing and short-to-medium-range order in metallic glasses," *Nature*, vol. 439, pp. 419–425, 2006.
- [48] N. Mattern, P. Jóvári, I. Kaban, S. Gruner, A. Elsner, V. Kokotin, H. Franz, B. Beuneu, and J. Eckert, "Short-range order of Cu-Zr metallic glasses," *J. Alloys Compd.*, vol. 485, pp. 163–169, 2009.
- [49] W. Dmowski, Y. Yokoyama, A. Chuang, Y. Ren, M. Umemoto, K. Tsuchiya, A. Inoue, and T. Egami, "Structural rejuvenation in a bulk metallic glass induced by severe plastic deformation," *Acta Mater.*, vol. 58, pp. 429–438, 2010.
- [50] X. D. Wang, Q. P. Cao, J. Z. Jiang, H. Franz, J. Schroers, R. Z. Valiev, Y. Ivanisenko, H. Gleiter, and H.-J. J. Fecht, "Atomic-level structural modifications induced by severe plastic shear deformation in bulk metallic glasses," *Scr. Mater.*, vol. 64, pp. 81–84, 2011.

- [51] D. B. Miracle, “A physical model for metallic glass structures: an introduction and update,” *Jom*, vol. 64, pp. 846–855, 2012.
- [52] D. B. Miracle, “The density and packing fraction of binary metallic glasses,” *Acta Mater.*, vol. 61, pp. 3157–3171, 2013.
- [53] L. Ward, D. Miracle, W. Windl, O. N. Senkov, and K. Flores, “Structural evolution and kinetics in Cu-Zr metallic liquids from molecular dynamics simulations,” *Phys. Rev. B*, vol. 88, p. 134205, 2013.
- [54] J. Ding, Y.-Q. Cheng, and E. Ma, “Full icosahedra dominate local order in Cu₆₄Zr₃₄ metallic glass and supercooled liquid,” *Acta Mater.*, vol. 69, pp. 343–354, 2014.
- [55] J. Ding, S. Patinet, M. L. Falk, Y. Cheng, and E. Ma, “Soft spots and their structural signature in a metallic glass,” *Proc. Natl. Acad. Sci.*, vol. 111, pp. 14052–14056, 2014.
- [56] Y. Q. Cheng, a. J. Cao, H. W. Sheng, and E. Ma, “Local order influences initiation of plastic flow in metallic glass: effects of alloy composition and sample cooling history,” *Acta Mater.*, vol. 56, pp. 5263–5275, 2008.
- [57] Z. Liu, Y. Yang, S. Guo, X. Liu, J. Lu, Y. Liu, and C. Liu, “Cooling rate effect on Young’s modulus and hardness of a Zr-based metallic glass,” *J. Alloys Compd.*, vol. 509, pp. 3269–3273, 2011.
- [58] Y. Waseda, K. Aust, and T. Masumoto, “Structural changes in amorphous Pd₇₇Si₁₇Cu₆ due to cold rolling and low temperature annealing,” *Scr. Metall.*, vol. 13, pp. 9–12, 1979.
- [59] D. Pan, Y. Yokoyama, T. Fujita, Y. H. Liu, S. Kohara, A. Inoue, and M. W. Chen, “Correlation between structural relaxation and shear transformation zone volume of a bulk metallic glass,” *Appl. Phys. Lett.*, vol. 95, pp. 1–4, 2009.
- [60] Á. Révész, P. Henits, and Z. Kovács, “Structural changes in Zr-based bulk metallic glasses deformed by high pressure torsion,” *J. Alloys Compd.*, vol. 495, pp. 338–340, 2010.
- [61] Á. Révész, E. Schafner, and Z. Kovács, “Structural anisotropy in a Zr₅₇Ti₅Cu₂₀Al₁₀Ni₈ bulk metallic glass deformed by high pressure torsion at room temperature,” *Appl. Phys. Lett.*, vol. 92, 2008.
- [62] Z. Kovács, E. Schafner, and Á. Révész, “Volume changes in vitreous bulk metallic glass during room temperature high-pressure torsion,” *J. Mater. Res.*, vol. 23, pp. 3409–3414, 2008.

- [63] M. M. J. Treacy and K. B. Borisenko, “The local structure of amorphous silicon,” *Science*, vol. 335, pp. 950–953, 2012.
- [64] S. N. Bogle, L. N. Nittala, R. D. Twisten, P. M. Voyles, and J. R. Abelson, “Size analysis of nanoscale order in amorphous materials by variable-resolution fluctuation electron microscopy,” *Ultramicroscopy*, vol. 110, pp. 1273–1278, 2010.
- [65] L. He, J. P. Chu, C.-L. L. Li, C.-M. M. Lee, Y.-C. C. Chen, P. K. Liaw, and P. M. Voyles, “Effects of annealing on the compositional heterogeneity and structure in zirconium-based bulk metallic glass thin films,” *Thin Solid Films*, vol. 561, pp. 87–92, 2014.
- [66] J. Hwang, Z. H. Melgarejo, Y. E. Kalay, I. Kalay, M. J. Kramer, D. S. Stone, and P. M. Voyles, “Nanoscale Structure and Structural Relaxation in Zr₅₀Cu₄₅Al₅ Bulk Metallic Glass,” *Phys. Rev. Lett.*, vol. 108, p. 195505, 2012.
- [67] A. Hirata, P. Guan, T. Fujita, Y. Hirotsu, A. Inoue, A. R. Yavari, T. Sakurai, and M. Chen, “Direct observation of local atomic order in a metallic glass,” *Nat. Mater.*, vol. 10, pp. 28–33, 2011.
- [68] A. Hirata, L. J. Kang, T. Fujita, B. Klumov, K. Matsue, M. Kotani, A. R. Yavari, and M. W. Chen, “Geometric frustration of icosahedron in metallic glasses,” *Science*, vol. 341, pp. 376–379, 2013.
- [69] F. Spaepen, “A microscopic mechanism for steady state inhomogeneous flow in metallic glasses,” *Acta Metall.*, vol. 25, pp. 407–415, 1977.
- [70] A. Argon, “Plastic deformation in metallic glasses,” *Acta Metall.*, vol. 27, pp. 47–58, 1979.
- [71] D. Turnbull and M. H. Cohen, “Free-volume model of the amorphous phase: glass transition,” *J. Chem. Phys.*, vol. 34, p. 120, 1961.
- [72] W. L. Johnson, J. Lu, and M. D. Demetriou, “Deformation and flow in bulk metallic glasses and deeply undercooled glass forming liquids - a self consistent dynamic free volume model,” *Intermetallics*, vol. 10, pp. 1039–1046, 2002.
- [73] C. Szeles and K. G. Lynn, *Positron-annihilation spectroscopy*. WILEY-VCH Verlag GmbH & Co KGaA, 2003.
- [74] K. M. Flores, D. Suh, R. H. Dauskardt, P. Asoka-Kumar, P. A. Sterne, and R. H. Howell, “Characterization of free volume in a bulk metallic glass using positron annihilation spectroscopy,” *J. Mater. Res.*, vol. 17, pp. 1153–1161, 2002.
- [75] D. Miracle, T. Egami, K. Flores, and K. Kelton, “Structural aspects of metallic glasses,” *Mrs Bull.*, vol. 32, pp. 629–634, 2007.

- [76] O. Haruyama, K. Kisara, a. Yamashita, K. Kogure, Y. Yokoyama, and K. Sugiyama, “Characterization of free volume in cold-rolled Zr₅₅Cu₃₀Ni₅Al₁₀ bulk metallic glasses,” *Acta Mater.*, vol. 61, pp. 3224–3232, 2013.
- [77] W. H. Wang, Z. X. Bao, C. X. Liu, D. Q. Zhao, and J. Eckert, “Equation of state of Zr₄₁Ti₁₄Cu_{12.5}Ni₁₀Be_{22.5} bulk metallic glass,” *Phys. Rev. B*, vol. 61, pp. 3166–3169, 2000.
- [78] K. M. Flores, B. P. Kanungo, S. C. Glade, and P. Asoka-Kumar, “Characterization of plasticity-induced structural changes in a Zr-based bulk metallic glass using positron annihilation spectroscopy,” *J. Non. Cryst. Solids*, vol. 353, pp. 1201–1207, 2007.
- [79] C. Nagel, K. Rätzke, E. Schmidtke, F. Faupel, W. Ulfert, K. Rätzke, E. Schmidtke, F. Faupel, and W. Ulfert, “Positron-annihilation studies of free-volume changes in the bulk metallic glass Zr₆₅Al_{7.5}Ni₁₀Cu_{17.5} during structural relaxation and at the glass transition,” *Phys. Rev. B*, vol. 60, pp. 9212–9215, 1999.
- [80] Y. Hu, J.-f. Li, P.-n. Zhang, and Y.-h. Zhou, “Effect of cold rolling on glass transition of Zr₅₅Al₁₀Ni₅Cu₃₀ bulk metallic glass,” *Trans. Nonferrous Met. Soc. China*, vol. 20, pp. 78–81, 2010.
- [81] Z. Evenson, I. Gallino, and R. Busch, “The effect of cooling rates on the apparent fragility of Zr-based bulk metallic glasses,” *J. Appl. Phys.*, vol. 107, p. 123529, 2010.
- [82] R. Brüning and K. Samwer, “Glass transition on long time scales,” *Phys. Rev. B*, vol. 46, pp. 11318–11322, 1992.
- [83] I. Gallino, M. B. Shah, and R. Busch, “Enthalpy relaxation and its relation to the thermodynamics and crystallization of the Zr_{58.5}Cu_{15.6}Ni_{12.8}Al_{10.3}Nb_{2.8} bulk metallic glass-forming alloy,” *Acta Mater.*, vol. 55, pp. 1367–1376, 2007.
- [84] D. P. Aji and G. Johari, “Enthalpy and entropy changes on structural relaxation of Mg₆₅Cu₂₅Tb₁₀ glass,” *Thermochim. Acta*, vol. 503-504, pp. 121–131, 2010.
- [85] A. Slipenyuk and J. Eckert, “Correlation between enthalpy change and free volume reduction during structural relaxation of Zr₅₅Cu₃₀Al₁₀Ni₅ metallic glass,” *Scr. Mater.*, vol. 50, pp. 39–44, 2004.
- [86] V. H. Hammond, M. D. Houtz, J. M. O’Reilly, and J. M. O’Reilly, “Structural relaxation in a bulk metallic glass,” *J. Non. Cryst. Solids*, vol. 325, pp. 179–186, 2003.
- [87] A. Q. Tool, “Relation between inelastic deformability and thermal expansion of glass in its annealing range,” *J. Am. Ceram. Soc.*, vol. 29, pp. 240–253, 1946.

- [88] C. T. Moynihan, A. J. Easteal, M. A. Bolt, and J. Tucker, “Dependence of the fictive temperature of glass on cooling rate,” *J. Am. Ceram. Soc.*, vol. 59, pp. 12–16, 1976.
- [89] Y. Yue, J. Christiansen, and S. Jensen, “Determination of the fictive temperature for a hyperquenched glass,” *Chem. Phys. Lett.*, vol. 357, pp. 20–24, 2002.
- [90] Y. Yue, R. Von der Ohe, and S. L. S. L. Jensen, “Fictive temperature, cooling rate, and viscosity of glasses,” *J. Chem. Phys.*, vol. 120, pp. 8053–9, 2004.
- [91] G. Kumar, P. Neibecker, Y. H. Liu, and J. Schroers, “Critical fictive temperature for plasticity in metallic glasses,” *Nat. Commun.*, vol. 4, p. 1536, 2013.
- [92] G. I. Taylor, “The mechanism of plastic deformation of crystals. part i. theoretical,” *Proc. R. Soc. A Math. Phys. Eng. Sci.*, vol. 145, pp. 362–387, 1934.
- [93] F. A. McClintock and A. Argon, *Mechanical behavior of materials*. Addison-Wesley Pub. Co., 1966.
- [94] M. H. Yoo and J. K. Lee, “Deformation twinning in h.c.p. metals and alloys,” *Philos. Mag. A*, vol. 63, pp. 987–1000, 1991.
- [95] V. Yamakov, D. Wolf, S. R. Phillpot, A. K. Mukherjee, and H. Gleiter, “Deformation-mechanism map for nanocrystalline metals by molecular-dynamics simulation,” *Nat. Mater.*, vol. 3, pp. 43–47, 2004.
- [96] Y. Fan, Y. N. Osetskiy, S. Yip, and B. Yildiz, “Mapping strain rate dependence of dislocation-defect interactions by atomistic simulations,” *Proc. Natl. Acad. Sci. U. S. A.*, vol. 110, pp. 17756–61, 2013.
- [97] G. Odette, M. Alinger, and B. Wirth, “Recent developments in irradiation-resistant steels,” *Annu. Rev. Mater. Res.*, vol. 38, pp. 471–503, 2008.
- [98] M. L. Falk and J. Langer, “Deformation and failure of amorphous, solidlike materials,” *Annu. Rev. Condens. Matter Phys.*, vol. 2, pp. 353–373, 2011.
- [99] M. D. Demetriou, “Modeling the transient flow of undercooled glass-forming liquids,” *J. Appl. Phys.*, vol. 95, p. 2857, 2004.
- [100] L. Anand and C. Su, “A theory for amorphous viscoplastic materials undergoing finite deformations, with application to metallic glasses,” *J. Mech. Phys. Solids*, vol. 53, pp. 1362–1396, 2005.
- [101] Q. Yang, A. Mota, and M. Ortiz, “A finite-deformation constitutive model of bulk metallic glass plasticity,” *Comput. Mech.*, vol. 37, pp. 194–204, 2006.
- [102] E. R. Homer and C. A. Schuh, “Mesoscale modeling of amorphous metals by shear transformation zone dynamics,” *Acta Mater.*, vol. 57, pp. 2823–2833, 2009.

- [103] E. R. Homer and C. a. Schuh, “Three-dimensional shear transformation zone dynamics model for amorphous metals,” *Model. Simul. Mater. Sci. Eng.*, vol. 18, p. 065009, 2010.
- [104] L. Li, E. Homer, and C. Schuh, “Shear transformation zone dynamics model for metallic glasses incorporating free volume as a state variable,” *Acta Mater.*, vol. 61, pp. 3347–3359, 2013.
- [105] P. Zhao, J. Li, and Y. Wang, “Heterogeneously randomized STZ model of metallic glasses: softening and extreme value statistics during deformation,” *Int. J. Plast.*, vol. 40, pp. 1–22, 2013.
- [106] L. Li, N. Wang, and F. Yan, “Transient response in metallic glass deformation: a study based on shear transformation zone dynamics simulations,” *Scr. Mater.*, vol. 80, pp. 25–28, 2014.
- [107] N. Wang, F. Yan, and L. Li, “Mesoscopic examination of cyclic hardening in metallic glass,” *J. Non. Cryst. Solids*, vol. 428, pp. 146–150, 2015.
- [108] E. D. Cubuk, S. S. Schoenholz, J. M. Rieser, B. D. Malone, J. Rottler, D. J. Durian, E. Kaxiras, and A. J. Liu, “Identifying structural flow defects in disordered solids using machine-learning methods,” *Phys. Rev. Lett.*, vol. 114, p. 108001, 2015.
- [109] F. H. Stillinger, “A topographic view of supercooled liquids and glass formation,” *Science*, vol. 267, pp. 1935–9, 1995.
- [110] D. L. Malandro and D. J. Lacks, “Relationships of shear-induced changes in the potential energy landscape to the mechanical properties of ductile glasses,” *J. Chem. Phys.*, vol. 110, p. 4593, 1999.
- [111] D. J. Wales, “A microscopic basis for the global appearance of energy landscapes,” *Science*, vol. 293, pp. 2067–70, 2001.
- [112] J. Hachenberg and K. Samwer, “Indications for a slow β -relaxation in a fragile metallic glass,” *J. Non. Cryst. Solids*, vol. 352, pp. 5110–5113, 2006.
- [113] P. Derlet and R. Maaß, “Linking high- and low-temperature plasticity in bulk metallic glasses: thermal activation, extreme value statistics and kinetic freezing,” *Philos. Mag.*, vol. 93, pp. 4232–4263, 2013.
- [114] H. B. Yu, W. H. Wang, H. Y. Bai, and K. Samwer, “The β -relaxation in metallic glasses,” *Natl. Sci. Rev.*, vol. 1, pp. 429–461, 2014.
- [115] Y. Fan, T. Iwashita, and T. Egami, “How thermally activated deformation starts in metallic glass,” *Nat. Commun.*, vol. 5, p. 5083, 2014.

- [116] Y. Fan, T. Iwashita, and T. Egami, “Crossover from localized to cascade relaxations in metallic glasses,” *Phys. Rev. Lett.*, vol. 115, p. 045501, 2015.
- [117] T. Nieh and J. Wadsworth, “Homogeneous deformation of bulk metallic glasses,” *Scr. Mater.*, vol. 54, pp. 387–392, 2006.
- [118] G. Ma, Z. Zhu, Z. Wang, and H. Zhang, “Deformation Behavior of the Zr_{53.5}Cu_{26.5}Ni₅Al₁₂Ag₃ Bulk Metallic Glass Over a Wide Range of Strain Rate and Temperatures,” *J. Mater. Sci. Technol.*, vol. 31, pp. 941–945, 2015.
- [119] A. Vormelker, O. Vatamanu, L. Kecskes, and J. Lewandowski, “Effects of test temperature and loading conditions on the tensile properties of a Zr-based bulk metallic glass,” *Metall. Mater. Trans. A*, vol. 39, pp. 1922–1934, 2007.
- [120] J. Lu, G. Ravichandran, and W. Johnson, “Deformation behavior of the Zr_{41.2}Ti_{13.8}Cu_{12.5}Ni₁₀Be_{22.5} bulk metallic glass over a wide range of strain-rates and temperatures,” *Acta Mater.*, vol. 51, pp. 3429–3443, 2003.
- [121] K. S. Lee, H. J. Jun, S. Pauly, B. Bartusch, Y. W. Chang, and J. Eckert, “Thermomechanical characterization of Cu_{47.5}Zr_{47.5}Al₅ bulk metallic glass within the homogeneous flow regime,” *Intermetallics*, vol. 17, pp. 65–71, 2009.
- [122] H. Kato, Y. Kawamura, A. Inoue, and H. S. Chen, “Newtonian to non-Newtonian master flow curves of a bulk glass alloy Pd₄₀Ni₁₀Cu₃₀P₂₀,” *Appl. Phys. Lett.*, vol. 73, p. 3665, 1998.
- [123] Y. Kawamura, T. Nakamura, A. Inoue, and T. Masumoto, “High-strain-rate superplasticity due to Newtonian viscous flow in La₅₅Al₂₅Ni₂₀ metallic glass,” *Mater. Trans. Jim*, vol. 40, pp. 794–803, 1999.
- [124] Y. Kawamura, T. Nakamura, and A. Inoue, “Superplasticity in Pd₄₀Ni₄₀P₂₀ metallic glass,” *Acta Metall.*, vol. 39, pp. 301–306, 1998.
- [125] M. Heggen, F. Spaepen, and M. Feuerbacher, “Creation and annihilation of free volume during homogeneous flow of a metallic glass,” *J. Appl. Phys.*, vol. 97, p. 033506, 2005.
- [126] B. Daniel, A. Reger-Leonhard, M. Heilmaier, J. Eckert, and L. Schultz, “Thermal Relaxation and High Temperature Creep of Zr₅₅Cu₃₀Al₁₀Ni₅ Bulk Metallic Glass,” *Mech. Time-Dependent Mater.*, vol. 6, pp. 193–206, 2002.
- [127] P. de Hey, J. Sietsma, and A. van den Beukel, “Structural disordering in amorphous Pd₄₀Ni₄₀P₂₀ induced by high temperature deformation,” *Acta Mater.*, vol. 46, pp. 5873–5882, 1998.

- [128] R. D. Conner, W. L. Johnson, N. E. Paton, and W. D. Nix, “Shear bands and cracking of metallic glass plates in bending,” *J. Appl. Phys.*, vol. 94, p. 904, 2003.
- [129] S. Scudino, B. Jerliu, S. Pauly, K. Surreddi, U. Kühn, and J. Eckert, “Ductile bulk metallic glasses produced through designed heterogeneities,” *Scr. Mater.*, vol. 65, pp. 815–818, 2011.
- [130] J. P. Chu, J. Greene, J. S. Jang, J. Huang, Y.-L. Shen, P. K. Liaw, Y. Yokoyama, A. Inoue, and T. Nieh, “Bendable bulk metallic glass: effects of a thin, adhesive, strong, and ductile coating,” *Acta Mater.*, vol. 60, pp. 3226–3238, 2012.
- [131] a. Dubach, F. H. Dalla Torre, and J. F. Löffler, “Deformation kinetics in Zr-based bulk metallic glasses and its dependence on temperature and strain-rate sensitivity,” *Philos. Mag. Lett.*, vol. 87, pp. 695–704, 2007.
- [132] D. Klaumünzer, R. Maaß, and J. F. Löffler, “Stick-slip dynamics and recent insights into shear banding in metallic glasses,” *J. Mater. Res.*, vol. 26, pp. 1453–1463, 2011.
- [133] D. C. Hofmann, J.-Y. Suh, A. Wiest, G. Duan, M.-L. Lind, M. D. Demetriou, and W. L. Johnson, “Designing metallic glass matrix composites with high toughness and tensile ductility,” *Nature*, vol. 451, pp. 1085–1089, 2008.
- [134] J. Schroers and W. Johnson, “Ductile bulk metallic glass,” *Phys. Rev. Lett.*, vol. 93, p. 255506, 2004.
- [135] G. R. Garrett, M. D. Demetriou, J. Chen, and W. L. Johnson, “Effect of microalloying on the toughness of metallic glasses,” *Appl. Phys. Lett.*, vol. 101, p. 241913, 2012.
- [136] C. Qin, W. Zhang, H. Kimura, K. Asami, and A. Inoue, “New Cu-Zr-Al-Nb bulk glassy alloys with high corrosion resistance,” *Mater. Trans.*, vol. 45, pp. 1958–1961, 2004.
- [137] L. Yang, G.-Q. Guo, L.-Y. Chen, B. LaQua, and J.-Z. Jiang, “Tuning local structures in metallic glasses by cooling rate,” *Intermetallics*, vol. 44, pp. 94–100, 2014.
- [138] X. Hu, S. C. Ng, Y. P. Feng, and Y. Li, “Cooling-rate dependence of the density of Pd₄₀Ni₁₀Cu₃₀P₂₀ bulk metallic glass,” *Phys. Rev. B*, vol. 64, p. 172201, 2001.
- [139] Y. Liu, H. Bei, C. T. Liu, and E. P. George, “Cooling-rate induced softening in a Zr₅₀Cu₅₀ bulk metallic glass,” *Appl. Phys. Lett.*, vol. 90, pp. 28–31, 2007.

- [140] Y. Huang, H. Fan, D. Wang, Y. Sun, F. Liu, J. Shen, J. Sun, and J. Mi, “The effect of cooling rate on the wear performance of a ZrCuAlAg bulk metallic glass,” *Mater. Des.*, vol. 58, pp. 284–289, 2014.
- [141] G. Duan, D. Xu, Q. Zhang, G. Zhang, T. Cagin, W. L. Johnson, W. a. Goddard, and W. Goddard III, “Molecular dynamics study of the binary Cu₄₆Zr₅₄ metallic glass motivated by experiments: Glass formation and atomic-level structure,” *Phys. Rev. B*, vol. 71, p. 224208, 2005.
- [142] Y. Hu, H. Yan, T. Lin, J. Li, and Y. Zhou, “Effect of cooling rate on the bending plasticity of Zr₅₅Al₁₀Ni₅Cu₃₀ bulk metallic glass,” *J. Alloys Compd.*, vol. 527, pp. 36–39, 2012.
- [143] G. Duan, M. L. Lind, M. D. Demetriou, W. L. Johnson, W. A. Goddard, T. Cagin, and K. Samwer, “Strong configurational dependence of elastic properties for a binary model metallic glass,” *Appl. Phys. Lett.*, vol. 89, p. 151901, 2006.
- [144] J. Qiao and J. Pelletier, “Enthalpy relaxation in Cu₄₆Zr₄₅Al₇Y₂ and Zr₅₅Cu₃₀Ni₅Al₁₀ bulk metallic glasses by differential scanning calorimetry (DSC),” *Intermetallics*, vol. 19, pp. 9–18, 2011.
- [145] G. P. Tiwari, R. V. Ramanujan, M. R. Gonal, R. Prasad, P. Raj, B. P. Badguzar, and G. L. Goswami, “Structural relaxation in metallic glasses,” *Mater. Sci. Eng. A*, vol. 306, pp. 499–504, 2001.
- [146] M. Kohda, O. Haruyama, T. Ohkubo, and T. Egami, “Kinetics of volume and enthalpy relaxation in Pt₆₀Ni₁₅P₂₅ bulk metallic glass,” *Phys. Rev. B*, vol. 81, p. 092203, 2010.
- [147] A. Kursumović, M. Scott, E. Girt, and R. Cahn, “Changes in the Young’s modulus during structural relaxation of a metallic glass,” *Scr. Metall.*, vol. 14, pp. 1303–1308, 1980.
- [148] P. Wesseling, B. C. Ko, L. O. Vatamanu, G. J. Shiflet, and J. J. Lewandowski, “Effects of annealing and pressure on devitrification and mechanical properties of amorphous Al₈₇Ni₇Gd₆,” *Metall. Mater. Trans. A Phys. Metall. Mater. Sci.*, vol. 39, pp. 1935–1941, 2008.
- [149] B. Zhang, Y. Chen, and H. Guo, “Effects of annealing on structures and properties of Cu-hf-Al amorphous thin films,” *J. Alloys Compd.*, vol. 582, pp. 496–499, 2014.
- [150] P. Murali and U. Ramamurty, “Embrittlement of a bulk metallic glass due to sub-T_g annealing,” *Acta Mater.*, vol. 53, pp. 1467–1478, 2005.
- [151] G. Kumar, D. Rector, R. Conner, and J. Schroers, “Embrittlement of Zr-based bulk metallic glasses,” *Acta Mater.*, vol. 57, pp. 3572–3583, 2009.

- [152] G. S. Yu, J. G. Lin, M. Mo, X. F. Wang, F. H. Wang, and C. E. Wen, “Effect of relaxation on pressure sensitivity index in a Zr-based metallic glass,” *Mater. Sci. Eng. A*, vol. 460-461, pp. 58–62, 2007.
- [153] D. Suh and R. H. Dauskardt, “Mechanical relaxation time scales in a Zr-Ti-Ni-Cu-Be bulk metallic glass,” *J. Mater. Res.*, vol. 17, pp. 1254–1257, 2002.
- [154] J. Gu, M. Song, S. Ni, S. Guo, and Y. He, “Effects of annealing on the hardness and elastic modulus of a Cu₃₆Zr₄₈Al₈Ag₈ bulk metallic glass,” *Mater. Des.*, vol. 47, pp. 706–710, 2013.
- [155] Q. Luo, B. Zhang, D. Q. Zhao, R. J. Wang, M. X. Pan, and W. H. Wang, “Aging and stability of cerium-based bulk metallic glass,” *Appl. Phys. Lett.*, vol. 88, p. 151915, 2006.
- [156] U. Ramamurty, M. L. Lee, J. Basu, and Y. Li, “Embrittlement of a bulk metallic glass due to low-temperature annealing,” *Scr. Mater.*, vol. 47, pp. 107–111, 2002.
- [157] C. H. Rycroft and E. Bouchbinder, “Fracture toughness of metallic glasses: annealing-induced embrittlement,” *Phys. Rev. Lett.*, vol. 109, pp. 1–5, 2012.
- [158] Z. Wang, K. L. Ngai, and W. H. Wang, “Understanding the changes in ductility and Poisson’s ratio of metallic glasses during annealing from microscopic dynamics,” *J. Appl. Phys.*, vol. 118, p. 034901, 2015.
- [159] S. Xie and E. P. George, “Hardness and shear band evolution in bulk metallic glasses after plastic deformation and annealing,” *Acta Mater.*, vol. 56, pp. 5202–5213, 2008.
- [160] Y. Yang, J. Zeng, a. Volland, J. Blandin, S. Gravier, and C. Liu, “Fractal growth of the dense-packing phase in annealed metallic glass imaged by high-resolution atomic force microscopy,” *Acta Mater.*, vol. 60, pp. 5260–5272, 2012.
- [161] Y.-Y. Zhao and X. Zhao, “Structural relaxation and its influence on the elastic properties and notch toughness of mgznca bulk metallic glass,” *J. Alloys Compd.*, vol. 515, pp. 154–160, 2012.
- [162] M. Launey, R. Busch, and J. Kruzic, “Effects of free volume changes and residual stresses on the fatigue and fracture behavior of a Zr-Ti-Ni-Cu-Be bulk metallic glass,” *Acta Mater.*, vol. 56, pp. 500–510, 2008.
- [163] J. Qiao and J. Pelletier, “Influence of thermal treatments and plastic deformation on the atomic mobility in Zr_{50.7}Cu₂₈Ni₉Al_{12.3} bulk metallic glass,” *J. Alloys Compd.*, vol. 615, pp. S85–S89, 2014.

- [164] C. E. Packard, L. M. Witmer, and C. A. Schuh, "Hardening of a metallic glass during cyclic loading in the elastic range," *Appl. Phys. Lett.*, vol. 92, p. 171911, 2008.
- [165] C. Packard, E. Homer, N. Al-Aqeeli, and C. A. Schuh, "Cyclic hardening of metallic glasses under Hertzian contacts: experiments and STZ dynamics simulations," *Philos. Mag.*, vol. 90, pp. 1373–1390, 2010.
- [166] P. Tong, D. Louca, G. Wang, P. K. Liaw, E. Maxey, and Y. Yokoyama, "The Effects of Fatigue on the Atomic Structure with Cyclic Loading in Zr₅₀Cu₄₀Al₁₀ and Zr₆₀Cu₃₀Al₁₀ Glasses," *Metall. Mater. Trans. A*, vol. 43, pp. 2676–2679, 2011.
- [167] F. Delogu, "Effects of compression cycles on the atomic mobility in metallic glasses," *Phys. Rev. B*, vol. 79, p. 064205, 2009.
- [168] C. Deng and C. A. Schuh, "Atomistic mechanisms of cyclic hardening in metallic glass," *Appl. Phys. Lett.*, vol. 100, p. 251909, 2012.
- [169] Y. C. Lo, H. S. Chou, Y. T. Cheng, J. C. Huang, J. R. Morris, and P. K. Liaw, "Structural relaxation and self-repair behavior in nano-scaled Zr-Cu metallic glass under cyclic loading: molecular dynamics simulations," *Intermetallics*, vol. 18, pp. 954–960, 2010.
- [170] J. Luo, K. Dahmen, K. Liaw, Y. Shi, P. K. Liaw, and Y. Shi, "Low-cycle fatigue of metallic glass nanowires," *Acta Mater.*, vol. 87, pp. 225–232, 2015.
- [171] W. Jiao, P. Wen, H. Y. Bai, Q. P. Kong, and W. H. Wang, "Transiently suppressed relaxations in metallic glass," *Appl. Phys. Lett.*, vol. 103, p. 161902, 2013.
- [172] P. Tong, D. Louca, G. Wang, P. Liaw, Y. Yokoyama, A. Llobet, H. Kawaji, Y. Qiu, and Y. Shi, "Structural irreversibility and enhanced brittleness under fatigue in Zr-based amorphous solids," *Metals (Basel)*, vol. 2, pp. 529–539, 2012.
- [173] V. Y. Zadorozhnyy, M. Y. Zadorozhnyy, A. Y. huryumov, S. V. Ketov, I. S. Golovin, and D. V. Louzguine-Luzgin, "Room-temperature dynamic quasi-elastic mechanical behavior of a Zr-Cu-Fe-Al bulk metallic glass," *Phys. Status Solidi*, vol. 213, pp. 450–456, 2016.
- [174] R. Cao, Y. Deng, and C. Deng, "Hardening and crystallization in monatomic metallic glass during elastic cycling," *J. Mater. Res.*, vol. 30, pp. 1820–1826, 2015.

- [175] Y. Shi, D. Louca, G. Wang, and P. K. Liaw, "Compression-compression fatigue study on model metallic glass nanowires by molecular dynamics simulations," *J. Appl. Phys.*, vol. 110, p. 023523, 2011.
- [176] N. Al-Aqeeli, "Strengthening behavior due to cyclic elastic loading in Pd-based metallic glass," *J. Alloys Compd.*, vol. 509, pp. 7216–7220, 2011.
- [177] Z. D. Sha, S. X. Qu, Z. S. Liu, T. J. Wang, and H. Gao, "Cyclic deformation in metallic glasses," *Nano Lett.*, p. 151005081932003, 2015.
- [178] Y. Ye, S. Wang, J. Fan, C. Liu, and Y. Yang, "Atomistic mechanism of elastic softening in metallic glass under cyclic loading revealed by molecular dynamics simulations," *Intermetallics*, vol. 68, pp. 5–10, 2016.
- [179] G. Li, "Structural relaxation of Zr₄₁Ti₁₄Cu_{12.5}Ni₁₀Be_{22.5} bulk metallic glass under high pressure," *Sci. China Ser. G*, vol. 46, p. 468, 2003.
- [180] W. H. Wang, R. J. Wang, D. Q. Zhao, M. X. Pan, and Y. S. Yao, "Microstructural transformation in a Zr₄₁Ti₄₁Cu_{12.5}Ni₁₀Be_{22.5} bulk metallic glass under high pressure," *Phys. Rev. B*, vol. 62, pp. 11292–11295, 2000.
- [181] P. Yu, H. Y. Bai, J. G. Zhao, C. Q. Jin, and W. H. Wang, "Pressure effects on mechanical properties of bulk metallic glass," *Appl. Phys. Lett.*, vol. 90, p. 051906, 2007.
- [182] B. C. Ko, P. Wesseling, O. L. Vatamanu, G. J. Shiflet, and J. J. Lewandowski, "Effects of annealing at high pressure on structure and mechanical properties of Al₈₇Ni₇Gd₆ metallic glass," *Intermetallics*, vol. 10, pp. 1099–1103, 2002.
- [183] J. Z. Jiang, L. Gerward, and Y. S. Xu, "Pressure effect on crystallization kinetics in Zr_{46.8}Ti_{8.2}Cu_{7.5}Ni₁₀Be_{27.5} bulk glass," *Appl. Phys. Lett.*, vol. 81, pp. 4347–4349, 2002.
- [184] H. Kato, J. Saida, and A. Inoue, "Influence of hydrostatic pressure during casting on as cast structure and mechanical properties in Zr₆₅Al_{7.5}Ni₁₀Cu_{17.5}Pd_x (x=0, 17.5) alloys," *Scr. Mater.*, vol. 51, pp. 1063–1068, 2004.
- [185] W. H. Wang, R. J. Wang, D. Y. Dai, D. Q. Zhao, M. X. Pan, and Y. S. Yao, "Pressure-induced amorphization of ZrTiCuNiBe bulk glass-forming alloy," *Appl. Phys. Lett.*, vol. 79, p. 1106, 2001.
- [186] M. Yousuf and K. G. Rajan, "Pressure induced structural relaxation in amorphous solids - example of Fe₄₀Ni₄₀P₁₄B₆," *J. Mater. Sci. Lett.*, vol. 3, pp. 149–152, 1984.
- [187] G. Johari, "Localized molecular motions of β -relaxation and its energy landscape," *J. Non. Cryst. Solids*, vol. 307-310, pp. 317–325, 2002.

- [188] G. Ruitenberg, P. De Hey, F. Sommer, and J. Sietsma, “Pressure-Induced Structural Relaxation in Amorphous Pd₄₀Ni₄₀P₂₀: The formation volume for diffusion defects,” *Phys. Rev. Lett.*, vol. 79, pp. 4830–4833, 1997.
- [189] L.-M. Wang, G. Li, Z. Zhan, L. Sun, and W. Wang, “Comparison of structural relaxation of Pd₃₉Ni₁₀Cu₃₀P₂₁ bulk metallic glass under ambient pressure and at a high pressure,” *Philos. Mag. Lett.*, vol. 81, pp. 419–423, 2001.
- [190] W. H. Wang, Y. X. Zhuang, M. X. Pan, and Y. S. Yao, “Glass transition behavior, crystallization kinetics, and microstructure change of Zr₄₁Ti₁₄Cu_{12.5}Ni₁₀Be_{22.5} bulk metallic glass under high pressure,” *J. Appl. Phys.*, vol. 88, p. 3914, 2000.
- [191] H. Jin, X. Gu, P. Wen, L. Wang, and K. Lu, “Pressure effect on the structural relaxation and glass transition in metallic glasses,” *Acta Mater.*, vol. 51, pp. 6219–6231, 2003.
- [192] M. X. Pan, J. G. Wang, Y. S. Yao, D. Q. Zhao, and W. H. Wang, “Phase transition of Zr₄₁Ti₁₄Cu_{12.5}Ni₁₀Be_{22.5} bulk amorphous below glass transition temperature under high pressure,” *Appl. Phys. Lett.*, vol. 78, p. 601, 2001.
- [193] J. Saida, R. Yamada, and M. Wakeda, “Recovery of less relaxed state in Zr-Al-Ni-Cu bulk metallic glass annealed above glass transition temperature,” *Appl. Phys. Lett.*, vol. 103, p. 221910, 2013.
- [194] M. Wakeda, J. Saida, J. Li, and S. Ogata, “Controlled rejuvenation of amorphous metals with thermal processing,” *Sci. Rep.*, vol. 5, p. 10545, 2015.
- [195] S. Hobor, A. Revesz, P. J. Szabo, A. P. Zhilyaev, V. K. Kis, J. L. Labar, and Z. Kovacs, “High pressure torsion of amorphous Cu₆₀Zr₃₀Ti₁₀ alloy,” *J. Appl. Phys.*, vol. 104, p. 033525, 2008.
- [196] Y. B. Wang, D. D. Qu, X. H. Wang, Y. Cao, X. Z. Liao, M. Kawasaki, S. P. Ringer, Z. W. Shan, T. G. Langdon, and J. Shen, “Introducing a strain-hardening capability to improve the ductility of bulk metallic glasses via severe plastic deformation,” *Acta Mater.*, vol. 60, pp. 253–260, 2012.
- [197] B. Zheng, Y. Zhou, S. N. Mathaudhu, R. Z. Valiev, C. Y. Tsao, J. M. Schoenung, and E. J. Lavernia, “Multiple and extended shear band formation in mgcugd metallic glass during high-pressure torsion,” *Scr. Mater.*, vol. 86, pp. 24–27, 2014.
- [198] F. Meng, K. Tsuchiya, Y. Yokoyama, I. Seiichiro, and Y. Yokoyama, “Reversible transition of deformation mode by structural rejuvenation and relaxation in bulk metallic glass,” *Appl. Phys. Lett.*, vol. 101, p. 121914, 2012.

- [199] S. Hóbor, Z. Kovács, and Á. Révész, “Effect of accumulated shear on the microstructure and morphology of severely deformed Cu₆₀Zr₃₀Ti₁₀ metallic glass,” *J. Alloys Compd.*, vol. 509, pp. 8641–8648, 2011.
- [200] S.-H. Joo, D.-H. Pi, A. D. H. Setyawan, H. Kato, M. Janecek, Y. C. Kim, S. Lee, and H. S. Kim, “Work-hardening induced tensile ductility of bulk metallic glasses via high-pressure torsion,” *Sci. Rep.*, vol. 5, p. 9660, 2015.
- [201] S. Hóbor, Z. Kovács, A. P. Zhilyaev, L. K. Varga, P. J. Szabó, and Á. Révész, “High pressure torsion of Cu-based metallic glasses,” *J. Phys. Conf. Ser.*, vol. 240, p. 012153, 2010.
- [202] K. Song, S. Pauly, Y. Zhang, S. Scudino, P. Gargarella, K. Surreddi, U. Kühn, and J. Eckert, “Significant tensile ductility induced by cold rolling in Cu_{47.5}Zr_{47.5}Al₅ bulk metallic glass,” *Intermetallics*, vol. 19, pp. 1394–1398, 2011.
- [203] M. H. Lee, K. S. Lee, J. Das, J. Thomas, U. Kühn, and J. Eckert, “Improved plasticity of bulk metallic glasses upon cold rolling,” *Scr. Mater.*, vol. 62, pp. 678–681, 2010.
- [204] S. Scudino, K. B. Surreddi, and J. Eckert, “Mechanical properties of cold-rolled Zr₆₀Ti₅Ag₅Cu_{12.5}Ni₁₀Al_{7.5} metallic glass,” *Phys. Status Solidi*, vol. 207, pp. 1118–1121, 2010.
- [205] J. M. Park, K. R. Lim, E. S. Park, S. Hong, K. H. Park, J. Eckert, and D. H. Kim, “Internal structural evolution and enhanced tensile plasticity of Ti-based bulk metallic glass and composite via cold rolling,” *J. Alloys Compd.*, vol. 615, pp. S113–S117, 2014.
- [206] S. Takayama, “Drawing of Pd_{77.5}Cu₆Si_{16.5} metallic glass wires,” *Mater. Sci. Eng.*, vol. 38, pp. 41–48, 1979.
- [207] H. Chen, “Effects of cold rolling on Young’s modulus and structure of metallic glasses,” *Scr. Metall.*, vol. 9, pp. 411–415, 1975.
- [208] H. Yan, Y. Hu, Z. Yan, X. Zheng, and Y. Li, “Microstructure Evolution of Zr₅₀Cu₁₈Ni₁₇Al₁₀Ti₅ Bulk Metallic Glass during Cold-rolling,” *J. Mater. Sci. Technol.*, vol. 28, pp. 756–760, 2012.
- [209] H. S. Chen, “Stored energy in a cold-rolled metallic glass,” *Appl. Phys. Lett.*, vol. 29, pp. 328–330, 1976.
- [210] M. Stolpe, J. Kruzic, and R. Busch, “Evolution of shear bands, free volume and hardness during cold rolling of a Zr-based bulk metallic glass,” *Acta Mater.*, vol. 64, pp. 231–240, 2014.

- [211] W. H. Jiang, F. E. Pinkerton, and M. Atzmon, “Mechanical behavior of shear bands and the effect of their relaxation in a rolled amorphous Al-based alloy,” *Acta Mater.*, vol. 53, pp. 3469–3477, 2005.
- [212] S. Scudino, B. Jerliu, K. B. Surreddi, U. Kühn, and J. Eckert, “Effect of cold rolling on compressive and tensile mechanical properties of Zr_{52.5}Ti₅Cu₁₈Ni_{14.5}Al₁₀ bulk metallic glass,” *J. Alloys Compd.*, vol. 509, pp. S128–S130, 2011.
- [213] J. W. Liu, Q. P. Cao, L. Y. Chen, X. D. Wang, and J. Z. Jiang, “Shear band evolution and hardness change in cold-rolled bulk metallic glasses,” *Acta Mater.*, vol. 58, pp. 4827–4840, 2010.
- [214] Q. P. Cao, J. F. Li, Y. H. Zhou, A. Horsewell, and J. Z. Jiang, “Free-volume evolution and its temperature dependence during rolling of Cu₆₀Zr₂₀Ti₂₀ bulk metallic glass,” *Appl. Phys. Lett.*, vol. 87, p. 101901, 2005.
- [215] Q. P. Cao, J. W. Liu, K. J. Yang, F. Xu, Z. Q. Yao, A. Minkow, H. J. Fecht, J. Ivanisenko, L. Y. Chen, X. D. Wang, S. X. Qu, and J. Z. Jiang, “Effect of pre-existing shear bands on the tensile mechanical properties of a bulk metallic glass,” *Acta Mater.*, vol. 58, pp. 1276–1292, 2010.
- [216] J. M. S. Park, H. K. Lim, J.-H. Kim, J. M. S. Park, W. T. Kim, and D. H. Kim, “Shear band formation and mechanical properties of cold-rolled bulk metallic glass and metallic glass matrix composite,” *J. Mater. Sci.*, vol. 40, pp. 1937–1941, 2005.
- [217] Z. Yan, W. Hao, Y. Hu, K. Song, M. Stoica, S. Scudino, and J. Eckert, “Evidence for viscous flow nature in Zr₆₀Al₁₅Ni₂₅ metallic glass subjected to cold rolling,” *Appl. Phys. Lett.*, vol. 103, p. 021907, 2013.
- [218] Y. Yokoyama, K. Yamano, K. Fukaura, H. Sunada, and A. Inoue, “Bulk Metallic Glasses. III. Enhancement of Ductility and Plasticity of Zr₅₅Cu₃₀Al₁₀Ni₅ Bulk Glassy Alloy by Cold Rolling,” *Mater. Trans.*, vol. 42, pp. 623–632, 2001.
- [219] V. a. Khonik and L. V. Spivak, “On the nature of low temperature internal friction peaks in metallic glasses,” *Acta Mater.*, vol. 44, pp. 367–381, 1996.
- [220] H. S. Chen and S. Y. Chuang, “Structural investigation of cold-rolled metallic glasses using positron annihilation methods,” *Appl. Phys. Lett.*, vol. 27, pp. 316–317, 1975.
- [221] T. Masumoto and R. Maddin, “Structural stability and mechanical properties of amorphous metals,” *Mater. Sci. Eng.*, vol. 19, pp. 1–24, 1975.

- [222] C.-M. Lee, K.-W. Park, and J.-C. Lee, “Plasticity improvement of a bulk amorphous alloy based on its viscoelastic nature,” *Scr. Mater.*, vol. 59, pp. 802–805, 2008.
- [223] Y. Tong, W. Dmowski, Z. Witczak, C.-P. Chuang, and T. Egami, “Residual elastic strain induced by equal channel angular pressing on bulk metallic glasses,” *Acta Mater.*, vol. 61, pp. 1204–1209, 2013.
- [224] S. Scudino, K. B. Surreddi, M. S. Khoshkhoo, M. Sakaliyska, G. Wang, and J. Eckert, “Improved Room Temperature Plasticity of Zr_{41.2}Ti_{13.8}Cu_{12.5}Ni₁₀Be_{22.5} Bulk Metallic Glass by Channel-Die Compression,” *Adv. Eng. Mater.*, vol. 12, pp. 1123–1126, 2010.
- [225] T. Yamamoto, T. Takahashi, H. Kimura, and A. Inoue, “Effect of ball-milling and shot-peening on Zr₅₅Al₁₀Ni₅Cu₃₀ alloys,” *J. Alloys Compd.*, vol. 430, pp. 97–101, 2007.
- [226] J. Fornell, a. Concustell, a. L. Greer, S. Suriñach, M. D. Baró, and J. Sort, “Effects of shot peening on the nanoindentation response of Cu_{47.5}Zr_{47.5}Al₅ metallic glass,” *J. Alloys Compd.*, vol. 586, pp. S36–S40, 2014.
- [227] A. Concustell, F. Méar, S. Suriñach, M. Baró, and A. Greer, “Structural relaxation and rejuvenation in a metallic glass induced by shot-peening,” *Philos. Mag. Lett.*, vol. 89, pp. 831–840, 2009.
- [228] F. Mear, B. Lenk, Y. Zhang, and A. Greer, “Structural relaxation in a heavily cold-worked metallic glass,” *Scr. Mater.*, vol. 59, pp. 1243–1246, 2008.
- [229] R. Raghavan, R. Ayer, H. Jin, C. Marzinsky, and U. Ramamurty, “Effect of shot peening on the fatigue life of a Zr-based bulk metallic glass,” *Scr. Mater.*, vol. 59, pp. 167–170, 2008.
- [230] Y. Zhang, W. H. Wang, and A. L. Greer, “Making metallic glasses plastic by control of residual stress,” *Nat. Mater.*, vol. 5, pp. 857–60, 2006.
- [231] Y. Nishi and H. Harano, “Effects of peening on magnetic-flux density in a metallic glass,” *J. Appl. Phys.*, vol. 63, pp. 1141–1143, 1988.
- [232] Y. Nishi, H. Harano, T. Fukunaga, and K. Suzuki, “Effect of peening on structure and volume in a liquid-quenched Pd_{0.835}Si_{0.165} glass,” *Phys. Rev. B*, vol. 37, pp. 2855–2860, 1988.
- [233] J. Fu, Y. Zhu, C. Zheng, R. Liu, and Z. Ji, “Effect of laser shock peening on mechanical properties of Zr-based bulk metallic glass,” *Appl. Surf. Sci.*, vol. 313, pp. 692–697, 2014.

- [234] F. O. Méar, B. Doisneau, a. R. Yavari, and a. L. Greer, “Structural effects of shot-peening in bulk metallic glasses,” *J. Alloys Compd.*, vol. 483, pp. 256–259, 2009.
- [235] L. Wang, L. Wang, Y. Xue, H. Zhang, and H. Fu, “Nanoindentation response of laser shock peened Ti-based bulk metallic glass,” *Aip Adv.*, vol. 5, p. 057156, 2015.
- [236] S. Gonzalez, J. Fornell, E. Pellicer, S. Surinach, M. D. Baro, A. L. Greer, F. J. Belzunce, and J. Sort, “Influence of the shot-peening intensity on the structure and near-surface mechanical properties of Ti₄₀Zr₁₀Cu₃₈Pd₁₂ bulk metallic glass,” *Appl. Phys. Lett.*, vol. 103, p. 211907, 2013.
- [237] J. Fu, Y. Zhu, C. Zheng, R. Liu, and Z. Ji, “Evaluate the effect of laser shock peening on plasticity of Zr-based bulk metallic glass,” *Opt. Laser Technol.*, vol. 73, pp. 94–100, 2015.
- [238] Y. Zhu, J. Fu, C. Zheng, and Z. Ji, “Effect of laser shock peening without absorbent coating on the mechanical properties of Zr-based bulk metallic glass,” *Opt. Laser Technol.*, vol. 75, pp. 157–163, 2015.
- [239] Y. Zhu, J. Fu, C. Zheng, and Z. Ji, “Influence of laser shock peening on morphology and mechanical property of Zr-based bulk metallic glass,” *Opt. Lasers Eng.*, vol. 74, pp. 75–79, 2015.
- [240] Y. Cheng, S. Pang, C. Chen, and T. Zhang, “Size-dependent enhancement of plasticity by laser surface melting in Zr₅₅Al₁₀Ni₅Cu₃₀ bulk metallic glass,” *J. Alloys Compd.*, vol. 658, pp. 49–54, 2016.
- [241] Y. Cao, X. Xie, J. Antonaglia, B. Winiarski, G. Wang, Y. C. Shin, P. J. Withers, K. a. Dahmen, and P. K. Liaw, “Laser shock peening on Zr-based bulk metallic glass and its effect on plasticity: experiment and modeling,” *Sci. Rep.*, vol. 5, p. 10789, 2015.
- [242] S. Mayr, “Impact of ion irradiation on the thermal, structural, and mechanical properties of metallic glasses,” *Phys. Rev. B*, vol. 71, pp. 1–7, 2005.
- [243] Q. Xiao, L. Huang, and Y. Shi, “Suppression of shear banding in amorphous ZrCuAl nanopillars by irradiation,” *J. Appl. Phys.*, vol. 113, p. 083514, 2013.
- [244] K. A. Avchaciov, Y. Ritter, F. Djurabekova, K. Nordlund, and K. Albe, “Controlled softening of Cu₆₄Zr₃₆ metallic glass by ion irradiation,” *Appl. Phys. Lett.*, vol. 102, p. 181910, 2013.
- [245] K. Avchaciov, Y. Ritter, F. Djurabekova, K. Nordlund, and K. Albe, “Effect of ion irradiation on structural properties of Cu₆₄Zr₃₆ metallic glass,” *Nucl.*

- Instruments Methods Phys. Res. Sect. B Beam Interact. With Mater. Atoms*, vol. 341, pp. 22–26, 2014.
- [246] R. E. Baumer and M. J. Demkowicz, “Prediction of spontaneous plastic deformation of irradiated metallic glasses due to thermal spike-induced plasticity,” *Mater. Res. Lett.*, vol. 2, pp. 221–226, 2014.
- [247] R. Baumer and M. Demkowicz, “Radiation response of amorphous metal alloys: subcascades, thermal spikes and super-quenched zones,” *Acta Mater.*, vol. 83, pp. 419–430, 2015.
- [248] R. E. Baumer and M. J. Demkowicz, “A figure of merit for susceptibility of irradiated amorphous metal alloys to thermal spike-induced plasticity,” *Acta Mater.*, vol. 102, pp. 251–262, 2016.
- [249] R. Gerling, F. Schimansky, and R. Wagner, “Restoration of the ductility of thermally embrittled amorphous alloys under neutron-irradiation,” *Acta Metall.*, vol. 35, pp. 1001–1006, 1987.
- [250] R. Raghavan, K. Boopathy, R. Ghisleni, M. A. Pouchon, U. Ramamurty, and J. Michler, “Ion irradiation enhances the mechanical performance of metallic glasses,” *Scr. Mater.*, vol. 62, pp. 462–465, 2010.
- [251] R. Raghavan, B. Kombaiah, M. Döbeli, R. Erni, U. Ramamurty, and J. Michler, “Nanoindentation response of an ion irradiated Zr-based bulk metallic glass,” *Mater. Sci. Eng. A*, vol. 532, pp. 407–413, 2012.
- [252] N. Onodera, A. Ishii, Y. Fukumoto, A. Iwase, Y. Yokoyama, and F. Hori, “Local structure and hardness change of Zr₅₀Cu₄₀Al₁₀ bulk glassy alloy after heavy ion irradiation,” *Nucl. Instruments Methods Phys. Res. Sect. B Beam Interact. With Mater. Atoms*, vol. 282, pp. 1–3, 2012.
- [253] Y. H. Liu, F. Zhao, Y. L. Li, and M. W. Chen, “Deformation behavior of metallic glass thin films,” *J. Appl. Phys.*, vol. 112, p. 063504, 2012.
- [254] A. G. Perez-Bergquist, H. Bei, K. J. Leonard, Y. Zhang, and S. J. Zinkle, “Effects of ion irradiation on Zr_{52.5}Cu_{17.9}Ni_{14.6}Al₁₀Ti₅ (BAM-11) bulk metallic glass,” *Intermetallics*, vol. 53, pp. 62–66, 2014.
- [255] S. Klaumünzer and G. Schumacher, “Dramatic growth of glassy Pd₈₀Si₂₀ during heavy-ion irradiation,” *Phys. Rev. Lett.*, vol. 51, pp. 1987–1990, 1983.
- [256] M.-d. Hou, S. Klaumünzer, and G. Schumacher, “Dimensional changes of metallic glasses during bombardment with fast heavy ions,” *Phys. Rev. B*, vol. 41, pp. 1144–1157, 1990.

- [257] S. Michalik, J. Michalikova, M. Pavlovic, P. Sovak, H.-P. Liermann, and M. Migliorini, “Structural modifications of swift-ion-bombarded metallic glasses studied by high-energy x-ray synchrotron radiation,” *Acta Mater.*, vol. 80, pp. 309–316, 2014.
- [258] R. Lontas, X. W. Gu, E. Fu, Y. Wang, N. Li, N. Mara, and J. R. Greer, “Effects of Helium Implantation on the Tensile Properties and Microstructure of Ni₇₃P₂₇ Metallic Glass Nanostructures,” *Nano Lett.*, vol. 14, pp. 5176–5183, 2014.
- [259] D. J. Magagnosc, R. Ehrbar, G. Kumar, M. R. He, J. Schroers, and D. S. Gianola, “Tunable tensile ductility in metallic glasses,” *Sci. Rep.*, vol. 3, pp. 16–18, 2013.
- [260] D. Magagnosc, G. Kumar, J. Schroers, P. Felfer, J. Cairney, and D. Gianola, “Effect of ion irradiation on tensile ductility, strength and fictive temperature in metallic glass nanowires,” *Acta Mater.*, vol. 74, pp. 165–182, 2014.
- [261] J. Heo, S. Kim, S. Ryu, and D. Jang, “Delocalized plastic flow in proton-irradiated monolithic metallic glasses,” *Sci. Rep.*, vol. 6, p. 23244, 2016.
- [262] S. V. Ketov, Y. H. Sun, S. Nachum, Z. Lu, a. Checchi, a. R. Beraldin, H. Y. Bai, W. H. Wang, D. V. Louzguine-Luzgin, M. a. Carpenter, and a. L. Greer, “Rejuvenation of metallic glasses by non-affine thermal strain,” *Nature*, vol. 524, pp. 200–203, 2015.
- [263] D. V. Louzguine-Luzgin, L. V. Louzguina-Luzgina, S. V. Ketov, V. Y. Zadorozhnyy, and a. L. Greer, “Influence of cyclic loading on the onset of failure in a Zr-based bulk metallic glass,” *J. Mater. Sci.*, vol. 49, pp. 6716–6721, 2014.
- [264] H. Guo, P. F. Yan, Y. B. Wang, J. Tan, Z. F. Zhang, M. L. Sui, and E. Ma, “Tensile ductility and necking of metallic glass,” *Nat. Mater.*, vol. 6, pp. 735–739, 2007.
- [265] C. A. Volkert, A. Donohue, and F. Spaepen, “Effect of sample size on deformation in amorphous metals,” *J. Appl. Phys.*, vol. 103, p. 083539, 2008.
- [266] Z. W. Shan, J. Li, Y. Q. Cheng, a. M. Minor, S. a. Syed Asif, O. L. Warren, and E. Ma, “Plastic flow and failure resistance of metallic glass: insight from in situ compression of nanopillars,” *Phys. Rev. B*, vol. 77, pp. 1–6, 2008.
- [267] D. Jang and J. Greer, “Transition from a strong-yet-brittle to a stronger-and-ductile state by size reduction of metallic glasses,” *Nat. Mater.*, vol. 9, pp. 1–5, 2010.
- [268] D. Jang, C. T. Gross, and J. R. Greer, “Effects of size on the strength and deformation mechanism in Zr-based metallic glasses,” *Int. J. Plast.*, vol. 27, pp. 858–867, 2011.

- [269] C. Chen, Y. Pei, O. Kuzmin, Z. Zhang, E. Ma, and J. De Hosson, “Intrinsic size effects in the mechanical response of taper-free nanopillars of metallic glass,” *Phys. Rev. B*, vol. 83, pp. 4–7, 2011.
- [270] O. Kuzmin, Y. Pei, C. Chen, and J. De Hosson, “Intrinsic and extrinsic size effects in the deformation of metallic glass nanopillars,” *Acta Mater.*, vol. 60, pp. 889–898, 2012.
- [271] B. Schuster, Q. Wei, M. Ervin, S. Hruszkewycz, M. Miller, T. Hufnagel, and K. Ramesh, “Bulk and microscale compressive properties of a Pd-based metallic glass,” *Scr. Mater.*, vol. 57, pp. 517–520, 2007.
- [272] B. Schuster, Q. Wei, T. Hufnagel, and K. Ramesh, “Size-independent strength and deformation mode in compression of a Pd-based metallic glass,” *Acta Mater.*, vol. 56, pp. 5091–5100, 2008.
- [273] L. Tian, Y.-Q. Cheng, Z.-W. Shan, J. Li, C.-C. Wang, X.-D. Han, J. Sun, and E. Ma, “Approaching the ideal elastic limit of metallic glasses,” *Nat. Commun.*, vol. 3, p. 609, 2012.
- [274] C.-C. Wang, J. Ding, Y.-Q. Cheng, J.-C. Wan, L. Tian, J. Sun, Z.-W. Shan, J. Li, and E. Ma, “Sample size matters for Al₈₈Fe₇Gd₅ metallic glass: Smaller is stronger,” *Acta Mater.*, vol. 60, pp. 5370–5379, 2012.
- [275] D. Z. Chen, D. Jang, K. M. Guan, Q. An, W. a. Goddard, and J. R. Greer, “Nanometallic glasses: size reduction brings ductility, surface state drives its extent,” *Nano Lett.*, vol. 13, pp. 4462–8, 2013.
- [276] D. Tönnies, R. Maaß, and C. a. Volkert, “Room temperature homogeneous ductility of micrometer-sized metallic glass,” *Adv. Mater.*, vol. 26, pp. 5715–5721, 2014.
- [277] W. Xiuying, Y. Chao, F. Changzeng, L. Riping, S. Liling, Z. Jun, Z. Jaojo, and W. Wenkui, “Effect of proton irradiation on structure relaxation of Zr_{41.5}Ti_{14.9}Cu_{12.6}Vi_{10.5}Be_{20.4} bulk metallic glass,” *Chinese Sci. Bull.*, vol. 49, pp. 999–1001, 2004.
- [278] D. S. Gianola, A. Sedlmayr, R. Mönig, C. A. Volkert, R. C. Major, E. Cyrankowski, S. A. S. Asif, O. L. Warren, and O. Kraft, “In situ nanomechanical testing in focused ion beam and scanning electron microscopes,” *Rev. Sci. Instrum.*, vol. 82, p. 063901, 2011.
- [279] K. F. Murphy, L. Y. Chen, and D. S. Gianola, “Effect of organometallic clamp properties on the apparent diversity of tensile response of nanowires,” *Nanotechnology*, vol. 24, p. 235704, 2013.

- [280] J. R. Taylor, *An introduction to error analysis : the study of uncertainties in physical measurements*. University Science Books, 1997.
- [281] R. Agrawal, R. A. Bernal, D. Isheim, and H. D. Espinosa, “Characterizing atomic composition and dopant distribution in wide band gap semiconductor nanowires using laser-assisted atom probe tomography,” *J. Phys. Chem. C*, vol. 115, pp. 17688–17694, 2011.
- [282] C. a. Schuh and A. C. Lund, “Atomistic basis for the plastic yield criterion of metallic glass,” *Nat. Mater.*, vol. 2, pp. 449–52, 2003.
- [283] G. Kumar, S. Prades-Rodel, A. Blatter, and J. Schroers, “Unusual brittle behavior of Pd-based bulk metallic glass,” *Scr. Mater.*, vol. 65, pp. 585–587, 2011.
- [284] S. Sastry, P. G. Debenedetti, and F. H. Stillinger, “Signatures of distinct dynamical regimes in the energy landscape of a glass-forming liquid,” *Nature*, vol. 393, pp. 554–557, 1998.
- [285] M. J. Demkowicz and A. S. Argon, “High-density liquidlike component facilitates plastic flow in a model amorphous silicon system,” *Phys. Rev. Lett.*, vol. 93, p. 025505, 2004.
- [286] A. Dubach, R. Raghavan, J. Loffler, J. Michler, and U. Ramamurty, “Micropillar compression studies on a bulk metallic glass in different structural states,” *Scr. Mater.*, vol. 60, pp. 567–570, 2009.
- [287] C. J. Lee, J. C. Huang, and T. G. Nieh, “Sample size effect and microcompression of Mg₆₅Cu₂₅Gd₁₀ metallic glass,” *Appl. Phys. Lett.*, vol. 91, p. 161913, 2007.
- [288] Y. Lai, C. Lee, Y. Cheng, H. Chou, H. Chen, X. Du, C. Chang, J. Huang, S. Jian, J. Jang, and T. Nieh, “Bulk and microscale compressive behavior of a Zr-based metallic glass,” *Scr. Mater.*, vol. 58, pp. 890–893, 2008.
- [289] A. Yavari, K. Georgarakis, W. Botta, and A. Inoue, “Homogenization of plastic deformation in metallic glass foils less than one micrometer thick,” *Phys. Rev. B*, vol. 82, p. 172202, 2010.
- [290] P. Sigmund, “A mechanism of surface micro-roughening by ion bombardment,” *J. Mater. Sci.*, vol. 8, pp. 1545–1553, 1973.
- [291] P. Schultz and K. Lynn, “Interaction of positron beams with surfaces, thin films, and interfaces,” *Rev. Mod. Phys.*, vol. 60, pp. 701–779, 1988.
- [292] J. Schroers and W. L. Johnson, “Highly processable bulk metallic glass-forming alloys in the pTconicup system,” *Appl. Phys. Lett.*, vol. 84, p. 3666, 2004.

- [293] E.-J. Donth, *The glass transition: relaxation dynamics in liquids and disordered materials*. Springer, 2001.
- [294] P. Badrinarayanan, W. Zheng, Q. Li, and S. L. Simon, “The glass transition temperature versus the fictive temperature,” *J. Non. Cryst. Solids*, vol. 353, pp. 2603–2612, 2007.
- [295] R. Freed and J. Vander Sande, “The metallic glass Cu₅₆Zr₄₄: Devitrification and the effects of devitrification on mechanical properties,” *Acta Metall.*, vol. 28, pp. 103–121, 1980.
- [296] C. Moynihan, “Structural relaxation and the glass transition,” *Rev. Mineral. Geochemistry*, vol. 32, 1995.
- [297] Z. G. Zhu, P. Wen, D. P. Wang, R. J. Xue, D. Q. Zhao, and W. H. Wang, “Characterization of flow units in metallic glass through structural relaxations,” *J. Appl. Phys.*, vol. 114, p. 083512, 2013.
- [298] M. J. Demkowicz and A. S. Argon, “Liquidlike atomic environments act as plasticity carriers in amorphous silicon,” *Phys. Rev. B*, vol. 72, p. 245205, 2005.
- [299] J. C. Ye, J. Lu, C. T. Liu, Q. Wang, and Y. Yang, “Atomistic free-volume zones and inelastic deformation of metallic glasses,” *Nat. Mater.*, vol. 9, pp. 619–23, 2010.
- [300] P. Guan, M. Chen, and T. Egami, “Stress-temperature scaling for steady-state flow in metallic glasses,” *Phys. Rev. Lett.*, vol. 104, p. 205701, 2010.
- [301] G. Adam and J. H. Gibbs, “On the temperature dependence of cooperative relaxation properties in glass-forming liquids,” *J. Chem. Phys.*, vol. 43, p. 139, 1965.
- [302] B. A. Legg, J. Schroers, and R. Busch, “Thermodynamics, kinetics, and crystallization of Pt_{57.3}Cu_{14.6}Ni_{5.3}P_{22.8} bulk metallic glass,” *Acta Mater.*, vol. 55, pp. 1109–1116, 2007.
- [303] N. Nishiyama, M. Horino, O. Haruyama, and a. Inoue, “Undercooled liquid-to-glass transition during continuous cooling in pdcunip alloys,” *Appl. Phys. Lett.*, vol. 76, p. 3914, 2000.
- [304] P. Sargent and P. Donovan, “Measurements of the microhardness of metallic glasses compared with some theoretical predictions,” *Scr. Metall.*, vol. 16, pp. 1207–1212, 1982.
- [305] a. Zhilyaev and T. Langdon, “Using high-pressure torsion for metal processing: fundamentals and applications,” *Prog. Mater. Sci.*, vol. 53, pp. 893–979, 2008.

- [306] D. Gaskell, *An Introduction to Transport Phenomena In Materials Engineering, 2nd edition*. Momentum Pr, 2012.
- [307] W. F. van Dorp and C. W. Hagen, “A critical literature review of focused electron beam induced deposition,” *J. Appl. Phys.*, vol. 104, p. 081301, 2008.
- [308] R. J. Dias, C. O’Regan, P. Thrompenaars, A. Romano-Rodriguez, J. D. Holmes, J. J. L. (Hans) Mulder, and N. Petkov, “Low resistivity Pt interconnects developed by electron beam assisted deposition using novel gas injector system,” *J. Phys. Conf. Ser.*, vol. 371, p. 012038, 2012.
- [309] C. O’Regan, A. Lee, J. D. Holmes, N. Petkov, P. Trompenaars, and H. Mulders, “Electrical properties of platinum interconnects deposited by electron beam induced deposition of the carbon-free precursor, Pt(PF₃)₄,” *J. Vac. Sci. Technol. B Microelectron. Nanom. Struct.*, vol. 31, p. 021807, 2013.
- [310] B. Böddeker and H. Teichler, “Dynamics near free surfaces of molecular dynamics simulated Ni_{0.5}Zr_{0.5} metallic glass films,” *Phys. Rev. E*, vol. 59, pp. 1948–1956, 1999.
- [311] V. V. Hoang and T. Q. Dong, “Free surface effects on thermodynamics and glass formation in simple monatomic supercooled liquids,” *Phys. Rev. B - Condens. Matter Mater. Phys.*, vol. 84, pp. 1–11, 2011.
- [312] Q. Zhang, Q.-K. Li, and M. Li, “Processing dependence of mechanical properties of metallic glass nanowires,” *Appl. Phys. Lett.*, vol. 106, p. 071905, 2015.
- [313] P. Ballone and S. Rubini, “An embedded atom study of an amorphous metal surface: Pd₈₀Si₂₀,” *Surf. Sci.*, vol. 342, pp. L1116–L1120, 1995.
- [314] J. Yi, W. H. Wang, and J. J. Lewandowski, “Sample size and preparation effects on the tensile ductility of Pd-based metallic glass nanowires,” *Acta Mater.*, vol. 87, pp. 1–7, 2015.
- [315] M. Gopinadhan, Z. Shao, Y. Liu, S. Mukherjee, R. C. Sekol, G. Kumar, A. D. Taylor, J. Schroers, and C. O. Osuji, “Finite size effects in the crystallization of a bulk metallic glass,” *Appl. Phys. Lett.*, vol. 103, p. 111912, 2013.
- [316] S. Sohn, Y. Jung, Y. Xie, C. Osuji, J. Schroers, and J. J. Cha, “Nanoscale size effects in crystallization of metallic glass nanorods,” *Nat. Commun.*, vol. 6, p. 8157, 2015.
- [317] K. L. Kearns, S. F. Swallen, M. D. Ediger, T. Wu, and L. Yu, “Influence of substrate temperature on the stability of glasses prepared by vapor deposition,” *J. Chem. Phys.*, vol. 127, p. 154702, 2007.

- [318] S. F. Swallen, K. L. Kearns, M. K. Mapes, Y. S. Kim, R. J. McMahon, M. D. Ediger, T. Wu, L. Yu, and S. Satija, “Organic glasses with exceptional thermodynamic and kinetic stability,” *Science*, vol. 315, pp. 353–6, 2007.
- [319] Z. Fakhraai, T. Still, G. Fytas, and M. D. Ediger, “Structural variations of an organic glassformer vapor-deposited onto a temperature gradient stage,” *J. Phys. Chem. Lett.*, vol. 2, pp. 423–427, 2011.
- [320] H. B. Yu, Y. Luo, and K. Samwer, “Ultrastable metallic glass,” *Adv. Mater.*, vol. 25, pp. 5904–5908, 2013.
- [321] I. Lyubimov, M. D. Ediger, and J. J. de Pablo, “Model vapor-deposited glasses: growth front and composition effects,” *J. Chem. Phys.*, vol. 139, p. 144505, 2013.
- [322] S. Han, R. Saha, and W. Nix, “Determining hardness of thin films in elastically mismatched film-on-substrate systems using nanoindentation,” *Acta Mater.*, vol. 54, pp. 1571–1581, 2006.
- [323] J. Hay and B. Crawford, “Measuring substrate-independent modulus of thin films,” *J. Mater. Res.*, vol. 26, pp. 727–738, 2011.
- [324] W. Oliver and G. Pharr, “Measurement of hardness and elastic modulus by instrumented indentation: advances in understanding and refinements to methodology,” *J. Mater. Res.*, vol. 19, pp. 3–20, 2004.
- [325] F. Gillessen and D. Herlach, “Thermodynamics of undercooled Pd-Cu-Si melts,” *J. Non. Cryst. Solids*, vol. 117-118, pp. 555–558, 1990.
- [326] R. Conner, R. Maire, and W. Johnson, “Effect of oxygen concentration upon the ductility of amorphous $Zr_{57}Nb_{5}Al_{10}Cu_{15.4}Ni_{12.6}$,” *Mater. Sci. Eng. A*, vol. 419, pp. 148–152, 2006.
- [327] W. Wang, “Roles of minor additions in formation and properties of bulk metallic glasses,” *Prog. Mater. Sci.*, vol. 52, pp. 540–596, 2007.
- [328] B. Yang and T. G. Nieh, “Effect of the nanoindentation rate on the shear band formation in an Au-based bulk metallic glass,” *Acta Mater.*, vol. 55, pp. 295–300, 2007.
- [329] K. L. Kearns, S. F. Swallen, M. D. Ediger, T. Wu, Y. Sun, and L. Yu, “Hiking down the energy landscape: progress toward the kauzmann temperature via vapor deposition,” *J. Phys. Chem. B*, vol. 112, pp. 4934–4942, 2008.
- [330] X. Bian, G. Wang, H. Chen, L. Yan, J. Wang, Q. Wang, P. Hu, J. Ren, K. Chan, N. Zheng, A. Teresiak, Y. Gao, Q. Zhai, J. Eckert, J. Beadsworth, K. Dahmen, and P. Liaw, “Manipulation of free volumes in a metallic glass through Xe-ion irradiation,” *Acta Mater.*, vol. 106, pp. 66–77, 2016.

- [331] H. Huth, A. A. Minakov, and C. Schick, “Differential AC-chip calorimeter for glass transition measurements in ultrathin films,” *J. Polym. Sci. Part B Polym. Phys.*, vol. 44, pp. 2996–3005, 2006.
- [332] K. L. Kearns, K. R. Whitaker, M. D. Ediger, H. Huth, and C. Schick, “Observation of low heat capacities for vapor-deposited glasses of indomethacin as determined by AC nanocalorimetry,” *J. Chem. Phys.*, vol. 133, p. 014702, 2010.
- [333] P. J. McCluskey and J. J. Vlassak, “Combinatorial nanocalorimetry,” *J. Mater. Res.*, vol. 25, pp. 2086–2100, 2011.
- [334] K. Xiao, J. M. Gregoire, P. J. McCluskey, and J. J. Vlassak, “A scanning AC calorimetry technique for the analysis of nano-scale quantities of materials,” *Rev. Sci. Instrum.*, vol. 83, p. 114901, 2012.
- [335] M. Ahrenberg, E. Shoifet, K. R. Whitaker, H. Huth, M. D. Ediger, and C. Schick, “Differential alternating current chip calorimeter for in situ investigation of vapor-deposited thin films,” *Rev. Sci. Instrum.*, vol. 83, p. 033902, 2012.
- [336] R. Garcia, C. Gómez, N. Martinez, S. Patil, C. Dietz, and R. Magerle, “Identification of nanoscale dissipation processes by dynamic atomic force microscopy,” *Phys. Rev. Lett.*, vol. 97, p. 016103, 2006.
- [337] H. Wagner, D. Bedorf, S. Küchemann, M. Schwabe, B. Zhang, W. Arnold, and K. Samwer, “Local elastic properties of a metallic glass,” *Nat. Mater.*, vol. 10, pp. 439–42, 2011.
- [338] J. Zeng, J. Chu, Y. Chen, a. Volland, J. Blandin, S. Gravier, and Y. Yang, “On the use of atomic force microscopy for structural mapping of metallic-glass thin films,” *Intermetallics*, vol. 44, pp. 121–127, 2014.
- [339] C. A. Angell, “Formation of glasses from liquids and biopolymers,” *Science*, vol. 267, pp. 1924–1935, 1995.
- [340] G. J. Fan, H. Choo, and P. K. Liaw, “Fragility of metallic glass-forming liquids: a simple thermodynamic connection,” *J. Non. Cryst. Solids*, vol. 351, pp. 3879–3883, 2005.
- [341] S. Wei, Z. Evenson, I. Gallino, and R. Busch, “The impact of fragility on the calorimetric glass transition in bulk metallic glasses,” *Intermetallics*, vol. 55, pp. 138–144, 2014.
- [342] W. Kauzmann, “The nature of the glassy state and the behavior of liquids at low temperatures,” *Chem. Rev.*, vol. 43, pp. 219–256, 1948.

- [343] A. Sepúlveda, M. Tyllinski, A. Guiseppi-Elie, R. Richert, and M. D. Ediger, “Role of fragility in the formation of highly stable organic glasses,” *Phys. Rev. Lett.*, vol. 113, p. 045901, 2014.
- [344] S. Singh, M. D. Ediger, and J. J. de Pablo, “Ultrastable glasses from in silico vapour deposition,” *Nat. Mater.*, vol. 12, pp. 139–144, 2013.
- [345] D. N. Perera, “Compilation of the fragility parameters for several glass-forming metallic alloys,” *J. Phys. Condens. Matter*, vol. 11, pp. 3807–3812, 1999.
- [346] L. Battezzati, “Interplay of process kinetics in the undercooled melt in the proximity of the glass transition,” *Mater. Sci. Eng. A*, vol. 375-377, pp. 60–65, 2004.